Unveiling the Intrinsic Properties of z～4 Star Forming Galaxies from UV Spectral Slope β

博士論文

Unveiling the Intrinsic Properties of $z \sim 4$ Star Forming Galaxies from UV Spectral Slope β

（紫外線スペクトルスロープ β を用いた赤方偏移 4 に存在する星形成銀河の性質への制限）

A dissertation submitted to
Tohoku University
in partial fulfillment of requirements for the degree of
Doctor of Philosophy (Science)

山中郷史

平成 28 年

Satoshi Yamanaka

Astronomical Institute,
Graduate School of Science,
Tohoku University

March 2017

Abstract

We investigate the stellar population and spatial distribution of star-forming galaxies at $z \sim 4$ by focusing on their slope of rest-frame ultraviolet (UV) continuum, β where $f_\lambda \propto \lambda^\beta$. We analyze the sample of bright Lyman Break Galaxies with $i' \leq 26.0$ in the Subaru/XMM-Newton Deep Survey field. We evaluate the observed UV spectral slope β by the simple power-law fitting and find that it shows little dependence on dust un-corrected UV absolute magnitude in the range of $-22.0 \lesssim M_{UV} \lesssim -20.0$. In order to evaluate the incompleteness of our sample selection, we estimate the recovery fraction based on the simulation with model galaxies and find that the observed flat β-M_{UV} relation cannot be caused by the selection effects but is due to physical reasons. To illustrate how the observed β-M_{UV} relation is formed through dust extinction, we introduce the *intrinsic* UV slope, β_{int}. We investigate the relation between β_{int} and *intrinsic* UV absolute magnitude, $M_{UV,int}$ and find that the β_{int} becomes bluer when the $M_{UV,int}$ becomes brighter. Extrapolation of the β_{int}-$M_{UV,int}$ relation toward the fainter magnitude range below our sample magnitude limit intersects the β_{obs}-$M_{UV,obs}$ relation previously obtained in the deeper narrow-area observations at $M_{UV} = -18.6$ and $\beta = -1.95$, which coincides with the break point of β_{obs}-$M_{UV,obs}$ relation observed so far. It indicates that the little obscured star-forming galaxies at $z \sim 4$ have $\beta \sim -2.0$. Our result also indicates that the galaxies with $\beta_{obs} > -1.7$, Av ≥ 1.0, and $\beta_{int} \leq -2.5$ are the intrinsically active star-forming (SFR $\gtrsim$ a few $\times 10^2 \mathrm{M}_\odot yr^{-1}$) galaxies suffering the dust reddening, and our flat β_{obs}-$M_{UV,obs}$ relation is seen due to such population. Spatial clustering properties of the sub-samples with the blue and red β_{obs} is also discussed.

Contents

1 INTRODUCTION **7**
- 1.1 *UV Spectral Slope β* . . . 7
- 1.2 *Stellar Population of High-z SFGs* . . . 12
- 1.3 *Spatial Clustering* . . . 18
- 1.4 *Direction of This Work* . . . 20

2 DATA **23**

3 ANALYSIS **27**
- 3.1 *Measurements of UV Spectral Slope β* . . . 27
- 3.2 *Photometric Catalog for SXDS Field* . . . 29
- 3.3 *Methodology of Clustering Analysis* . . . 30

4 RESULTS **33**
- 4.1 *Observed Distribution of UV Spectral Slope β* . . . 33
- 4.2 *Incompleteness of Our Selection* . . . 36

5 DISCUSSION **43**
- 5.1 *Validity of Our SED Fitting Analysis* . . . 43
- 5.2 *Intrinsic UV Spectral Slope β* . . . 46
- 5.3 *β_{int}-$M_{\mathrm{UV},int}$ Relation* . . . 50
- 5.4 *Color-Color Diagram* . . . 51
- 5.5 *Implication for Most Active SFGs at $z \sim 4$* . . . 56
- 5.6 *Dust Attenuation Law of Intrinsically Active SFGs at $z \sim 4$* . . . 58

6 FUTURE PROSPECTS **63**
- 6.1 *Analysis of Angular Auto Correlation Function* . . . 63
- 6.2 *EW(Hβ)-β Method* . . . 71

7 SUMMARY **75**

Chapter 1

INTRODUCTION

In this chapter, we introduce the previous studies of ultraviolet (UV) spectral slope β, stellar population of high-redshift star-forming galaxies, Dusty Star-Forming Galaxies (DSFGs), and spatial clustering of galaxies. At a glance, while they seem not to be related each other, the UV spectral slope β can shed light on the issues of each topic. Thus, we also explain the relevance between UV spectral slope β and each topic in the following section, and we summarize them in the final section.

1.1 *UV Spectral Slope* β

The UV continuum spectrum of star-forming galaxies was first characterized by the spectral index β in the form of $f_\lambda \propto \lambda^\beta$ in Calzetti et al. (1994). This UV spectral slope β is a useful probe for the physical quantities of star-forming galaxies such as dust contents, age of galaxy, Star Formation History (SFH), and metallicity. In the case of less dust attenuation, younger age, and lower metallicity, the galaxy has the larger negative β value (Figure 1.1). Since it is relatively simple to measure β values and the rest-frame UV light is observable from local to high redshift galaxies by current instruments, the UV spectral slope β is one of the most important information for star-forming galaxies.

1.1.1 *Overview*

Interstellar dust scatters and/or absorbs UV light, and the UV light at shorter wavelength is more scattered/absorbed than the UV light at longer wavelength. The wavelength dependence of dust scattering/absorption is investigated as dust attenuation curve of Milky Way, Large Magellanic Cloud, and/or Small Magellanic Cloud (e.g., Seaton 1979; Koornneef & Code 1981; Bouchet et al. 1985). Therefore, the dust reddening is considered to be the dominant factor controlling the β value. Indeed, there seems to be a linear correlation between the β value and the Balmer decrement (i.e., the difference of Balmer line optical depth between Hα and Hβ, which represents the amount of the dust attenuation), and this linear correlation can be explained by both models of uniform or clumpy dust screen in front of sources (Calzetti et al. 1994). On the basis of the linear correlation and its independence on dust geometry,

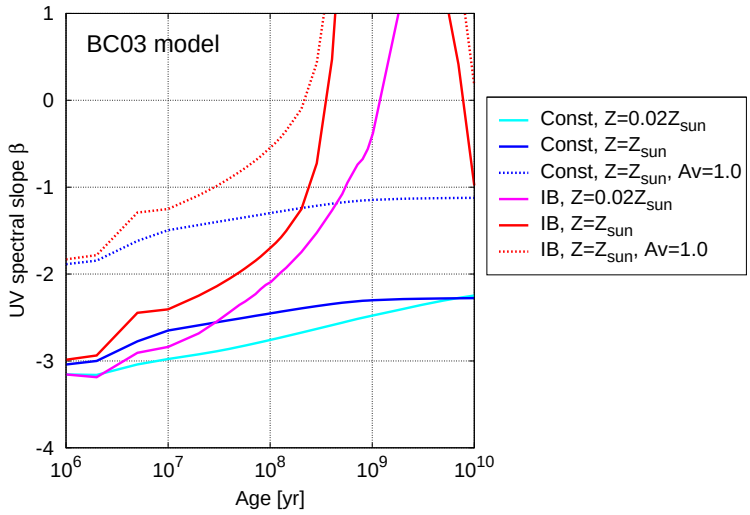

Figure 1.1: Relation between β value and stellar population calculated from stellar population synthesis model. The vertical axis is the UV spectral slope β and the horizontal axis is the age of galaxy. The red and blue solid lines denote the models of instantaneous burst (IB) and continuous constant star-formation (CSF) with solar metallicity, respectively. The magenta and cyan solid lines denote the models of IB and CSF with lower metallicity ($Z = 0.02Z_{\odot}$), respectively. The red and blue dotted-lines show the dust-attenuated models of IB and CSF with solar metallicity and Av = 1.0 assuming the dust attenuation law of Calzetti et al. (2000), respectively.

the relationship between the β value and the ratio of Far-InfraRed (FIR) to UV fluxes (called InfraRed Excess, IRX; IRX = $F_{\rm FIR}/F_{\rm UV}$) is calibrated for the local starburst galaxies, and it is known as a powerful empirical relation, 'IRX-β relation' (Meurer et al. 1999, hereafter M99; Figure 1.5). The FIR flux comes from the dust which is heated by the UV radiation, and hence the IRX value is a direct indicator of dust absorption. By using the IRX-β relation, we can estimate the dust attenuation value from the UV observation alone.

Subsequent studies, however, indicate that the M99 IRX-β relation is not always applicable to the local star-forming galaxies; the deviation from the M99 IRX-β relation is reported for quiescent normal star-forming galaxies and IR luminous galaxies (e.g., Kong et al. 2004; Burgarella et al. 2005a,b). The normal star-forming galaxies are distributed bellow the M99 relation, and the IR luminous galaxies are distributed above the M99 relation. Although the reason of the deviation for the IR luminous galaxies is not still clear (see also Section 1.2), the reason for the quiescent normal star-forming galaxies is that the UV flux is not appropriately measured in M99[1], and the re-examinations for the galaxies used in M99 provide the consistent IRX-β relation for both normal star-forming and starburst galaxies (Overzier et al. 2011; Takeuchi et al. 2012). Recently, thanks to the following new instruments for UV, Mid-IR (MIR), FIR, and Sub-millimeter wavelength range, the IRX-β relation has been studied and

[1]In M99, the UV flux is measured with *International UV Explorer (IUE)* whose maximum aperture size for photometry is much smaller than the aperture size used for IR flux measurement, and then the IRX value is overestimated.

discussed for the star-forming galaxies at $z \sim 0$ (Casey et al. 2014), $z \sim 1$ (Heinis et al. 2013), $z \sim 2$ (Reddy et al. 2006; Chapman et al. 2005), $z \sim 3$ (Oteo et al. 2013; Álvarez-Márquez et al. 2016), and even $z \gtrsim 4$ (Capak et al. 2015; Bouwens et al. 2016b). Consequently, it seems that *typical* star-forming galaxies at $z \lesssim 3$ are roughly distributed on the similar IRX-β relation (Figure 1.5), and we can estimate the dust attenuation from the IRX-β relation.

In the IRX-β formula, we assume that the dust properties and the underlying stellar population of star-forming galaxies do not significantly change among the sample. However, all the quantities can vary from galaxy to galaxy and can cause the scatter in the IRX-β relation. In fact, the β value of local starbursts depends on the metallicity and the β value becomes redder with increasing the metallicity (Heckman et al. 1998). Moreover, high-z star-forming galaxies, whose luminosity is boosted by the gravitational lensing, are individually investigated and it appears that the high-z galaxies also have the similar trend (Pettini et al. 2000, 2002; Finkelstein et al. 2009; Siana et al. 2009; Dessauges-Zavadsky et al. 2010). When considering the link between metal pollution and dust production, these results is not surprising. In other words, the extremely blue galaxies in the β value (i.e., $\beta \sim -3.0$) are expected to be extremely metal poor galaxies or possibly metal-free galaxies. This prediction is also indicated from the stellar population synthesis models (Bouwens et al. 2010; Dunlop et al. 2013). Although the extremely blue galaxies have not been investigated yet, the *very* blue galaxies in the β value ($\beta \sim -2.2$) is certainly low-metallicity galaxies (Erb et al. 2010; de Barros et al. 2016; Naidu et al. 2016). In addition, bluer star-forming galaxies in the β value tend to have less massive stellar mass (Finkelstein et al. 2012a) or the stellar population synthesis models also predict the β dependence on age and SFH of the galaxies. In brief, the β value can be a tracer of not only dust attenuation but also stellar population of star-forming galaxies.

Typical β values for given redshift and UV luminosity are individually studied in the previous literature, and it is broadly found that higher redshift galaxies have bluer β values (hereafter β-z relation) and lower UV luminosity galaxies also have bluer β values (hereafter β-$M_{\rm UV}$ relation). These relations are comprehensively studied and first confirmed in Bouwens et al. (2009, 2010) by using the same data set observed with *Hubble Space Telescope (HST)* and same analysis method for the star-forming galaxies at $z \sim$ 2.5-7. Although the β-$M_{\rm UV}$ relation became a subject of debates, at present the β-$M_{\rm UV}$ relation is accepted to be real and is often understood as another aspect of the mass-metallicity relation seen in star-forming galaxies at $z \lesssim 4$ (Tremonti et al. 2004; Erb et al. 2006; Maiolino et al. 2008; Finkelstein et al. 2012a; Bouwens et al. 2012). Moreover, in the most recent study for the β-$M_{\rm UV}$ relation, it is suggested that there is a "knee" in the β-$M_{\rm UV}$ relation at $M_{\rm UV} \sim -19.0$, and the dependence of β on $M_{\rm UV}$ becomes weaker at $M_{\rm UV} \lesssim -19.0$ than at $M_{\rm UV} > -19.0$ (Bouwens et al. 2014, Figure 1.2 Top). The β-z relation is interpreted as a history of dust attenuation (i.e., dust production in star-forming galaxies) by using the IRX-β relation, and interestingly the dust attenuation history at $z \gtrsim 3.0$ estimated from the β-z relation is smoothly connected with the dust attenuation history at $z \lesssim 3$ estimated from the direct measurements of both IR and UV luminosity (Burgarella et al. 2013, Figure 1.3 Top). The dust attenuation history is used for revealing the history of *true* (*dust-corrected*) cosmic Star Formation Rate (SFR) density (Bouwens et al. 2009, 2012; Madau & Dickinson 2014, Figure 1.3 Bottom), because it is still difficult to obtain IR luminosity for high-z star-forming galaxies. Currently, the β-z relation

has been used for considering the source of cosmic reionization, assuming that the β value represents the production rate of hydrogen ionizing photons (Duncan et al. 2015; Bouwens et al. 2015, 2016a).

In conclusion, the UV spectral slope β has long been investigated from local to high-z ($z \sim 8$) star-forming galaxies. The β value enable us to deduce the stellar population, and especially the IRX-β relation is a powerful empirical tool to estimate the dust attenuation value. The interpretation of β-$M_{\rm UV}$ relation and β-z relation results in the history of dust attenuation, cosmic SFR density, and the source of cosmic reionization. However, there is a discussion about the validity of the IRX-β relation and the detailed investigation for the stellar population of star-forming galaxies is needed in order to utilize the β value as a indicator of the stellar population.

1.1.2 *Recent Issues*

According to the recent works, the typical β value is ~ -1.7 for $\approx L_*$ galaxies at $z = 4$ with $M_{\rm UV} \sim -21.0$ (e.g., Bouwens et al. 2012; Finkelstein et al. 2012a). The typical β value becomes bluer at higher redshift up to at least $z \sim 7$ (β-z relation) and is ~ -1.9 (Wilkins et al. 2011; Bouwens et al. 2014). On the other hand, the typical β value for faint galaxies (e.g., $M_{\rm UV} \sim -19.0$) has still uncertainties and the relation between β and UV absolute magnitude (β-$M_{\rm UV}$ relation) has been a subject of debate for the last several years (Bouwens et al. 2012, 2014; Dunlop et al. 2012, 2013; Finkelstein et al. 2012a; Rogers et al. 2014). Bouwens et al. and Rogers et al. report that bright galaxies have redder β values and faint galaxies have bluer β values (Figure 1.2 Top), while Dunlop et al. and Finkelstein et al. report that β values are constant over the observed magnitude range (Figure 1.2 Bottom). This inconsistency in the β-$M_{\rm UV}$ relation can be caused by both large photometric errors for faint galaxies and selection bias. In the most recent studies, both Duncan et al. (2015) and Bouwens et al. (2014) show that the β value decreases with the $M_{\rm UV}$ value. Duncan et al. find the trend by combining the results of the various literature (Bouwens et al. 2014; Duncan et al. 2014; Dunlop et al. 2012, 2013; Finkelstein et al. 2012a; Rogers et al. 2014; Wilkins et al. 2011) and Bouwens et al. discuss the trend by assessing the observational bias (incompleteness) of the observed β distribution in the faint magnitude range. At present, star-forming galaxies are considered to have the β-$M_{\rm UV}$ relation and for estimating the accurate UV spectral slope β a large sample of objects with small photometric uncertainties is needed and/or it is necessary to assess the incompleteness of the observed β distribution.

We also note that the samples in the recent literature are overlapped to some extent since the set of GOODS-South/*HST* or HUDF/*HST* data was mostly used so far. Due to the small observed area, the number of UV-bright objects in the field is limited (except for Rogers et al. 2014), and thus these previous studies focused on relatively UV-faint galaxies. The β distribution of the UV-bright objects is, however, also important, since such population provides important clues to understand early star-formation history in the universe. In particular, such UV luminous objects are expected to have high star-formation activity (e.g., Kennicutt & Evans 2012) and it is interesting that the UV-luminous galaxies show the trend of β-$M_{\rm UV}$ relation as reported by the previous works. Actually, Lee al. (2011) shows the results for $z \sim 4$ super luminous ($-23.5 \lesssim M_{\rm UV} \lesssim -21.5$) Lyman Break Galaxies (LBGs) and finds

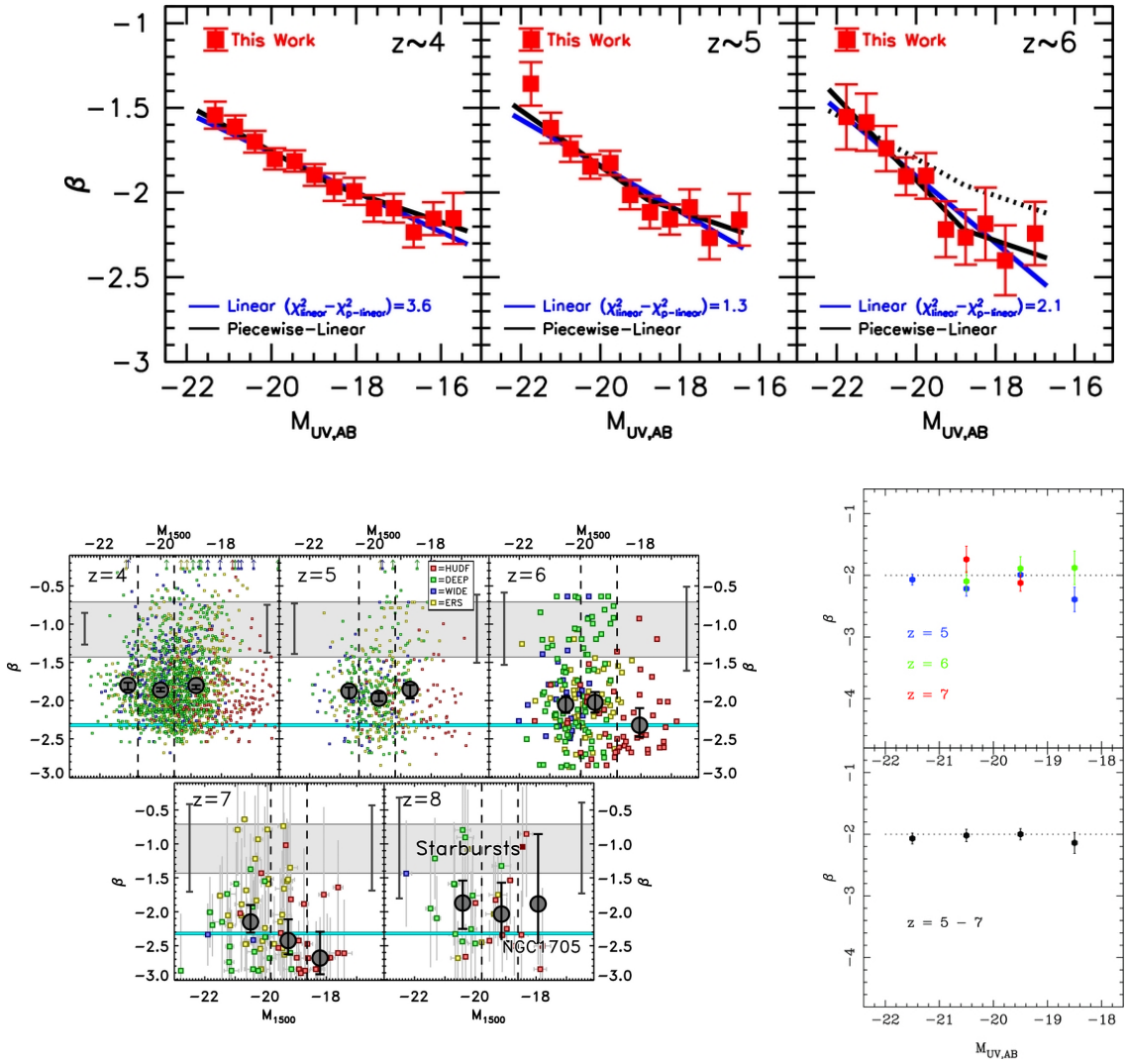

Figure 1.2: The β-$M_{\rm UV}$ relation obtained in three literature for different redshift samples. Top: Result from Bouwens et al. (2014). The red filled squares show the mean β values for each magnitude bin. The blue and black solid lines represent the best-fit simple linear and piecewise-linear function. In the most right panel, the black dotted line represents the best-fit simple linear function for $z \sim 4$ sample. Bottom Left: Result from Finkelstein et al. (2012a). The red, green, blue, and yellow filled squares represent individual galaxies in the Hubble Ultra Deep Field (HUDF), GOODS-South Deep field, GOODS-S Wide filed, and GOODS-S Early Release Science (ERS) field, respectively. The gray circles show the median β value. The gray shaded region indicates the β range of typical local starbursts, whereas the cyan solid line indicates the β value of NGC 1705 which is one of the bluest local starbursts. Bottom Right: Result from Dunlop et al. (2012). In the upper panel, the blue, green, and red points show the average β values for galaxies at $z \simeq 5$, 6, and 7, respectively. In the lower panel, the black points represent the average β value for all galaxies over the redshift range of z =5-7. *The Top and Bottom Left figures are taken from Bouwens et al. (2014) and Finkelstein et al. (2012a), respectively, reproduced by permission of the AAS. The Bottom Right figure is taken from Dunlop et al. (2012).*

that the UV-brighter galaxies have redder β values. However, the authors adopt the image stacking analysis in which they stack all the images and make one deepest average image. By the analysis, it is difficult to discuss the observational bias and the variation of the β values which represents the variety of the stellar population of the UV-bright galaxies. Therefore, it is necessary to investigate the β distribution from individual UV-luminous galaxies observed with wide-field imaging data.

1.2 *Stellar Population of High-z SFGs*

Stellar population of galaxies is key information to understand the galaxy formation and evolution, and the various types of galaxies from local to high redshift universe have been investigated for revealing the stellar population so far. Among the properties of stellar population, dust attenuation value and SFR is estimated and discussed in the relatively wide redshift range. In general, the typical dust attenuation in star-forming galaxies and the cosmic SFR density (SFRD) increase from $z = 0$, and peaks at $z \sim 1$ for the dust obscuration (e.g., Burgarella et al. 2013, Figure 1.3 Top) and at $z \sim 2-3$ for the cosmic SFRD (e.g., Bouwens et al. 2012, Figure 1.3 Bottom; Madau & Dickinson 2014). After the peak, both the quantities decrease with increasing redshift. At $z \lesssim 3$, these results are obtained from the direct measurement of dust thermal emission (typically rest-frame $\lambda = 8 - 1000\mu$m) for individual galaxies. On the other hand, at $z \gtrsim 4$ these results are derived from the indirect method which utilize the UV spectral slope β due to several reasons. In the following subsection, we first introduce the relation between the UV spectral slope β and the stellar population in detail, and then show the key results about the dust obscuration and SFR focusing on highly dust obscured star-forming galaxies (Dusty Star-Forming Galaxies; DSFG).

1.2.1 *Detailed Connection between UV Spectral Slope β and Stellar population*

As described above, the UV spectral slope β is a useful indicator of stellar population of star-forming galaxies. In fact, the UV spectral slope β is sensitive to the existence of hot, massive, and short-lived stars such as O- and B-type stars (Figure 1.4). The balance between OB-type stars and the other type stars is very important, and if OB-type stars are more populated in a galaxy, the β value of the galaxy becomes bluer. In other words, the older-age galaxies tend to be redder in the β value due to the short life time of OB-type stars. Furthermore, the β value becomes much redder when the SFH of the galaxies is not continuous star formation, i.e. single instantaneous burst for the extreme case. The (stellar) metallicity also influences the β value since the hardness of the stellar spectrum depends on the metallicity. The effective temperature of the stars decreases with increasing the metallicity, and then the galaxies with high metallicity tend to be redder in the β value (Figure 1.1). Note that the influence from the metallicity is much smaller than the influence from the age and/or SFH. In addition to these stellar origin β variation (or we can call them *intrinsic* β variation), the rest-frame UV light is strongly affected by dust obscuration. The amount of the dust obscuration and its wavelength dependence are characterized by the dust attenuation value, Av or E(B-V), and the assumed dust extinction curve such as Milky

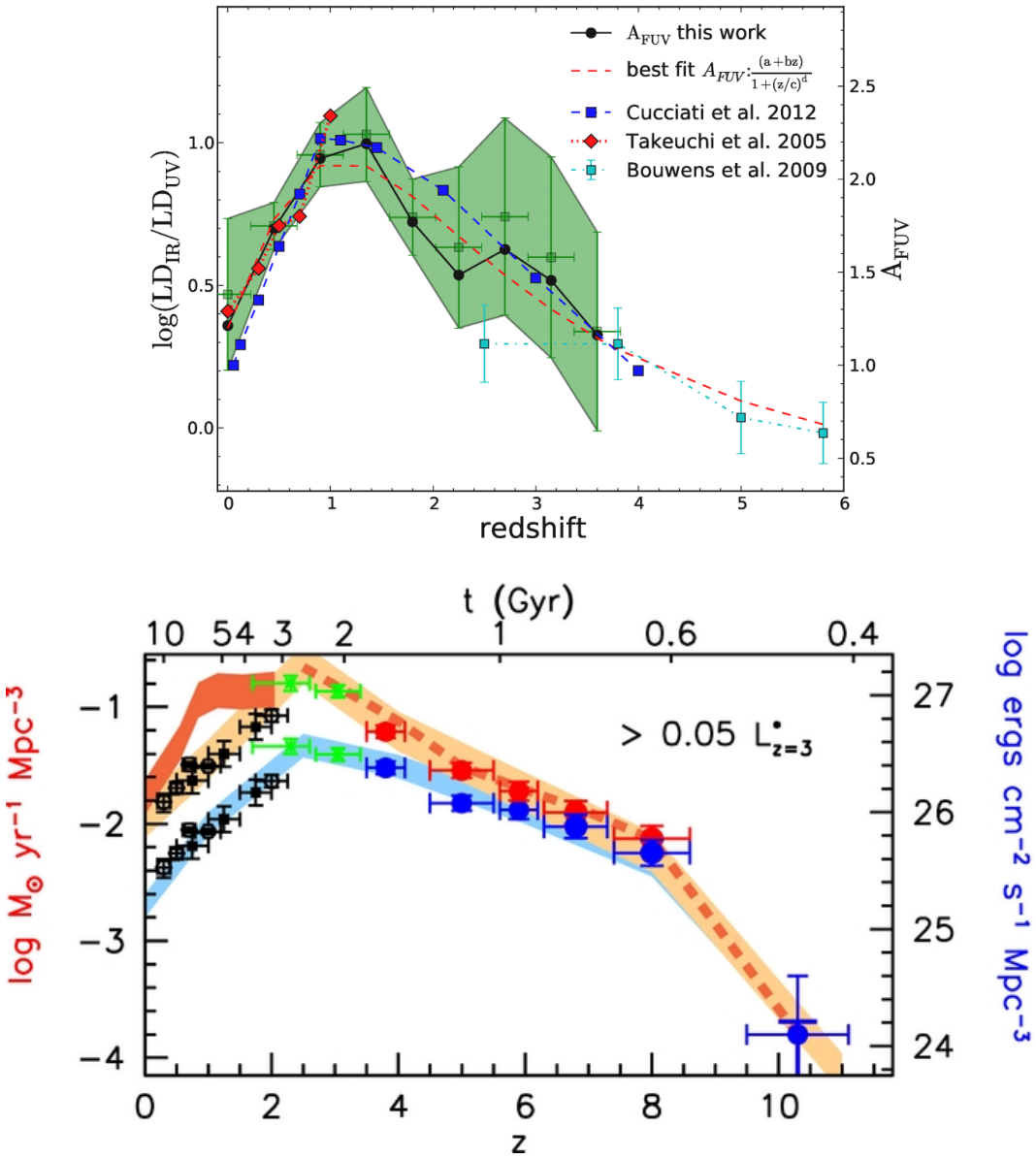

Figure 1.3: Top: The IRX value (left axis) or the Far-UV (FUV) dust attenuation (right axis) are plotted as a function of redshift. The black dots are calculated by integrating the luminosity function, and the green dots and green filled area show the mean and uncertainties computed from the bootstrap resampling method. Bottom: The SFRD (left axis) or luminosity density (right axis) as a function of redshift is shown. The SFRD is computed from the rest-frame UV luminosity density. The blue points and shaded region represent the *observed* SFRD, and the red points and shaded region represent the *dust-corrected* SFRD by applying the dust correction estimated from the M99 IRX-β relation. The black points are taken from previous literature. The dark red dashed line and shaded region represent the contribution from the LIRG/ULIRG population. *The Top figure is taken from Burgarella et al. (2013), reproduced with permission © ESO. The Bottom figure is taken from Bouwens et al. (2012), reproduced by permission of the AAS.*

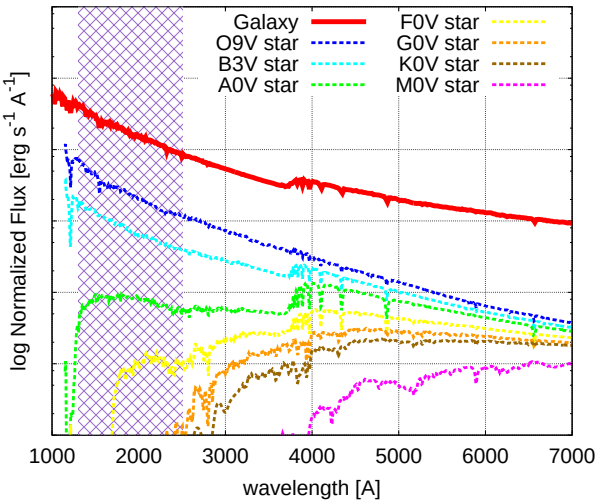

Figure 1.4: The contribution to the whole galaxy spectrum from the various type stars. The vertical axis shows the normalized flux in the unit of erg $s^{-1}Å^{-1}$ in a logarithmic scale and the horizontal axis shows the rest-frame wavelength in the unit of Å. The red solid line shows the example spectrum of a star-forming galaxy. The seven colored dotted-lines represent the different type stars described in the panel. The purple hatched area represents the wavelength range used for calculating the β value.

Way (MW), Large Magellanic Cloud (LMC), Small Magellanic Cloud (SMC), and starbursts (Calzetti et al. 2000). The β variation from the dust obscuration is comparable to or larger than the β variation from the age and/or SFH of galaxies. Therefore, there is difficulty in deducing the stellar population from only the observed β value, especially for the galaxies with redder β values ($\beta \gtrsim -2.0$), since the effect of the dust obscuration on the color of the galaxy is degenerated with the age. It is essential to resolve these degeneracy in order to confirm whether the observed UV spectral slope β really traces the stellar population, or not.

One of the way to avoid the degeneracy is the Spectral Energy Distribution (SED) fitting analysis. Although we need a multi-band photometry catalog for this analysis, we can deduce the stellar population of galaxies by modeling the broad-band SED. In particular, older-age star-forming galaxies tend to have the strong Balmer Break (at rest-frame $\lambda \sim 3600$), and the strong spectral feature is an important clue to resolve the degeneracy between dust and age. Erb et al. (2010) perform the SED fitting analysis for the star-forming galaxy at $z_{spec} = 2.3048$ which is very blue in the β value ($\beta = -2.1$). The authors find that the blue galaxy have the extraordinary conditions of a young age (< 100Myr), low mass ($M_* \sim 10^9 M_\odot$), and unreddened ($E(B-V) \simeq 0.02$). In the paper, the spectroscopic observation also shows that the galaxy has the low metallicity ($Z \sim 1/6 Z_\odot$) and relatively low SFR ($15 M_\odot$/yr). de Barros et al. (2016) and Naidu et al. (2016) also do the same analysis for the blue star-forming galaxies at $z_{spec} = 2-3$, and obtain the similar dust attenuation value, stellar mass, and metallicity, but the relatively older age ($\sim$ a few $\times$ 100Myr). We, however, note that the target galaxies in de Barros et al. (2016) and Naidu et al. (2016) are a highly Lyman Continuum leaking galaxy (see also Section 6.2), and the targets perhaps have the unusual

properties compared with the typical star-forming galaxies. Hathi et al. (2016) investigate the star-forming galaxies at $z_{spec} = 2 - 2.5$ selected from the spectroscopic sample of the VIMOS Ultra Deep Survey. The authors find that the galaxies with the red β value tend to have the higher dust attenuation value and higher stellar mass. Consequently, the UV spectral slope β can roughly trace the stellar population of star-forming galaxies; namely, the blue galaxies have the properties of less dust attenuation and low stellar mass, and most likely have moderately young age and low metallicity.

1.2.2 *Dusty Star-Forming Galaxies and UV Spectral Slope β*

Another important study about the UV spectral slope β is 'IRX-β relation'. The dust attenuation value can be directly estimated from the measurement of the dust thermal emission without complicated assumptions such as dust extinction curve and underlying stellar population, and thus the relation between the dust attenuation in star-forming galaxies and the β value has long been studied. Meurer et al. (1999, hereafter M99) investigate the relation between the β value and the ratio of total (or bolometric) InfraRed (IR) luminosity, $L_{\rm TIR}$, to UV luminosity, $L_{\rm UV}$ (called IRX; IRX $= L_{\rm TIR}/L_{\rm UV}$) for local starburst galaxies, and find that there is a relatively tight correlation between β and IRX (called IRX-β relation; Figure 1.5 Left). Within a galaxy, UV photons are absorbed by dust and re-emitted at the IR wavelength range as the dust thermal emission. Therefore, the IRX value is a direct indicator of the dust obscuration and can be converted to the dust attenuation value. Until now, the IRX-β relation has been studied and discussed for the star-forming galaxies from local to up to $z \sim 3$ (Figure 1.5 Right; e.g., Overzier et al. 2011; Takeuchi et al. 2012; Heinis et al. 2013; Casey et al. 2014; Álvarez-Márquez et al. 2016). Although there are some differences in the IRX-β relation among the literature, the typical star-forming galaxies are roughly distributed on the similar relation.

For the star-forming galaxies at $z \gtrsim 4$, the IRX-β relation is not investigated since there are difficulties in identifying the counterparts of the galaxies at the wavelength of the dust thermal emission. First, the current instruments for Mid-IR (MIR), Far-IR (FIR), and Sub-Millimeter wavelength range have the coarse spatial resolution ($\gtrsim 10''$) than the optical/NIR instruments ($\lesssim 1''$) except for the Atacama Large Millimeter/submillimeter Array (ALMA). Second, it is difficult to detect the dust thermal emission by the current instruments at the MIR and FIR wavelength range due to the positive K-correction. Finally, the galaxies at higher redshift may show the weak dust thermal emission. Indeed, the observation with ALMA indicates that the IRX value of *typical* star-forming galaxies at $z \gtrsim 4$ is significantly smaller than the IRX value expected from the M99 IRX-β relation although the sample size and survey area are not large enough (Capak et al. 2015; Bouwens et al. 2016b). It is not clear whether the IRX-β relation is really applicable to the high-z star-forming galaxies. Nevertheless, applying the M99 IRX-β relation to the star-forming galaxies at $z \gtrsim 4$, Bouwens et al. (2009, 2012) find the evolution of the dust obscuration from $z \sim 7$ to $z \sim 4$. Burgarella et al. (2013) investigates the UV and IR luminosity function from $z = 0$ to $z = 4$, and shows that the IRX value peaks at $z \sim 1.2$ (Figure 1.3 Top). Interestingly, the result of Burgarella et al. (2013) is continuously connected to the results of Bouwens et al. (2009). Therefore, it implies a cosmic dust attenuation history: the dust obscuration increases from $z = 0$, peaks

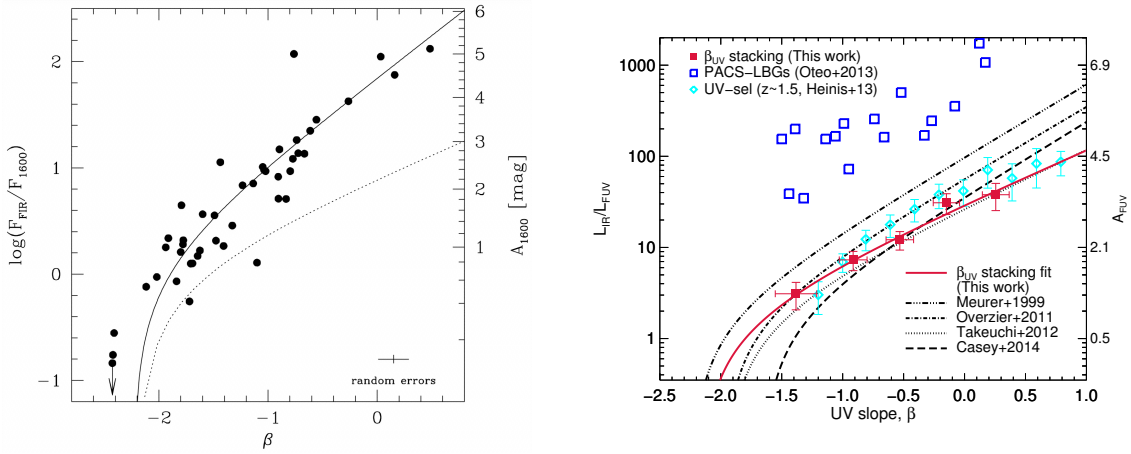

Figure 1.5: IRX-β diagram for local starbursts (Left) and high-z LBGs (Right). Left: The left axis is the IRX value and the right axis is the corresponding dust attenuation at $\lambda = 1600$Å. The black dots represent individual local starbursts, and the black solid line indicates the IRX-β relation proposed in Meurer et al. (1999). The black dotted line indicates the suggested model of Pettini et al. (1998). Right: The left axis is same as the Left panel and the right axis is the corresponding dust attenuation at *GALEX*/FUV-band. The red filled squares and solid line represent the stacked results and its best-fit function for LBGs at $z \sim 3$ (Álvarez-Márquez et al. 2016). The blue open squares denote the individual *Herschel*/PACS-detected LBGs at $z \sim 3$ (Oteo et al. 2013). The cyan open diamonds denote the stacked results for UV-selected galaxies at $z \sim 1.5$ (Heinis et al. 2013). The black various lines show the results for local starbursts from M99 (triple-dot-dashed line), Takeuchi et al. (2012, dotted line), Overzier et al. (2011, dot-dashed line), and Casey et al. (2014, dashed line). *The Left figure is taken from Meurer et al. (1999), reproduced by permission of the AAS. The Right figure is taken from Álvarez-Márquez et al. (2016), reproduced with permission* © *ESO.*

at $z \sim 1.2$, and decreases toward higher redshift, at least up to $z \sim$ 6-7.

While the IRX-β relation has a uncertainty for the high-z star-forming galaxies, even at $z \sim$ 2-3 the IRX value of the DSFGs also deviates from the IRX-β relation toward the higher IRX value (Figure 1.5 Right; e.g., Reddy et al. 2006; Chapman et al. 2005; Oteo et al. 2013). It means that the DSFGs at $z \sim$ 2-3 are dustier than the typical starbursts at $z \sim 0$ and the DSFGs at $z \sim 1$ although the observed β value is similar among the galaxies. The DSFGs are identified as Luminous InfraRed Galaxies (LIRGs), Ultra LIRGs (ULIRGs), SMGs, and/or simply FIR-detected galaxies, which emit the bulk of their energy at the rest-frame IR wavelength. The LIRG/ULIRG population is characterized by their total IR luminosity, and the LIRGs/ULIRGs are the galaxies with $10^{11} L_\odot < L_{\rm TIR} < 10^{12} L_\odot$ and $10^{12} L_\odot < L_{\rm TIR} < 10^{13} L_\odot$, respectively. These populations have been studied by using the MIR and FIR space telescopes (e.g., *IRAS*, Neugebauer et al. 1984; *ISO*, Lemke et al. 1996; *Spitzer*, Rieke et al. 2004; *Herschel*, Griffin et al. 2010, Poglitsch et al. 2010), and the intense IR emission is fueled by star formation and/or Active Galactic Nuclei (AGNs). The fraction of LIRGs/ULIRGs with AGN increases with their IR luminosity, and at least $\sim$ 50% of ULIRG population with $L_{\rm TIR} > 10^{12.3} L_\odot$ have the signature of AGN (Veilleux et al. 1995, 1999; Yuan et al. 2010). Moreover, all the LIRGs/ULIRGs with $L_{\rm TIR} > 10^{11.5} L_\odot$ at local universe show

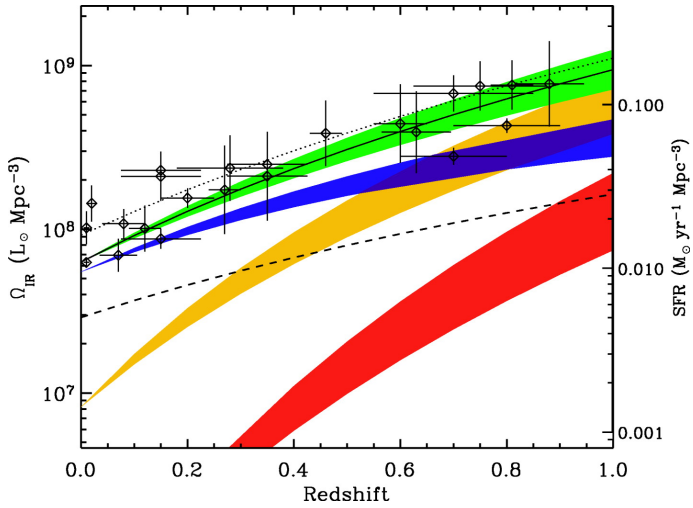

Figure 1.6: Comoving IR luminosity density as a function of redshift for several populations. The left vertical axis is the IR luminosity density and the right vertical axis is the corresponding SFRD. The green, blue, orange, and red filled regions denote the all galaxies, low-luminosity galaxies with $L_{\rm TIR} < 10^{11} L_\odot$, IR luminous galaxies ($L_{\rm TIR} \geq 10^{11} L_\odot$; LIRGs + ULIRGs), and ULIRGs ($L_{\rm TIR} \geq 10^{12} L_\odot$), respectively. The black dashed line represent the SFRD calculated from the NOT dust-corrected UV luminosity. The black diamonds with error bars show the SFRD obtained from previous literature. *The figure is taken from Le Floc'h et al. (2005), reproduced by permission of the AAS.*

a signature of major or minor mergers (Larson et al. 2016). Therefore, the major merger of gas-rich galaxies can be a dominant process igniting the star formation and/or AGN, and this event is understood as a part of the formation and evolution scenario of local massive ellipticals; the interaction of galaxies causes the LIRG/ULIRG phase which is followed by the AGN/quasar phase, and then massive ellipticals are formed after the termination of star formation and AGN through dry minor mergers (Sanders et al. 1988; Hopkins et al. 2008). The SMG population is the objects detected at the observed-frame sub-millimeter wavelength (typically $\lambda_{obs} \sim 250\mu$m-2mm). The SMGs were first discovered with the Submillimeter Common User Bolometer Array (SCUBA; Holland et al. 1999) on the James Clerk Maxwell Telescope (JCMT), and the SMGs were defined as 850μm-detected galaxies. Although there is a difficulty in identifying the counterparts of SMGs, the redshift distribution of SMGs is studied and seems to have a peak at $z \sim 2.5$ for 850μm- and 1.1mm-detected SMGs (Chapman et al. 2005; Chapin et al. 2009; Banerji et al. 2011; Wardlow et al. 2011; Yun et al. 2012; Simpson et al. 2014). Therefore, the SMG population is considered as the higher-redshift LIRG/ULIRG population, namely a kind of the DSFGs.

The prominent IR emission of the DSFGs comes from the dust thermal emission heated by strong internal UV emission, and hence most of the UV light (or star formation) in the DSFGs are hidden by thick dust. It is important to reveal such hidden star formation and its contribution to the cosmic SFRD. Le Floc'h et al. (2005) find that the contribution of the IR-luminous sources ($L_{\rm TIR} \geq 10^{11} L_\odot$; LIRGs + ULIRGs) to the total IR luminosity density sharply increases from $z = 0$ to 1, and it reaches 70% at $z \sim 1$ (Figure 1.6). The contribution

of the ULIRGs also increase from $z = 0$ to 1, but it is modest ($\sim$ 10% at $z \sim 1$). The authors also show that the cosmic SFRD converted from the total IR luminosity density (the green region in Figure 1.6) is much higher than the cosmic SFRD estimated from the not dust-corrected UV luminosity (the black dashed line) over the redshift range. Magnelli et al. (2011, 2013) extend this study and show that the contribution of the ULIRGs to the total IR luminosity density continues to increase from $z = 1$ to 2 and reaches 50% at $z \sim 2$, although the contribution of the LIRGs is 50% at $z \sim 1$ and 30% at $z \sim 2$. Therefore, the IR-luminous galaxies dominate the cosmic SFRD at z = 0-2, and particularly the contribution from the LIRGs/ULIRGs becomes much higher toward higher redshift (up to $z \sim 2$). Note that, in the conversion from IR luminosity to SFR, the authors assume that the origin of the dust thermal emission is attributed to star formation, and does not consider the contribution from AGNs to the IR luminosity.

Gruppioni et al. (2013) investigate the total IR luminosity density over the wider redshift range ($0 < z < 4$), and show that the total IR luminosity density steeply increases from $z = 0$ to 1, flattens between $z \sim 1$ and 3, and decreases toward higher redshift ($z > 3$). Madau & Dickinson (2014) compile a number of results from previous literature and show the global history of the cosmic SFRD (Figure 1.3 Bottom). However, at $z \gtrsim 4$ the cosmic SFRD relies on the *dust-corrected* UV luminosity whose dust attenuation value is estimated from the M99 IRX-β value (Bouwens et al. 2012). In conclusion, the DSFGs play a critical role in the history of the dust attenuation and the cosmic SFRD. In order to reveal the nature of star formation at $z \gtrsim 4$, it is necessary to place a strong constraint on the dust attenuation in star-forming galaxies at $z \gtrsim 4$.

1.3 *Spatial Clustering*

In the Λ Cold Dark Matter (ΛCDM) universe, the large-scale structure is hierarchically formed through the mergers of dark matter halos across cosmic time. Since galaxy formation and evolution are closely linked to the structure formation, the information of galaxy spatial clustering can provide an unique insight into the assembly history of dark matter and baryon mass. In general, the spatial clustering is quantified by two-point correlation function. The separation of pairs is customary described by the real-space vector $\boldsymbol{r}$ or the redshift-space (z-space) vector $\boldsymbol{s}$ in comoving coordinates. If we know the redshift for all target galaxies, we can measure the z-space correlation function, $\xi(s)$, the z-space two-dimensional (2-D) correlation function, $\xi(\sigma, \pi)$, and the projected correlation function, $\omega_p(\sigma)$. In the last two correlation functions, σ and π represent the separation distance of pairs transverse and parallel to the line-of-sight, respectively[2]. Otherwise we cannot always know the redshift information for all targets, and instead we measure the angular correlation function (ACF), $\omega(\theta)$, in which θ represents the separation angle of pairs. In any case, the main purpose of the clustering analysis is to infer the real-space correlation function, $\xi(r)$, which is ordinary characterized by a power-law of the form $\xi(r) = (r/r_0)^{\gamma}$, and then the final goal is to estimate the correlation length, r_0, and the correlation slope, γ. By combining the ΛCDM model with the clustering

[2]In some literatures, authors use r_p as the perpendicular component of the separation distance of pairs instead of σ.

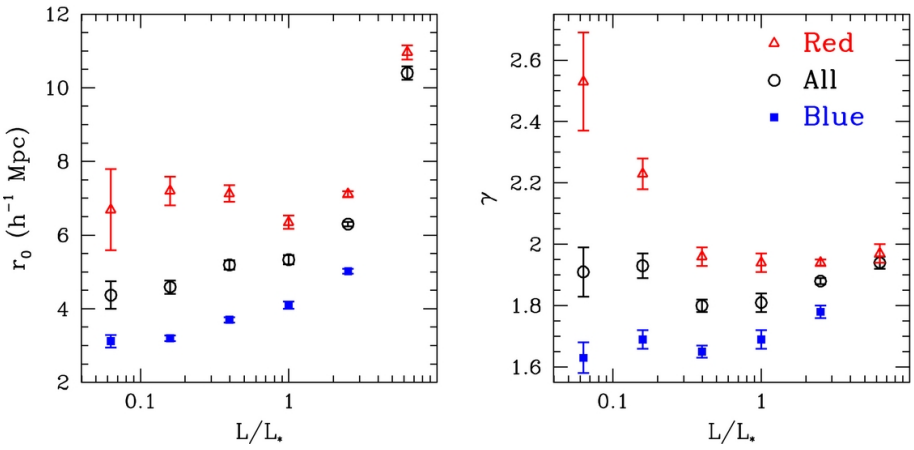

Figure 1.7: The clustering correlation length (Left) and slope (Right) are shown as a function of the optical luminosity for the different optical color samples at $z < 0.25$. The black open circles, red open triangles, and blue filled points represent the samples of whole galaxies, optical red galaxies, and optical blue galaxies, respectively. The red and blue galaxies are defined by $g - r = 0.21 - 0.03M_r$. The luminosity is calculated from r-band magnitude, and for computing the correlation function the samples are divided into each luminosity bin. Therefore, the number of galaxy is significantly small at the faintest bin. *The figure is taken from Zehavi et al. (2011), reproduced by permission of the AAS.*

analysis, we can interpret the results as the mean dark matter halo mass and/or galaxy-dark matter bias of the target galaxies.

The larger clustering length and steeper clustering slope mean the higher mean dark matter halo mass hosting target galaxies. The mass of the host dark matter halos is expected to depend on the type of the galaxy population, and thus the two-point correlation function can have variations as a function of redshift, luminosity, color, morphology, SFR and stellar mass of galaxy sample. It is generally accepted that the galaxies which are luminous in rest-frame optical/UV, red in rest-frame optical, early-type, higher SFR, and higher stellar mass are more clustered than the galaxies which are less luminous, blue, late-type, lower SFR, and lower stellar mass (Figure 1.7; e.g., Bethermin et al. 2014; Kashikawa et al. 2005; Ouchi et al. 2004, 2005; Zehavi et al. 2011). Furthermore, comparing the correlation function for the various type of galaxies, we can deduce the origin of the galaxy population. For example, Bielby et al. (2016) investigate the angular auto- and cross-correlation function of LBGs and LAEs at $z \sim 3$, and find that the clustering length of LBGs and LAEs are consistent at faint UV continuum magnitude. Finally the authors conclude that LAEs are a low-luminosity subset of LBGs in their sample. As another example, Hickox et al. (2012) investigate the cross-correlation function between SMGs and *Spitzer*/IRAC detected-galaxies, and find that the clustering length of SMGs is similar to that of QSOs at the same redshift assuming the clustering slope of $\gamma = 1.8$. The authors conclude that the SMGs and QSOs occur in the same systems. In these ways, the clustering analysis is used for revealing the nature of galaxy formation and evolution.

For understanding the detailed relationship between observed galaxies and invisible dark

matter halos, the important framework is the Halo Occupation Distribution (HOD; e.g., Peacock & Smith 2000; Berlind & Weinberg 2002). The HOD modeling describes the number of galaxies, N, in a dark matter halo of virial mass, M, by the conditional probability distribution, $P(N \mid M)$. In this model, galaxies are classified into two categories according to the location of the galaxies within a host dark matter halo. One is the *central* galaxy, which is at or near the center of the host dark matter halo, and the other is the *satellite* galaxies, which reside in the same host halo but not near the center. The satellite galaxies is also considered to be hosted in subhalos which are gravitationally bound distinct halos within the larger host halo (Kravtsov et al. 2004). According to the HOD formalism, the signal of the two-point correlation function on scales smaller than a typical halo size is produced by the pairs of central and satellite galaxies which reside in a same host halo. This component is called the 'one-halo' term. On the other hand, the signal on scales larger than a typical halo size is attributed to the pairs of galaxies which reside in two different halos. This component is called the 'two-halo' term. By cosmological N-body simulations, the prominent excess of the one-halo term compared with the two-halo term is predicted for the galaxies at higher redshift ($z \gtrsim 1$; Kravtsov et al. 2004). The simulations also indicate that the power-law shape correlation function, $\xi(r) = (r/r_0)^{\gamma}$; which is observed in the local universe so far, is formed from the specific balance between the one- and two-halo terms (Berlind & Weinberg 2002). Indeed, the previous observational studies for high redshift galaxies ($z \sim 3-4$) show that the ACF (or projected correlation function) deviate strongly from a power-law on the small scales (e.g., Ouchi et al. 2005; Bielby et al. 2011, 2013). Moreover, even at $z = 0$ the small departures from a power-law on the small scales are also reported by Zehavi et al. (2004). Consequently, the framework of HOD is a powerful theoretical model to interpret the observed two-point correlation function, and to provide the strong constraint on the environment of galaxies.

As mentioned in Section 1.2, the UV spectral slope β strongly depends on the stellar population of star-forming galaxies. Particularly, if a galaxy shows the extremely blue β value ($\beta < -3.0$), the stars in the galaxy are formed from less metal-polluted HI gas and the galaxy is extremely young and nearly dust-free (perhaps, for the extreme case, the galaxy can be a *primordial galaxy* which is dominated by metal-free PopⅢ stars). In a given epoch, it is considered that such an extremely blue stellar system is hosted in less massive dark matter halo and tends to be less clustered than the redder stellar system, or may be isolated. Consequently, the clustering power of the galaxies with blue β value (namely, blue color in rest-frame UV) becomes smaller than that of the galaxies with red β value. Although the previous works compare the optically red (quiescent) galaxies with the optically blue (star-forming) galaxies, the comparison between the blue and red star-forming galaxies is not investigated. Assuming the above relation between the UV spectral slope β and the spatial distribution, the β value should show the variations of the clustering amplitude and slope, and can be used as a probe of the mass assembly and metal enrichment.

1.4 *Direction of This Work*

The UV spectral slope β represents the hardness of the UV continuum flux of star-forming

galaxies, and the measurement of the β value is relatively simple even for the galaxies at higher redshift. Bellow, we briefly summarize the introductions, issues, and motivations.

- ◇ According to recent works, the β value is measured for high-z star-forming galaxies ($z \sim 3-7$), and the β-z relation and β-$M_{\rm UV}$ relation is well investigated especially for the faint star-forming galaxies. On the other hand, the β-$M_{\rm UV}$ relation for the luminous star-forming galaxies is not sufficiently investigated due to the small FoV of the *HST* imaging data set. It is required to study the β-$M_{\rm UV}$ relation for luminous high-z galaxies by using wide field imaging data.
- ◇ We can roughly deduce the stellar population of star-forming galaxies from the β value. In particular, the IRX-β relation is useful for estimating the dust attenuation value although we need more discussions on the validity of the relation for high-z galaxies and DSFGs. We should investigate the relation between the β value and the stellar population in detail for higher redshift galaxies.
- ◇ The spatial clustering depends on the mass assembly of DM halos. The extremely blue β systems can trace the less massive DM halos, and thus we probably identify the differences of the spatial clustering between the red and blue β systems.

On the basis of the motivation, we focus on **Lyman Break Galaxies (LBGs) at redshift 4** ($3.5 < z < 4.5$) which is the boundary redshift accessible to the dust thermal emission by current IR instruments. It is worth investigating the stellar population of $z \sim 4$ LBGs in detail by using the SED fitting analysis.

In the following, we briefly explain the structure of this paper. In Section 2, we show detailed informations of imaging data. Our target field is the Subaru/XMM-Newton Deep Survey (SXDS) field which is partially covered by other surveys. Thus, the informations of all the imaging data we use in this research are shown. In Chapter 3, the procedures for calculating the UV spectral slope β, making a photometric catalog, and the clustering analysis are explained. In Chapter 4, we show the result of the observed β distribution. The purpose of this analysis is to investigate the trend of β-$M_{\rm UV}$ relation and justify it. For the justification, we also show the result from Monte-Carlo simulations which compute the detectability of star-forming galaxies by taking account of our adopted selection criteria. In Chapter 5, we first show some examples of the SED fitting analysis and consider its validity. Then we discuss the intrinsic UV spectral slope β and the stellar population. After that, in order to verify our analysis, we discuss the dependence of the β-$M_{\rm UV}$ relation on SFHs and we check the distribution of our sample on a color-color diagram which is calculated by using a population synthesis model. Finally, we discuss the dust attenuation law of high-z star-forming galaxies. In Chapter 6, we show a result of the clustering analysis and mention its future prospect. Moreover, we also mention the EW(Hβ)-β method as the other future prospect which has a great potential to reveal the source of reionization.

Last of all, in regard to the cosmological parameters, we assume $\Omega_{m,0} = 0.3$, $\Omega_{\Lambda,0} = 0.7$, $H_0 = 70$ km s^{-1} Mpc^{-1}. Throughout this paper, we apply the AB magnitude system (Oke & Gunn 1983; Fukugita et al. 1996).

Chapter 2

DATA

The SXDS field is one of the deep and wide survey field observed with Subaru/Suprime-Cam *B, V, R, i′, z′*-band (Furusawa et al. 2008). The survey area is as large as 1deg^2, and this field is partially covered by other deep surveys, i.e., UDS-UKIDSS/UKIRT, UDS-CANDELS/*HST*, and SEDS/*Spitzer* (Figure 2.1). In addition to the archival SXDS data, we used the data of updated-z' from Subaru/Suprime-Cam, *J, H*, and *K* from UKIRT/WFCAM, F125W and F160W from *HST*/WFC3, and 3.6μm and 4.5μm from *Spitzer*/IRAC. The updated-z' band images are new ones observed by the updated CCD (Furusawa et al. 2016) and $\sim$ 0.5 mag deeper than the archival SXDS data. The *J, H*, and *K*-band images are taken from the UKIRT Deep Sky Survey (UKIDSS; Lawrence et al. 2007) DR10 in which this field is observed as the Ultra Deep Survey (UDS) field. The F125W and F160W band images are taken from the Cosmic Assembly Near-Infrared Deep Extragalactic Legacy Survey (CANDELS; Grogin et al. 2011; Koekemoer et al. 2011). The 3.6μm and 4.5μm band images are taken from the Spitzer Extended Deep Survey (SEDS; Ashby et al. 2013). In this work, we made a photometry catalog of the SXDS field by ourselves. The detailed procedure is described in Section 3.2.

The imaging data set in the SXDS field covers the very large wavelength range from $\sim$ 4000Å to $\sim$ 45000Å in the observed-frame. In terms of the survey depth, survey area, and wavelength coverage, the SXDS field is quite unique compared with other surveys and the best survey field in order to investigate the stellar population of high-redshift galaxies. In particular, the deepest *J*, *H* and *K*-band images are very useful to constrain the stellar population of $z \sim 4$ galaxies because the wavelength range of *JHK*-band covers the wavelength of Balmer Break for $z \sim 4$ galaxies (see also Figure 3.1).

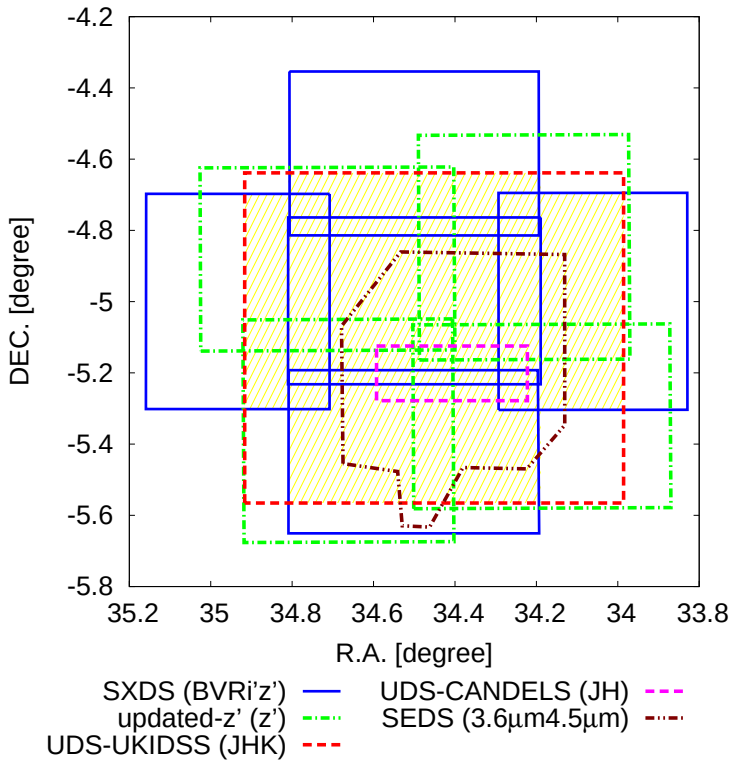

Figure 2.1: Field map of imaging data used in our analysis. The blue solid lines, which make the five open rectangles, show the sky coverage of the SXDS/Subaru field; the green dot-dashed lines, which make the four open rectangles, represent the sky coverage observed with Subaru/updated-z'; The red dashed line, which make the large open square, represents the sky coverage of the UDS-UKIDSS/UKIRT field; the magenta dashed line, which make the smallest rectangle, represents the sky coverage of the UDS-CANDELS*HST* field; and the brown two-dot-dashed line, which make the polygon, represents the sky coverage of the SEDS/*Spitzer* field. Our catalog consists of the objects within the area covered by all of the SXDS, updated-z', and UDS field since we used the i', z', updated-z', and J-band photometry for estimating the β value. This area is filled by the yellow slanting lines.

Table 2.1: Summary of Original Data.

Name of Field	Instrument	Filter	Lim. Mag. (5σ, AB)	PSF FWHM (arcsec)
SXDS	Subaru/Suprime-Cam	B	~ 27.5[a]	0.8
SXDS	Subaru/Suprime-Cam	V	~ 27.1[a]	0.8
SXDS	Subaru/Suprime-Cam	R	~ 27.0[a]	0.8
SXDS	Subaru/Suprime-Cam	i'	~ 26.9[a]	0.8
SXDS	Subaru/Suprime-Cam	z'	~ 25.8[a]	0.7
	Subaru/Suprime-Cam	updated-z'	26.5[b]	1.0
UDS-UKIDSS	UKIRT/WFCAM	J	25.5[b]	0.8
UDS-UKIDSS	UKIRT/WFCAM	H	24.9[b]	0.8
UDS-UKIDSS	UKIRT/WFCAM	K	25.2[b]	0.8
UDS-CANDELS	*HST*/WFC3	F125W	25.6[b]	0.12
UDS-CANDELS	*HST*/WFC3	F160W	25.6[b]	0.18
SEDS	*Spitzer*/IRAC	3.6μm	24.75[c]	1.8
SEDS	*Spitzer*/IRAC	4.5μm	24.8[c]	1.8

[a] Derived from Furusawa et al. (2008). This value is measured with $2''\phi$ random aperture for original (not PSF-matched) images.

[b] Measured by SY with $2''\phi$ for PSF-matched images. Although there is a little difference of limiting magnitude between the FoVs for each broad-band filter, the difference is negligible.

[c] Derived from Ashby et al. (2013). This value represents the typical total magnitude where the completeness of the source detection is 50%.

Chapter 3

ANALYSIS

3.1 *Measurements of UV Spectral Slope* β

First of all, I describe the method for the measurement of the UV spectral slope β. According to the original definition of Calzetti et al. (1994), the β value should be estimated from the Spectral Energy Distribution (SED) from ∼1250 Å to ∼2600 Å thorough the 10 fitting windows (Figure 3.1 Left and Table 3.1). However it is impractical to accurately measure the continuum flux from spectroscopic data for all the targets. Instead we apply the simple power-law fitting to the broad-band photometry with the following functional form,

$$M(\lambda_x) = -2.5\ (\beta + 2)\ \log\lambda_x + Const \tag{3.1}$$

where λ_x is the effective wavelength of xth broad-band filter, $M(\lambda_x)$ is the measured magnitude of xth broad-band filter, and *Const* is a constant value. This method is suitable since the bias in the β estimation is small (Finkelstein et al. 2012a; Rogers et al. 2013). For the fitting, we conducted the least square fitting to the at least three broad-band filters which cover the rest-frame wavelength from $\sim$ 1500 to $\sim$ 2500Å. Although using the larger number of the photometric data points results in more accurate determination of the β value, we need to select the optimal broad-band filters for the fitting so as to avoid strong spectral features. In the rest-frame UV wavelength range, the redshifted Lyα ($\lambda = 1216$Å) line and Balmer Break ($\lambda \sim 3600$Å) can be a contamination affecting the broad-band photometry. For example, when we calculate the β values of $z \sim 4$ galaxies, the R ($\lambda \sim 6000 - 7000$Å) and H ($\lambda \sim 15000 - 17000$Å) band filters are probably affected by the strong spectral features (Figure 3.1 Right). Consequently, we used the i', z', updated-z', and J-band filters for the objects in the SXDS filed, the R, i' and z'-band filters in the SSA22 field, and the i, z, y-band filters in the ELAIS-N1 fields. Throughout the paper, the β value is calculated by the above method and filter sets unless otherwise stated.

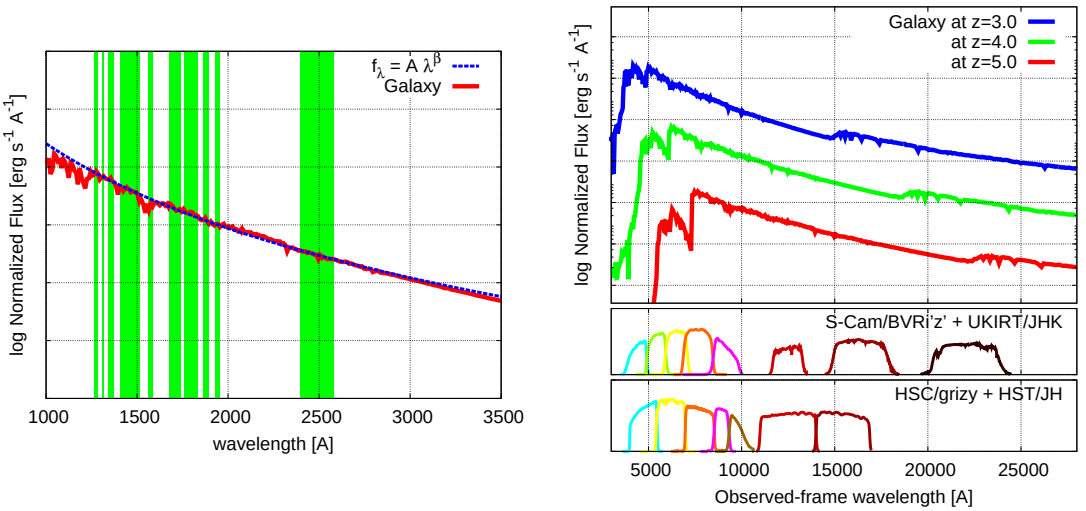

Figure 3.1: Left: Fitting window for calculating the β value defined in Calzetti et al. (1994). The red solid line shows the sample spectrum of a star-forming galaxy, and the blue dotted line denotes the best-fit function of $f_\lambda \propto \lambda^\beta$. The vertical axis represents the normalized flux in the unit of erg s^{-1}Å^{-1}, and the horizontal axis represents the rest-frame wavelength in the unit of Å. Right: Sample spectra for star-forming galaxies at different redshifts (Top), and the response curves of broad-band filters used in our analysis (Middle and Bottom). In the top panel, the blue, green, and red solid lines show the spectra of the star-forming galaxies at $z = 3$, 4, and 5, respectively. The vertical axis is same as left panel, but the horizontal axis represents the observed-frame wavelength in the unit of Å. In the middle panel, from left to right the response curve of Subaru/Suprime-Cam $BVRi'z'$-band and UKIRT/WFCAM JHK-band are shown. In the bottom panel, from left to right the response curve of Subaru/HSC $grizy$-band and HST/WFC3 JH-band are shown.

Table 3.1: Fitting Window defined in Calzetti et al. (1994), *reproduced by permission of the AAS.*

Window No.	Wavelength Range [Å]
1	1268−1284
2	1309−1316
3	1342−1371
4	1407−1515
5	1562−1583
6	1677−1740
7	1760−1833
8	1866−1890
9	1930−1950
10	2400−2580

3.2 *Photometric Catalog for SXDS Field*

3.2.1 *Photometry*

In this study, we made a photometric catalog which includes the photometry from SXDS/B to SEDS/4.5μm (the data is summarized in Table 2.1). For the data from B to K band, we measured 2″-diameter aperture magnitude by using the SExtractor[1] ver.2.5.0 (Bertin & Arnouts 1996). Before measuring the photometry, the smaller PSF images are convolved with Gaussian kernels to be matched in FWHM of the stars (1″.0) with the original updated-z' band image. For the 3.6μm and 4.5μm photometry, we used the photometry from the archival catalog made by Ashby et al. (2013) after applying aperture correction. Finally, we picked up the objects which are in the overlapped region covered by both the SXDS and UDS-UKIDSS fields (Figure 2.1; the overlapped region is filled by yellow slanting lines) because we need both optical and NIR photometry for estimating the UV spectral slope βvalue of $z \sim 4$ galaxies.

3.2.2 *Sample Selection*

From the above photometric catalog, we selected the objects satisfying all the following criteria.

(1) $i' \leq 26.0$
(2) updated-z', and J band detected
(3) $B - R > 1.2$, $R - i' < 0.7$, and $B - R > 1.6\ (R - i') + 1.9$
(4) $3.5 \leq z_{phot} < 4.5$ with reduced $\chi^2 \leq 2$

The criteria (1) is applied so as to select the galaxies bright enough to have small photometric errors and the criteria (2) is required to estimate the β value accurately. The criteria (3) is the $BRi'-$LBG selection reported by Ouchi et al. (2004) and it is intended to pick up star-forming galaxies at z $\sim$ 4. In Ouchi et al. (2004), the LBG selection is investigated for the Subaru/Suprime-Cam filter set, and the detectability of $z \sim 4$ galaxies and the rate of the contamination from low-z galaxies are discussed. Therefore, at least for our data set, this selection is optimal. Up to this criteria, the total number of objects is $\sim$ 2100. The criteria (4) is applied so as to select the reliable galaxies at $z \sim 4$. The reduced χ^2 value is calculated for each galaxy from χ^2/d.o.f, in which d.o.f = (number of observed broad-band filters for each galaxy) $-$ (number of free parameters in the fitting). In the selection procedure, our concern is only the photometric redshift and thus we adopted the number of free parameters = 1. As a result, our catalog contains $\sim$ 1800 LBGs. In other words, 300 objects are rejected by the criteria (4), and most of the rejected objects have the χ^2/d.o.f > 2 or $z_{phot} \sim 0.5$.

3.2.3 *SED Fitting Analysis*

For the SED fitting analysis, in which we estimate the photometric redshift and the other physical quantities simultaneously, we used the 'Hyperz'[2] photometric redshift code ver.1.1

[1] `http://www.astromatic.net/software/sextractor`
[2] `http://webast.ast.obs-mip.fr/hyperz/`

(Bolzonella et al. 2000) with the Bruzual & Charlot (2003) templates[3] (hereafter BC03) and the STARBURST99[4] (Leitherer et al. 1999) templates (hereafter SB99). The BC03 templates are chosen as "typical galaxy" models and constructed from five different SFHs, fifteen age values, and three metallicity values with the Chabrier Initial Mass Function (IMF). The five SFHs are Single Burst with the finite time duration (=10Myr), Continuous Constant, and Exponentially Decline with τ=0.1Gyr, 2Gyr, and 5Gyr. The fifteen age values distribute between 2 Myr and 10 Gyr, and the three metallicity values are $Z = 0.02Z_{\odot}, 0.2Z_{\odot}$, and $Z_{\odot}$. The SB99 templates are adopted as "young star-forming galaxy" models and constructed from two SFHs, fifteen age values, four metallicity values, and two extreme nebular continuum cases with the Kroupa IMF. The two SFHs are Instantaneous Burst and Continuous Constant, the fifteen age values distribute between 0.01 Myr and 150 Myr, and the four metallicity values are $Z = 0.02Z_{\odot}, 0.2Z_{\odot}, 0.4Z_{\odot}$, and $Z_{\odot}$. In the run of the Hyperz, the dust attenuation value, Av, is ranged from 0.0 to 3.0 with ΔAv=0.1 assuming the Calzetti et al. (2000) attenuation law for dust extinction curve.

3.3 *Methodology of Clustering Analysis*

For studying clustering properties, we measure the angular auto-correlation function (hereafter we call this as ACF), $\omega(\theta)$, applying the formula of Landy & Szalay (1993).

$$\omega(\theta) = \frac{DD - 2DR + RR}{RR} \tag{3.2}$$

In this equation the term of DD, DR, and RR represents the number of pairs, which indicates data-data, data-random, and random-random object, respectively, with the separation between $\theta - \Delta\theta/2$ and $\theta + \Delta\theta/2$. The random object is generated from a random number which places within the effective survey area and we make the 200,000 random objects for the SXDS field. The ACF signals are calculated from $\theta \sim 2$ to $\theta \sim 1000$ arcsec with the binning of $\log \Delta\theta = 0.40$.

The errors of the ACF signals are estimated by using the bootstrap resampling method (Ling et al. 1986). In the bootstrap method, we pick up the data objects permitting repetition and make a data catalog which has the same number of objects as the original data catalog. We calculate $\omega(\theta)$ for the catalog by Eq.(3.2) and repeat this process 10,000 times. Finally we obtain the number distribution of $\omega(\theta)$ which provide the plausible value of $\omega(\theta)$ and the standard deviation of $\omega(\theta)$ as the error of the ACF signal.

For the quantitative discussion, we fit the observed ACF signals by the power-law form, $\omega(\theta) = A_{\omega}\theta^{1-\gamma}$, which is the fiducial model of the ACF. However, because of the limited survey area and shape, the observed ACF signals are underestimated compared with the intrinsic ACF signals and this offset can be quantified as the integral constant (IC; Groth & Peebles 1977). Therefore the observed ACF signals should be fitted by,

$$\begin{aligned} \omega_{obs}(\theta) &= \omega_{int}(\theta) - \mathrm{IC} \\ &= A_{\omega}(\theta^{1-\gamma} - \mathrm{IC}/A_{\omega}). \end{aligned} \tag{3.3}$$

[3] `http://www.bruzual.org/bc03/`

[4] `http://www.stsci.edu/science/starburst99/docs/default.htm`

This IC value can be calculated from,

$$\mathrm{IC} = \frac{1}{\Omega^2} \int \int \omega_{int}(\theta_{12}) \mathrm{d}\Omega_1 \mathrm{d}\Omega_2. \tag{3.4}$$

This equation is replaced to the following equation (Roche et al. 1999),

$$\mathrm{IC} = \frac{\sum RR(\theta)\omega_{int}(\theta)}{\sum RR(\theta)}. \tag{3.5}$$

When we know the index of γ, we can numerically calculate the IC/A_ω value from the random object sample. By using the least-square non-linear fitting method, we can estimate the A_ω, γ, and IC/A_ω value. In this paper we use the arcsec scale unit for the separation of the object pairs, thus the A_ω and IC/A_ω value have the arcsec unit.

Chapter 4

RESULTS

4.1 *Observed Distribution of UV Spectral Slope β*

Figure 4.1 shows the obtained distribution of the UV spectral slope β as a function of the UV absolute magnitude at rest-frame 1500Å (β-$M_{\rm UV}$ relation). The UV absolute magnitude for each object is calculated from the best-fit SED template by integrating the flux from rest-frame 1450Å to 1550Å. The green open squares show the objects in the area observed with *Spitzer* and the blue ones show the objects out of the area. There seems to be no notable systematic difference in the distribution of the sample with and without the SEDS/*Spitzer* data. The magenta filled squares with the error bars indicate the mean β value for each bin. The standard deviation of the β distribution is indicated by the thick marks toward the left side, and the typical uncertainty in the β value for the individual objects is shown by the thick marks toward the right side. For the mean values, we just apply the simple geometric mean without taking account of the individual uncertainty in β for the individual objects. This is because the mean β value can be biased toward positive values if we weight the β values by the individual uncertainty for the individual objects, i.e., the uncertainty is not symmetric and becomes smaller toward positive β values than the opposite. The mean β value, standard deviation, and typical uncertainty for each bin are summarized in Table 4.1.

Figure 4.2 shows the number histogram of the β value for each magnitude bin. The green and blue histogram represent the same objects as Figure 4.1. The red solid lines, magenta dashed-lines, and magenta solid lines represent the mean β value, standard deviation, and typical uncertainty for each bin, respectively. At the top right in each panel, we describe the corresponding magnitude bin and the p-value from the two-sample Kolmogorov-Smirnov (K-S) test. The null hypothesis of the K-S test is that the samples with (green) and without (blue) SEDS/*Spitzer* data are derived from the same distribution. As a result, the obtained p-value is significantly high ($0.50 - 0.70$), and the null hypothesis is not rejected at 5% significance level. Therefore, we can conclude that the lack of the information about 3.6μm and 4.5μm does not influence the selection for $z \sim 4$ star-forming galaxies very much.

From both the figure, the standard deviation is clearly larger than the typical uncertainty in the β value except for the two of the most faint magnitude bin. In these two bins, the typical

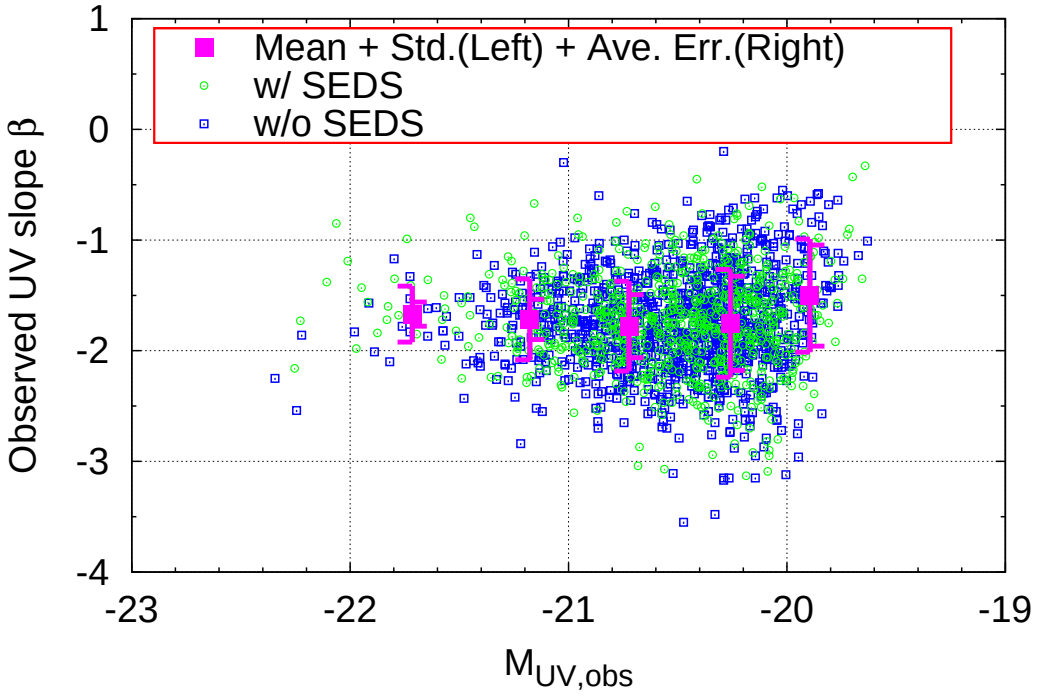

Figure 4.1: Observed UV slope β vs. UV absolute magnitude at rest-frame 1500Å (β-M_{UV} relation). The UV absolute magnitude is calculated by integrating the flux of the best-fit SED model template from rest-frame 1450Å to 1550Å. The green open circles represent the individual objects in the area of the SEDS and the blue open squares represent the individual objects out of the area. The magenta filled squares with the error bars represent the mean UV slope β value, standard deviation (left side), and mean error (right side) of the UV slope β for each magnitude bin, and they are summarized in Table 4.1.

uncertainty becomes as large as the standard deviation and we expect that the individual uncertainty in β for individual objects can explain the scatter of the observed β distribution. In Section 5.2, we will consider whether this large uncertainty can change our conclusions, or not. At least, in the magnitude range of $-22.0 \leq M_{\rm UV} < -20.5$, the observed β distribution is more scattered than the typical uncertainty, and the observed scatter represents the variation of the stellar population and dust extinction among the sample.

For the whole sample, the mean β value does not decrease with the UV magnitude M_{UV} but shows the weak correlation with the UV magnitude M_{UV}. In fact, by least-square linear fitting for the magenta points from $M_{UV} = -22.0$ to $M_{UV} = -20.0$, the slope of the fitted linear equation becomes -0.04 ± 0.02[1], which is nearly zero compared with the value in the previous works for the similar redshift, -0.13 ± 0.02 (Bouwens et al. 2014) and -0.10 ± 0.03

[1]For the fitting, we used *standard error of the mean* as the uncertainties for each the mean value. Therefore the uncertainties is calculated by (standard deviation)/(number of galaxy)= σ_β/N_{obj} described in Table 4.1

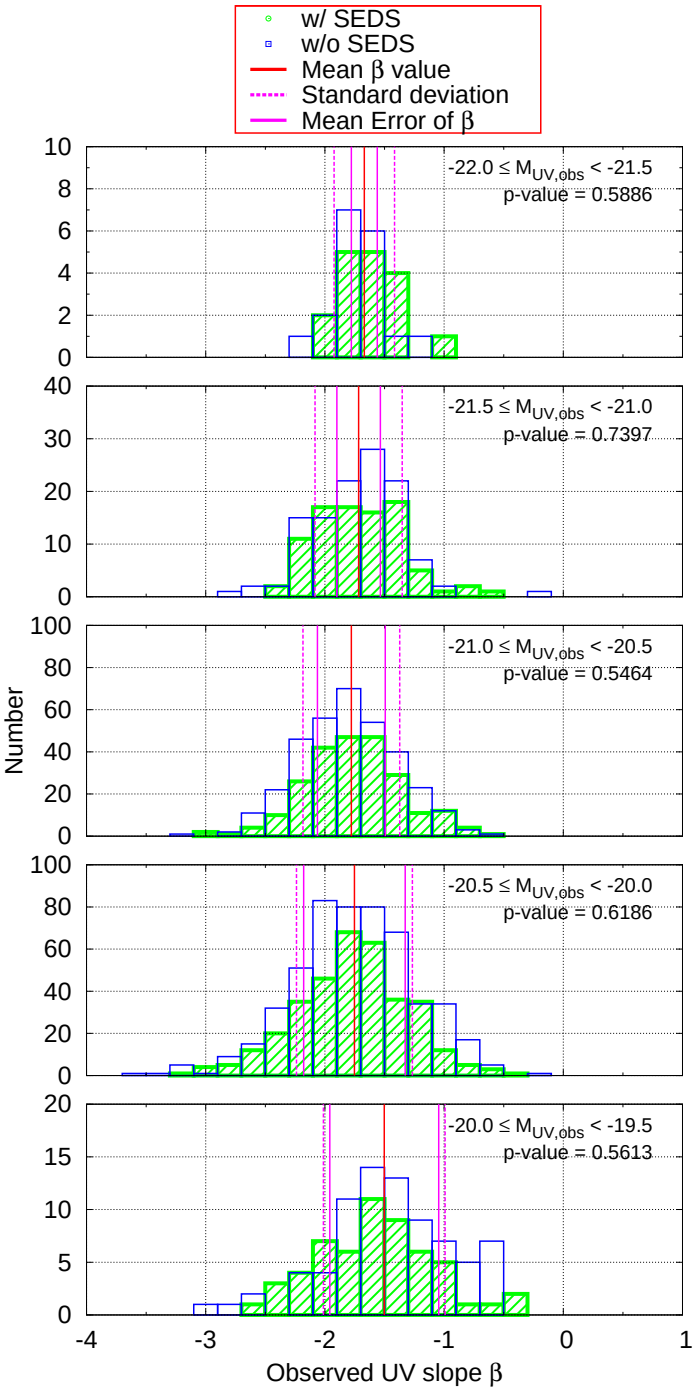

Figure 4.2: Number histogram of the β value for each magnitude bin. The green and blue histogram represent the samples with and without the SEDS/*Spitzer* data. At the top right in each panel, the magnitude bin and the p-value from the K-S test for the green and blue samples are shown.

Table 4.1: Summary of β_{obs}-$M_{UV,obs}$ Relation.

M_{UV} bin	$M_{\rm UV,mean}$	$\beta_{\rm mean}$	σ_β	Mean Err. of β	N_{obj}
-22.0 $\sim$ -21.5	-21.72	-1.67	0.25	0.11	35
-21.5 $\sim$ -21.0	-21.18	-1.72	0.37	0.18	207
-21.0 $\sim$ -20.5	-20.72	-1.78	0.41	0.28	577
-20.5 $\sim$ -20.0	-20.26	-1.75	0.49	0.43	863
-20.0 $\sim$ -19.5	-19.90	-1.50	0.51	0.46	134

(Kurczynski et al. 2014). In Figure 4.3, we show the comparison of our result to the results from $z \sim 4$ super luminous LBGs (Lee al. 2011) and $z \sim 4$ faint LBGs (Bouwens et al. 2014). Our results indicate that the luminous star-forming galaxies at $z_{phot} \sim 4$ which are selected from the ground-based wide field images show the weaker β-M_{UV} relation over the magnitude range from $M_{UV} = -22.0$ to $M_{UV} = -20.0$.

It seems that the distribution of the objects in Figure 4.1 is truncated and the shape of the distribution looks like a "triangle". This must be a result from either some physical constraint or some sample selection bias, or both. For example, a galaxy at $z = 4.5$ with the i'-band magnitude $i' = 26.0$ has $M_{UV} \lesssim -20.1$, and therefore the number of objects, which are selected from our selection criteria, would decrease in the region around $M_{UV} \sim -20$ and $\beta \sim -2.5$. By using only the three magenta points from the left in Figure 4.1, the slope of the relation indeed becomes -0.11 ± 0.02 which is quite similar to the value of the previous works. However, the number of the objects in the most left bin is much less than the other bins (see column 6 in Table 4.1) and consequently the slope is almost estimated from only the two data points. It is very risky to calculate the slope by only the two data points. In order to take account of our selection bias including the above, we need to assess the incompleteness of the observed β distribution, which is discussed in the next section.

4.2 *Incompleteness of Our Selection*

As it is evident from Figure 4.1, the observed β distribution is restricted in the "triangle" zone. It seems that there are three truncations, namely, (a) at the top left side, (b) at the bottom left side, and (c) at the bottom right side. In order to discuss the reason of those truncation and evaluate the validity of our results, we calculate the recovery fraction which is the number ratio of recovered objects to input objects by using Monte Carlo method.

At first, it is essential to make a uniform input distribution on β-M_{UV} space for the quantitative discussion. For this purpose we consider the 8×13=104 grids with $\Delta\beta = 0.5$ and $\Delta M_{UV} = 0.25$, and we generate 300 mock galaxy spectra whose β and M_{UV} values place in each the small grid (so the total spectra are 104×300=31,200). The mock spectra are constructed from the BC03 or SB99 model templates which are the same template sets as described in Section 3.2. All of the parameters such as SFH, dust attenuation value (Av), age,

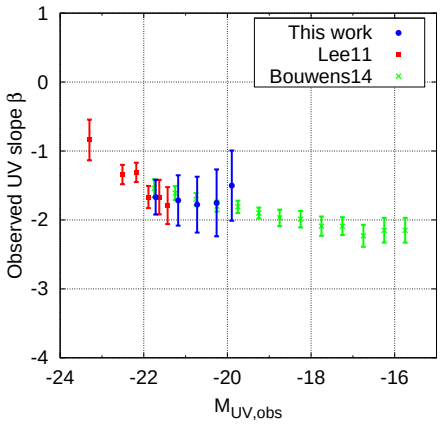

Figure 4.3: Comparison of this work with the previous studies at the similar redshift. The red squares and green crosses with the error bars show the results from Lee al. (2011) and Bouwens et al. (2014), respectively. Since the β values and its uncertainties for each magnitude bin are not explicitly described in Lee al. (2011), the plotted points with error bars are estimated by SY from the photometry described in their paper. Thus, the error bars show the uncertainty of power-law fitting. The error bars of Bouwens et al. (2014) show the sum of the random and systematic error described in their paper. The blue circles with the error bars show the result from our sample which is same as the magenta points in Figure 4.1. The error bars denote the *standard deviation* for each magnitude bin in order to show the scatter of our result.

metallicity (Z), and source redshift (z_s) are basically determined by random numbers. We note that the range of the dust attenuation value and source redshift for the mock galaxies are different from the range described in Section 3.2, and they are $0.0 \leq \mathrm{Av} \leq 1.5$ and $3.5 \leq z_s \leq 4.5$. If a resultant spectrum does not place in the designated small grid, we again shake a dice and generate a spectrum until the desired β and M_{UV} values.

Second, we calculate the apparent magnitude of the broad-band filters for each mock spectrum and we put the artificial galaxies on the real observed images from Subaru/B to UKIRT/K by using the IRAF mkobjects task. Since we check that the impact of *Spitzer*/3.6μm and 4.5μm is negligible for the β-M_{UV} relation in Section 4.1, we omit both the information in our simulation. The size and shape of the mock galaxies are also determined by random numbers so that the size distribution of our simulated objects reproduces the observed size distribution.

Finally these embedded mock galaxies are re-detected, re-measured, and re-compiled by the same manners described in Section 3.2. We count the number of final recovered objects for each small grid and calculate the number ratio of recovered to input objects. The final result includes the impact from the image quality, the magnitude criteria, the LBG selection, and the photo-z selection. Note that the prepared objects are restricted by only the rest-frame UV information and thus the rest-frame *optical* information such as Balmer break is purely determined by random numbers.

Figure 4.4 shows the final recovery fraction map by the color-corded area. The vertical

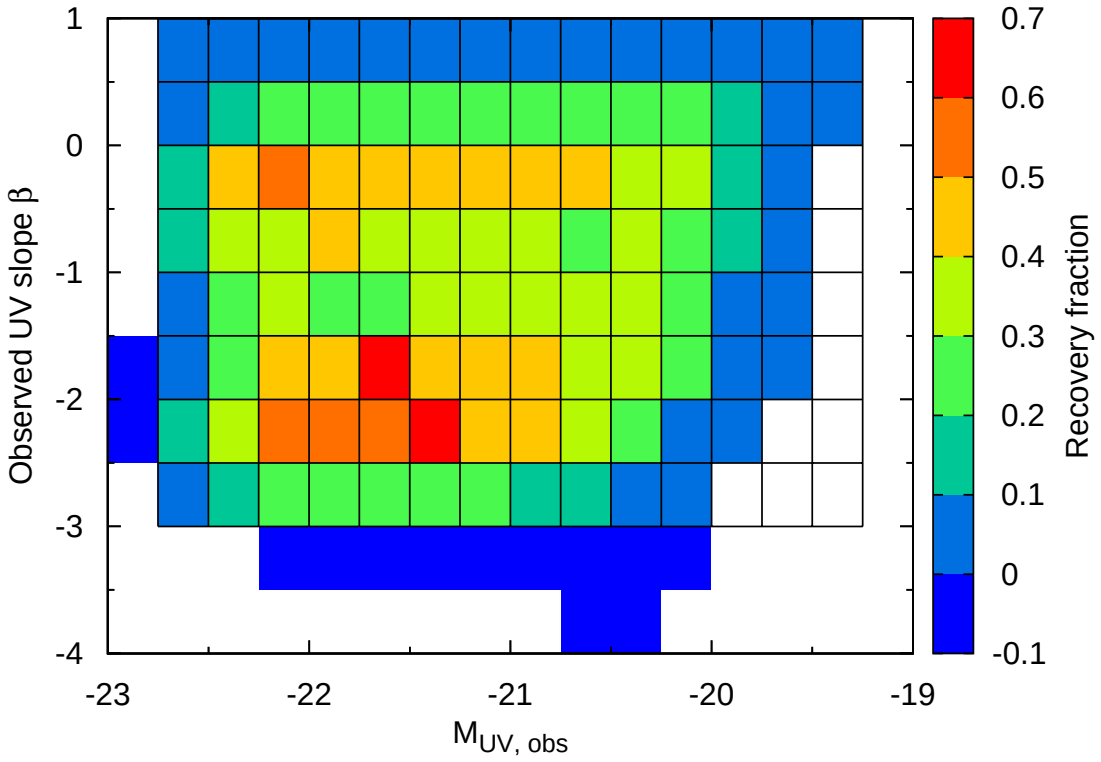

Figure 4.4: Recovery fraction which is the number ratio of recovered to input objects on β-M_{UV} space. The black grid lines represent the area where we prepare the input objects uniformly throughout the β-M_{UV} space and a total of 31,200 mock galaxies is distributed. The colored area represents the "detected" area where we can find recovered objects, and especially the blue colored area represents the area where there are no input objects but there are some recovered objects. The white colored area represents the "non-detection" area where we cannot find any recovered objects.

axis is the UV slope β and the horizontal axis is the absolute magnitude at rest-frame 1500Å. Although the UV absolute magnitude for input objects is given as total magnitude, the UV absolute magnitude for recovered objects is calculated from 2″-diameter aperture photometry. Therefore we convert the total magnitude of input objects to the 2″-aperture magnitude by the aperture correction: $M_{UV,aperture} = M_{UV,total} + 0.352$. The black lattice lines indicate each area where $\sim$ 300 mock galaxies (or input objects) are distributed except for both the faintest and brightest magnitude bins where $\sim$ 150 mock galaxies are distributed. The white area represents the "non-detection" area which means that there are no recovered objects. The colored area of the 'negative' recovery fraction (blue) represents the case that there are no input objects but there are some recovered objects. The galaxy with $\beta_{obs} < -3.0$ can be 'observed' even if there are no extremely blue galaxies for the input.

We find that the recovery fraction ranges between 0.0 and 0.7 over the input area except for the area around the truncation (c), namely, at the right bottom side. It means that

the truncation (c) is artificially caused by our sample selection. Actually our simulation indicates that the truncation (c) is attributed to the selection criteria of the updated-z' and J band detection. On the other hand, we find no evidence that the truncation (a) and (b) are artificial, and they must be caused by some other reasons. The figure also indicates that the recovery fraction shows a bimodal distribution which peaks at $\beta \sim -0.25$ and $\beta \sim -2.0$. We consider that the blue galaxies with $\beta \sim -2.0$ show significantly detectable Lyman Break and the red galaxies with $\beta \sim -0.25$ have clear Balmer Break if their red color is due to the aged stellar population. These prominent spectral features can be easily identified by the SED fitting procedure, and then the recovery fraction may become higher than the other β values. Indeed, the recovery fraction around $\beta \sim -2.0$ shows the highest value within the input area. It reflects our sample selection (Lyman Break) rather than the assumption about input objects since the Lyman Break technique prefers to select the blue galaxies. As mentioned above, the rest-frame optical information is determined by random numbers in our simulation, and hence the too many input galaxies, which have the prominent Balmer break, are probably generated to have the β value around ~ -0.25. If this is not the case, we can expect that the recovery fraction of $\beta \sim -0.25$ is not significantly different from that of $\beta \sim -0.75$ and $\beta \sim +0.25$. Therefore we infer that the bias due to the input mock galaxies has little impact on the incompleteness at $\beta \sim -0.25$.

In order to verify the above prediction for the bimodal distribution in Figure 4.4, we check number distributions of the input galaxies for each dust attenuation value and age. Figure 4.5 shows the number distributions of the input, and we can see a preferred dust attenuation value or age for a given β value in our simulation. The upper three panels represent the number distributions for the input galaxies with (1-a) Av < 0.5, (1-b) $0.5 \leq$ Av < 1.0, and (1-c) $1.0 \leq$ Av ≤ 1.5 from left to right. Also, the lower three panels represent the number distributions for the input galaxies with (2-a) Age $\leq$ 30Myr, (2-b) 30Myr $<$ Age $\leq$ 150Myr, and (2-c) Age $>$ 150Myr from left to right. The binning size in β and $M_{\rm UV}$ ($\Delta\beta$ and $\Delta M_{\rm UV}$) is same as Figure 4.4. The colored area denotes that the number of the input galaxies is larger than zero, and the white area means that the number of the input is equal to zero.

The upper three panels indicate that the redder (or bluer) galaxies tend to be produced from more (or less) dusty templates in the range of $-3.0 < \beta < 0.0$, and especially most of the red galaxies with $\beta \sim -0.25$ are produced from the templates with $1.0 \leq$ Av ≤ 1.5. At $\beta > 0.0$, however, the opposite trend is found, and the extremely red β galaxies ($\beta \sim 1.0$) can be produced from not only the more dusty templates but also the less dusty templates. From the lower three panels, we also find that the redder (or bluer) galaxies tend to be produced from older-age (or younger-age) templates in the entire range of the input β values. Indeed, the red galaxies with $\beta \sim -0.25$ are mainly produced from the templates with 30Myr $<$ Age $\leq$ 150Myr which have the relatively noticeable Balmer Break. The stronger Balmer Break and their red color result in the significant detection at the NIR band filters, and then such the galaxies are easily identified and have the higher recovery fraction through the Lyman Break and the photo-z selection. We conclude that the inhomogeneity of the recovery fraction seen in Figure 4.1 is mainly due to our sample selection criteria adopting the Lyman Break technique and photo-z estimation.

Comparing Figure 4.1 and Figure 4.4, interestingly, the area of the higher recovery fraction (> 0.5) corresponds to the area where there are little observed objects. In other words, the

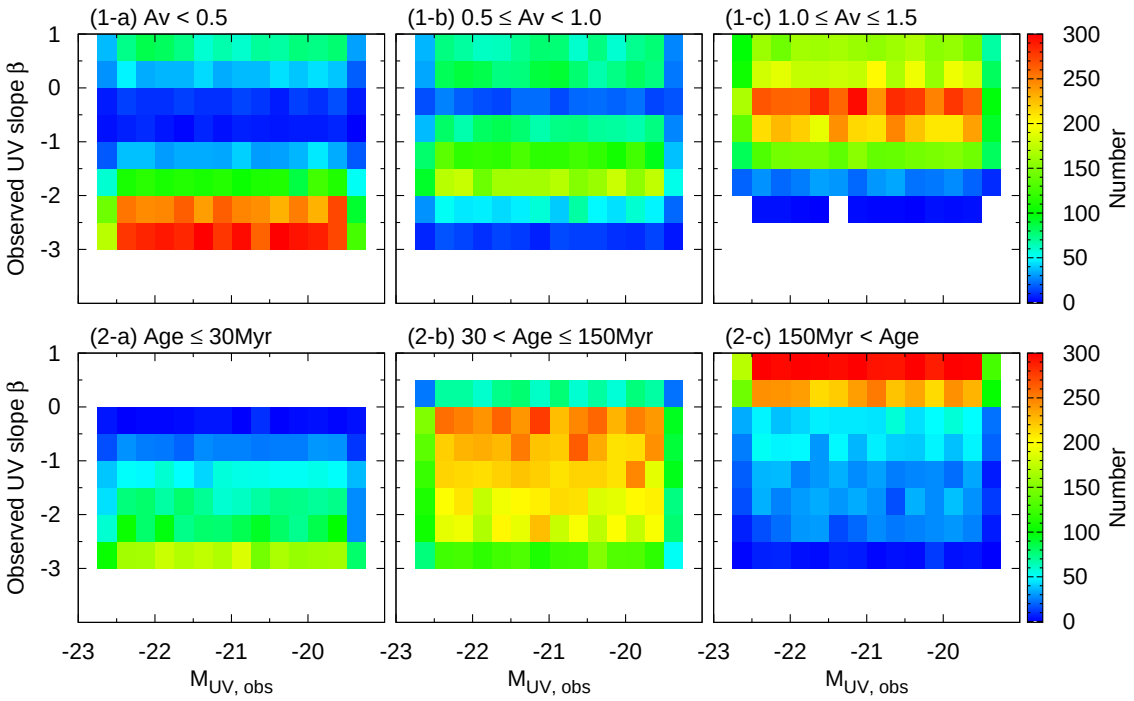

Figure 4.5: Number distribution of the input galaxies with a given dust attenuation value (upper three panels) or age value (lower three panels) on β-M_{UV} space. The white colored area represents $N_{input} = 0$, and the other colored are represents $N_{input} > 0$. The upper three panels labeled with (1-a), (1-b), and (1-c) show the number distributions for the input galaxies with Av $<$ 0.5, 0.5 $\leq$ Av $<$ 1.0, and 1.0 $\leq$ Av $\leq$ 1.5, from left to right respectively. Also, the lower three panels labeled with (2-a), (2-b), and (2-c) show the number distributions for the input galaxies with Age $\leq$ 30Myr, 30Myr $<$ Age $\leq$ 150Myr, and Age $>$ 150Myr, from left to right respectively. For instance, these panels show that input galaxies with $-3.0 < \beta < -2.5$ mainly consist of the templates with Av $<$ 0.5 and Age $\leq$ 30Myr.

truncation (a) and (b) cannot be reproduced by our sample selection and furthermore we can potentially find a more large number of LBGs at both area. We can explain this result as follows. The observed number of LBGs decreases toward the brighter UV magnitude and the average UV slope β value converges in $\beta \sim -1.7$. The decrease of LBGs along with the UV magnitude must be explained by the drop of UV Luminosity Function since the characteristic luminosity of $z \sim 4$ LBGs is $M_{\rm UV}{}^{*} = -21.14$ (Yoshida et al. 2006). However, it is *not clear* why the average UV slope β value converges in $\beta \sim -1.7$. Qualitatively the galaxies with $\beta \gtrsim -1.7$ should contain a large amount of dust and their UV magnitude becomes fainter due to the dust obscuration. Therefore the red and bright galaxies are a rare or almost impossible population, and it causes the truncation (a). On the other hand, the galaxies with $\beta \lesssim -1.7$ contain a less amount of dust and the galaxies can remain bright UV magnitude. As we cannot find the blue and bright galaxies from Figure 4.1, such the objects are indeed a rare population in the observational data.

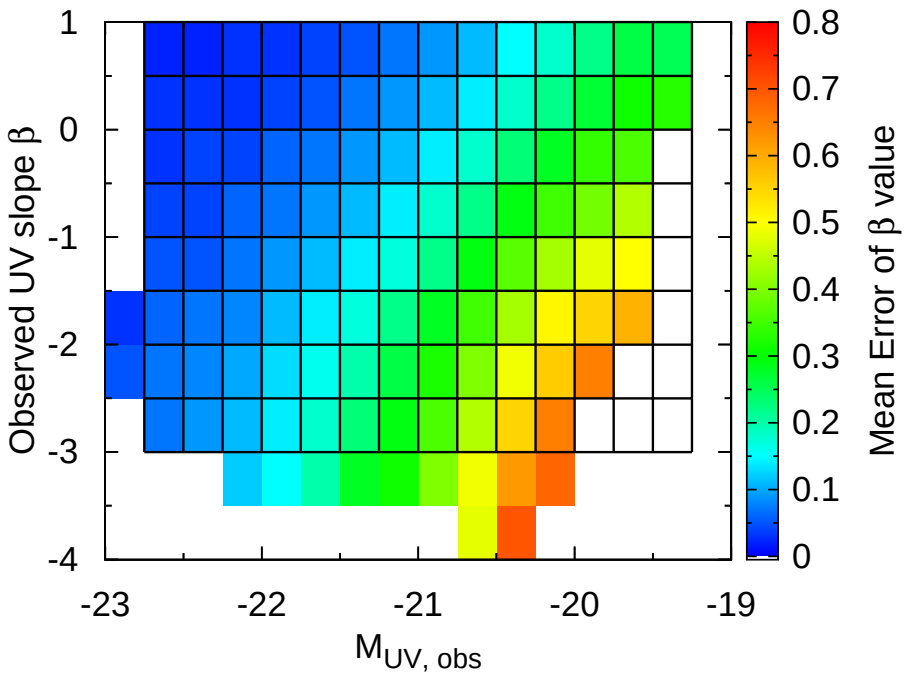

Figure 4.6: Same as Figure 4.4 but the color-coding denotes the average uncertainty of the β value for each grid.

Last of this section, it is useful to show a typical uncertainty of the β value for each grid on the β-$M_{\rm UV}$ space which is calculated for the recovered objects in our simulation. Figure 4.6 represents the distribution of the average uncertainty of the β value. This figure is same as Figure 4.4 but the color-coding represents the average uncertainty instead of the recovery fraction. The average uncertainty of the β value is as large as 0.7 at the right bottom region ($\beta \sim -2.5$ and $M_{\rm UV}\sim -20.0$) and as small as 0.1 at the left top region ($\beta \sim -0.5$ and $M_{\rm UV}\sim -22.0$). These values are consistent with the average β uncertainties calculated for the observed sample (Table 4.1). Clearly, objects around the right bottom region suffer from large photometric uncertainties, and the truncation (c) is caused by our selection criteria, especially the detection at the Subaru/updated-z' and/or UKIRT/J band filters. Moreover, for a given $M_{\rm UV}$ value, the β uncertainty decreases toward the redder β value. Therefore, if we calculate the average β value weighted by the individual β uncertainty for the observed sample in Section 4.1, the weighted-average β value will be biased toward the redder β value. The method for calculating the average β value described in Section 4.1 is suitable at least for our observed sample.

In summary, we conclude that the truncation (a) and (b) are NOT only caused by our sample selection and are most likely caused by some physical requirements, and the truncation (c) is clearly caused by our sample selection. In order to understand what make the blue and bright galaxies rare and to reveal the reason of the truncation (b), we discuss the underlying stellar population of LBGs for our sample in Chapter 5.

Chapter 5

DISCUSSION

In Section 4.2, we conclude that the observed distribution on β-$M_{\rm UV}$ space is caused by some physical reasons. Both observed β and $M_{\rm UV}$ value strongly depend on the dust attenuation value, and hence it is helpful to investigate the β-$M_{\rm UV}$ distribution before the dust reddening. We here consider the dust-corrected β (hereafter we call it *intrinsic* UV spectral slope, β_{int}, which is referred in Section 1.2) and the dust-corrected $M_{\rm UV}$ (hereafter we call it *intrinsic* UV absolute magnitude, $M_{{\rm UV},int}$). These intrinsic values are estimated assuming that the reasonable best-fit physical quantities are estimated from our SED fitting analysis in which the observed photometry covers the wavelength range between rest-frame $\sim$ 900 and $\sim$ 4400 Å (or $\sim$ 9000 Å in part) for $z \sim 4$ objects.

In this chapter, first, the validity of our SED fitting analysis is checked, and then we discuss the intrinsic UV spectral slope, β_{int}. We also investigate the β_{int} value in the case of fixed SFHs since there is a difficulty in inferring the SFHs in the SED fitting analysis. Moreover, we compare our results for $z \sim 4$ galaxies with the previous results for $z \sim 2$ and 0 galaxies. Finally, these results depends on the assumed dust attenuation law, and thus we check the difference when using the SMC dust extinction curve.

5.1 *Validity of Our SED Fitting Analysis*

Before going to the discussion for β_{int} and $M_{{\rm UV}int}$, we show three examples in our sample in Figures 5.1, 5.2, and 5.3 in order to check the validity of our SED fitting analysis. The first and second figures are the intrinsically blue LBGs observed without *Spitzer* ($\beta_{obs} = -1.17$ and $M_{{\rm UV},obs} = -21.79$) and with *Spitzer* ($\beta_{obs} = -0.74$ and $M_{{\rm UV},obs} = -20.73$), and the third figure is the apparently blue LBG ($\beta_{obs} = -2.16$ and $M_{{\rm UV},obs} = -22.25$). In the top of each figure, we show the stamps of the imaging data from SXDS/B to UDS/K. The green "plus" mark at the center of the images represents the detected position, and the green two "bars" are placed at 1″ from the detected position with 1″ length. In the bottom left panel, we show the best-fit SED and observed photometry. For comparison, in Figures 5.1 and 5.2 we also show the model template of the old and less dusty population (SB99, Burst, Age=150Myr, Av=0.1, and $Z = 0.2Z_{\odot}$) whose magnitude is normalized to be same as the observed magnitude at i'-band. In the bottom right panel, we show the χ^2 map of our SED

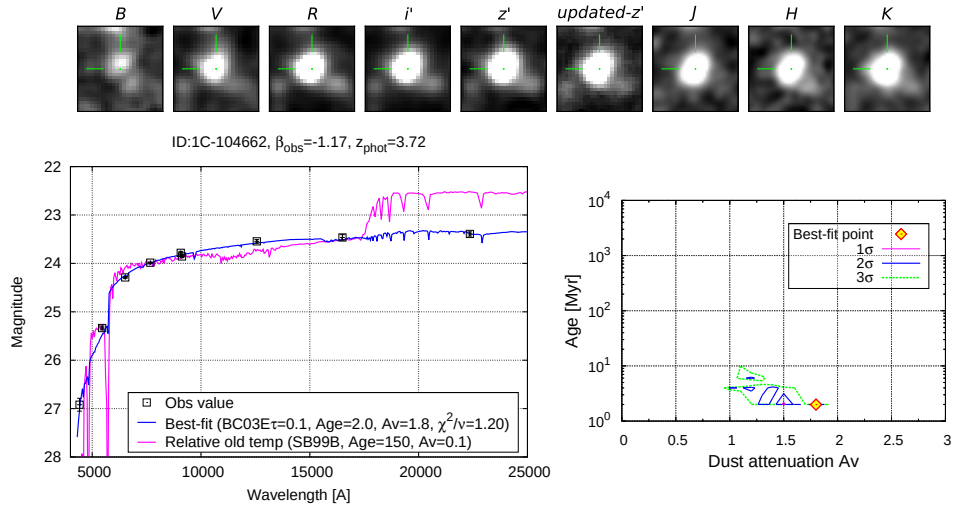

Figure 5.1: Example object for the intrinsically intense star-forming galaxy which has $\beta_{obs} = -1.17$, $M_{\mathrm{UV},obs} = -21.79$, and $z_{phot} = 3.72$. Top: The images show the $5'' \times 5''$ stamps from SXDS/B (left) to UDS/K (right). The green plus point at the center of each stamp represents the position of the detection in each filter, and the green two straight lines in each stamp have $1''$ length and are drawn at $1''$ apart from the center. Bottom left: The black open squares with the error bars show the measured aperture photometry with the 1σ error from SXDS/B (left) to UDS/K (right). The blue solid line shows the best-fit SED model template which is constructed from the parameters of the BC03 exponentially decline SFH with $\tau = 0.1$ Gyr, age of 2.0 Myr, Av = 1.8, and $Z = 0.2Z_{\odot}$. For comparison, we also show the model template of the relatively old (= 150 Myr) and less dusty (Av= 0.1) stellar population normalized by the i'-band magnitude. Bottom right: We show the χ^2 map on Age-Dust parameter space. The best-fit point is shown by the yellow filled diamond and the 1σ, 2σ, and 3σ confidence levels are shown by the magenta, blue, and green encircled lines, respectively.

fitting analysis on two-dimensional space. The vertical axis represents the galaxy age and the horizontal axis represents the dust attenuation value. The best-fit point is described by the yellow diamond and the area of the 1σ, 2σ, and 3σ confidence levels, estimated from the best-fit χ^2 value, are drawn by the magenta, blue, and green lines, respectively. The three examples we show here demonstrate that our SED fitting procedure performs well thanks to the deep imaging data of UDS-UKIDSS/UKIRT *HK*-band which covers the wavelength of Balmer break for LBGs at $z \sim 4$.

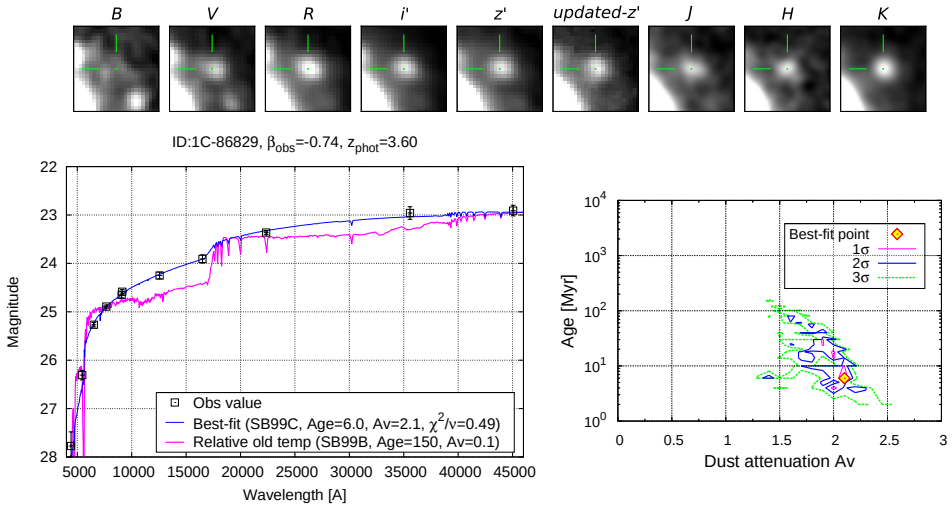

Figure 5.2: Example object for the intrinsically intense star-forming galaxy observed with *Spitzer*. The object has $\beta_{obs} = -0.74$, $M_{\mathrm{UV},obs} = -20.73$, and $z_{phot} = 3.60$. Top and Bottom right: Same as Figure 5.1. Bottom left: Same as Figure 5.1 but the best-fit parameters are the SB99 continuous constant SFH, age of 6.0 Myr, Av = 2.1, and $Z = 0.2Z_{\odot}$

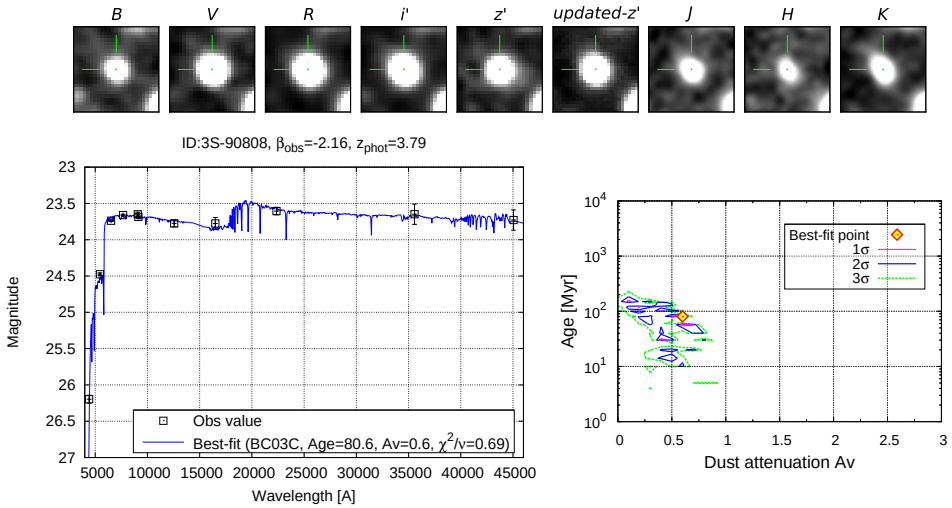

Figure 5.3: Example object for the apparently active star-forming galaxy which has $\beta_{obs} = -2.16$, $M_{\mathrm{UV},obs} = -22.25$, and $z_{phot} = 3.79$. Top and Bottom right: Same as Figure 5.1. Bottom left: Same as Figure 5.1 but we only show the best-fit model template which is constructed from the parameters of the BC03 continuous constant SFH, age of 80.6 Myr, Av = 0.6, and $Z = 0.2Z_{\odot}$

5.2 *Intrinsic UV Spectral Slope* β

We calculate the intrinsic UV spectral slope β by Eq.3.1 for the intrinsic magnitude of i', updated-z', and J band filters. For estimating the intrinsic magnitude, we convolve the intrinsic SED, which is reproduced with the best-fit physical quantities without any dust extinction, with the three broad-band filters. We note that the intrinsic UV slope depends on the prepared model templates in the SED fitting (i.e., SFH, age, and metallicity) and has discrete values in our discussion.

Figure 5.4 shows the step-by-step conversion from observed to intrinsic value for β and $M_{\rm UV}$. The top left panel shows the *observed* β as a function of the *observed* $M_{\rm UV}$ (β_{obs}-$M_{{\rm UV},obs}$ relation, same as Figure 4.1). The top right panel shows the *observed* β as a function of the *intrinsic* $M_{\rm UV}$ (β_{obs}-$M_{{\rm UV},int}$ relation). The bottom right panel shows the *intrinsic* β as a function of the *intrinsic* $M_{\rm UV}$ (β_{int}-$M_{{\rm UV},int}$ relation). The blue, green, and red points represent individual objects with the best-fit dust attenuation value of Av < 0.5, $0.5 \leq$ Av < 1.0, and $1.0 \leq$ Av. In the top left panel we confirm that the objects with the higher dust attenuation value are distributed at the upper area where the β value becomes redder. This trend is natural and is not inconsistent with the previous studies reported as the relation between the β and dust attenuation value (IRX-β relation; e.g., Calzetti et al. 1994; Meurer et al. 1999; Takeuchi et al. 2012). In the top right panel the distribution of objects becomes tighter than the distribution in the top left panel and the two quantities seem more correlated. This reflects the correlation between total (or extinction-corrected) luminosity and dust attenuation (Reddy et al. 2006). The distribution of the objects with similar β_{obs} values occupies the similar area in the bottom right panel, i.e., the galaxies which show similar observed β values have similar intrinsic β and intrinsic UV absolute magnitude values.

In the bottom right panel of Figure 5.4, surprisingly, the intrinsic β value slightly increases with the intrinsic $M_{\rm UV}$ value and the trend is opposite of those of the β_{obs}-$M_{{\rm UV},obs}$ and β_{obs}-$M_{{\rm UV},int}$ relation. In other words, the objects which are redder in the observed β tend to be bluer in the intrinsic β and brighter in the intrinsic $M_{\rm UV}$. Although there is a degeneracy between the galaxy age and dust attenuation value, the uncertainty (e.g., shown in Figures 5.1, 5.2, and 5.3) is not significantly large and does not change the whole shape of the β_{int}-$M_{{\rm UV},int}$ distribution. Moreover, if a object actually has a older-age and less-dusty stellar population than the best-fit value, the object should have a relatively red β_{int} and faint $M_{{\rm UV},int}$ value. In that case the object moves along the suggested β_{int}-$M_{{\rm UV},int}$ relation. Therefore this β_{int}-$M_{{\rm UV},int}$ trend is substantial and can be interpreted as follows; the more intense ongoing star-forming galaxies, whose *intrinsic* β and $M_{\rm UV}$ value are bluer and brighter, generate and/or contain a large amount of dust, and the *observed* β and $M_{\rm UV}$ value result in a redder and fainter value due to the dust attenuation. Then, the nearly constant β_{obs}-$M_{{\rm UV},obs}$ distribution is formed by the galaxies which have a blue β_{int} and bright $M_{{\rm UV},int}$ value because they are distributed at the area of a red β_{obs} and faint $M_{{\rm UV},obs}$ value.

According to our SED fitting analysis, a young-age stellar population is responsible for the bluest β_{int} value. In other words, there are some young-age galaxies with the bluest β_{int} and brightest $M_{{\rm UV},int}$ value, but there are no intermediate- and old-age galaxies with the bluest β_{int} and brightest $M_{{\rm UV},int}$ value. This is not surprising because the intrinsic UV luminosity

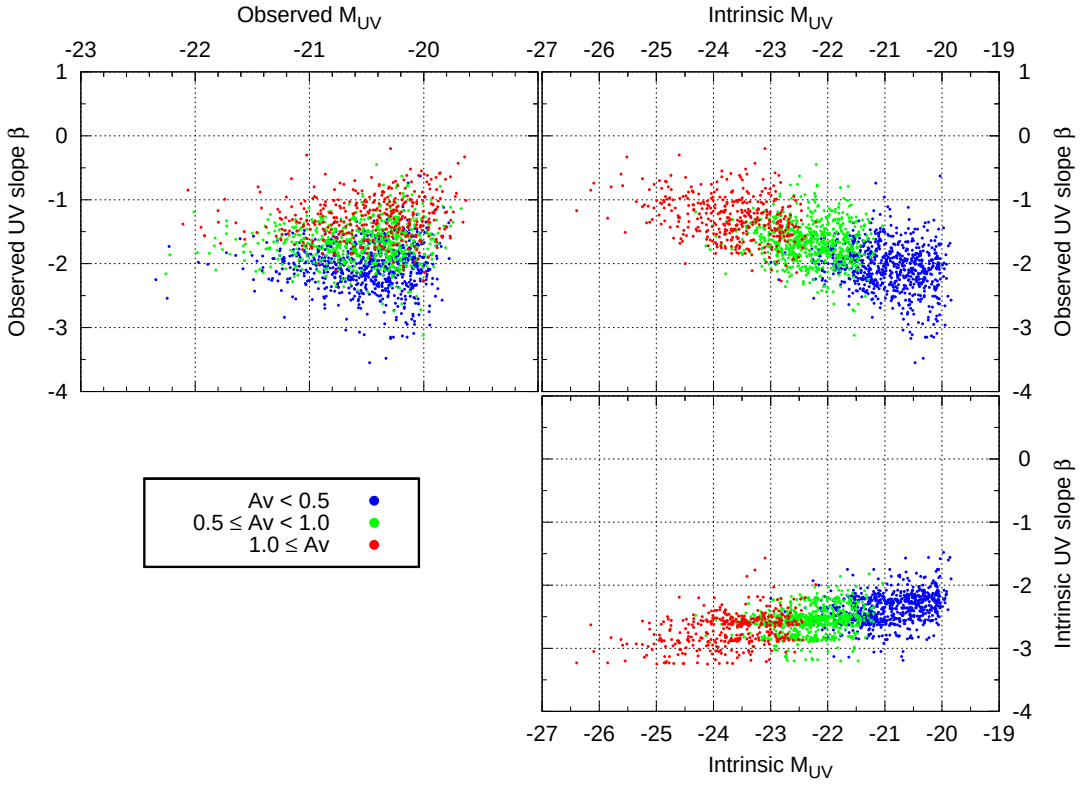

Figure 5.4: Comparison of the distribution for observed UV slope β vs. observed absolute magnitude at rest-frame 1500Å (top left panel, same as Figure 4.1), observed UV slope β vs. *intrinsic* absolute magnitude (top right panel), and *intrinsic* UV slope β vs. *intrinsic* absolute magnitude (bottom right panel). The best-fit dust attenuation values for the individual objects are expressed by the blue, green, and red color-coding, which indicate Av < 0.5, $0.5 \leq$ Av < 1.0, and $1.0 \leq$ Av, respectively.

is expected to be sensitive to the age of the stellar population. For example, in the case of the instantaneous burst SFH, the UV luminosity is dominated by the stars at "turn-off point" on Hertzsprung-Russell Diagram which is a age indicator of the stellar population. In the case of the continuous constant SFH, it is hard to sustain a very high star formation rate with the intermediate and long time duration due to gas depletion. We, however, emphasize that the bluest β_{int} value is explained by the young-age stellar population in our analysis, but other parameters such as metallicity and/or IMF can explain the reason of the bluest β_{int} value. Indeed some literatures argue that dusty star-forming galaxies have a "top-heavy" IMF although the discussion still continues (e.g., Baugh et al. 2005; Tacconi et al. 2008; Bastian et al. 2010). Under the top-heavy IMF environment, hot and massive stars can be formed more and more, and the bluer β_{int} value is easily produced. Otherwise, among the galaxies with the bluest β_{int} value, there may be a post-primordial starburst which is dominated by extremely metal-poor (or PopⅢ) stars.

In Figure 5.5, we reproduce Figure 5.4 but the color-coding represents the $M_{\mathrm{UV},obs}$ value.

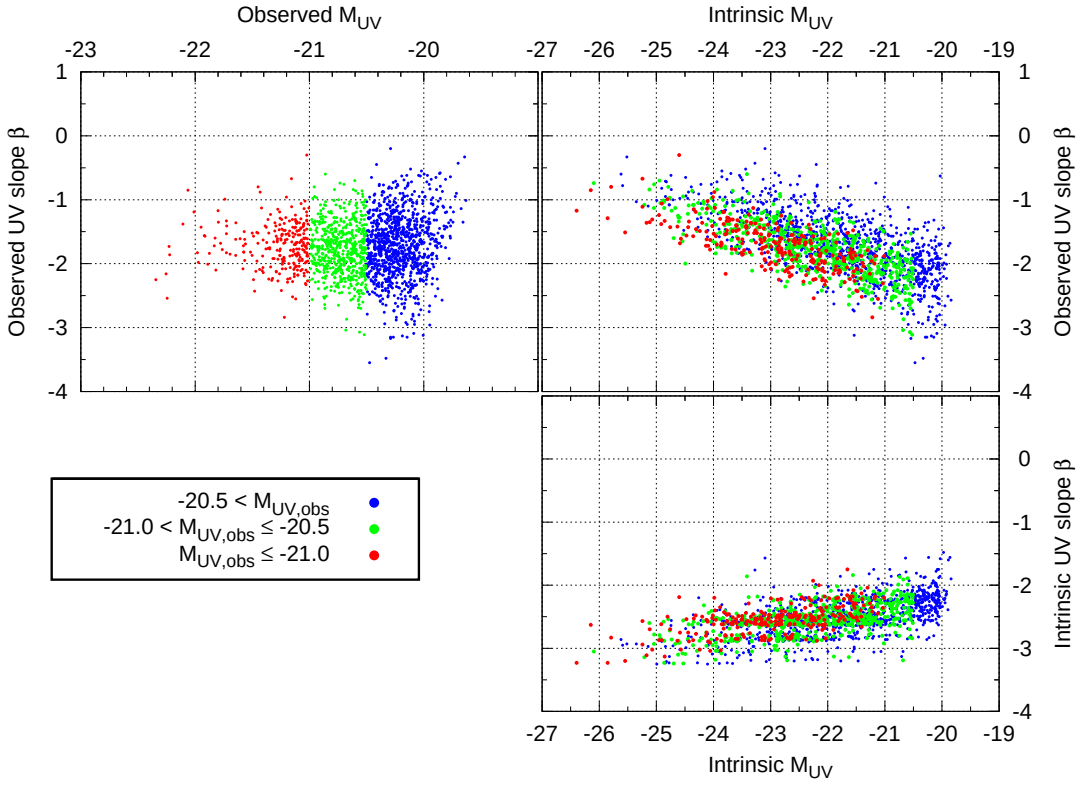

Figure 5.5: Same as Figure 5.4 but the blue, green, and red points represent the individual objects with $M_{\mathrm{UV},obs} > -20.5$, $-20.5 \geq M_{\mathrm{UV},obs} > -21.0$, and $-21.0 > M_{\mathrm{UV},obs}$, respectively.

The blue, green, and red points indicate $M_{\mathrm{UV},obs} > -20.5$, $-20.5 \geq M_{\mathrm{UV},obs} > -21.0$, and $-21.0 > M_{\mathrm{UV},obs}$, respectively. From Figure 4.1, Figure 4.2, and Table 4.1, it is possible that the β_{int}-$M_{\mathrm{UV},int}$ relation is artificially formed since the typical uncertainty in the β_{obs} value is as large as the standard deviation of the β_{obs} distribution in the two of the most faint magnitude bin. However this figure specifically shows that the trend of β_{int}-$M_{\mathrm{UV},int}$ relation is independent on the $M_{\mathrm{UV},obs}$ value. It means that the β_{int} and $M_{\mathrm{UV},int}$ value are determined by taking account of the whole shape of spectrum and our result is not significantly affected by the uncertainty of observed UV spectral slope β.

In order to check the above interpretation, we plot the Star Formation Rate (SFR) of the individual objects as a function of their stellar mass in Figure 5.6. For the estimation of SFR, we convolve the best-fit template with the *GALEX*/FUV filter response curve and use the calibration for FUV luminosity (Hao et al. 2011; Kennicutt & Evans 2012). For estimating the stellar mass, we multiply the best-fit normalization factor to the output from the BC03 model template. All the left three panels in Figure 5.6 show the observed (NOT dust-corrected) SFR as a function of the stellar mass, but represent the various sub-samples in each panel. In the top panel, the blue, green, and red points represent the individual objects with the dust attenuation value of Av < 0.5, $0.5 \leq$ Av < 1.0, and $1.0 \leq$ Av, respectively. In

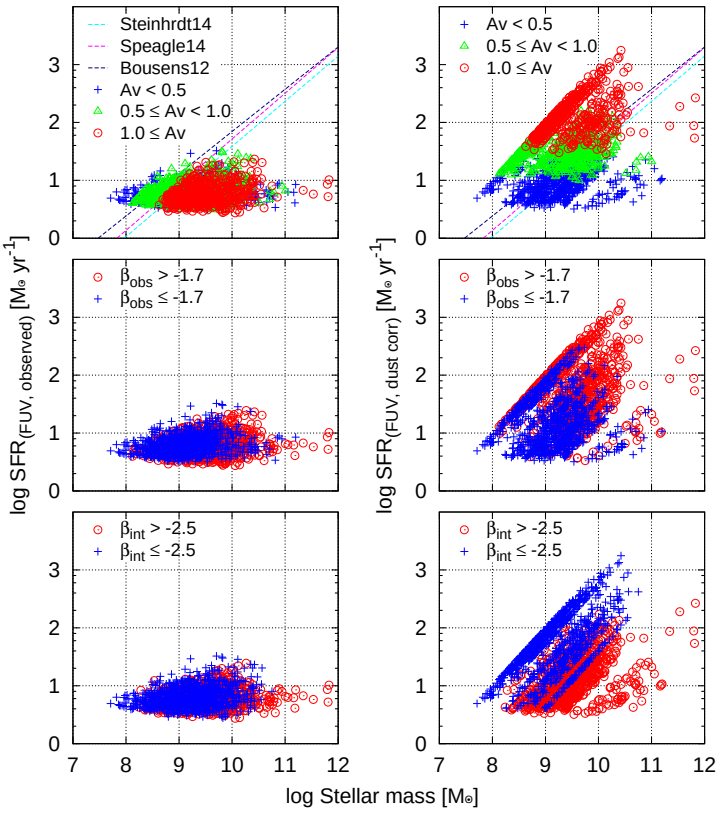

Figure 5.6: SFR vs. stellar mass estimated from the BC03 model templates. The SFR is estimated from the luminosity at the *GALEX*/FUV filter by using the Hao et al. (2011) calibration. The stellar mass is calculated multiplying the normalization factor to the output of the BC03 model. Left: All of the three panels show the SFR estimated from the observed (NOT dust-corrected) luminosity as a function of the stellar mass. From top to bottom, the color-coding represents the best-fit dust attenuation value, the observed UV slope, and the intrinsic UV slope, respectively. In the top panel, we also draw the SFR − M_* relation at $z \sim 4$ (Bouwens et al. 2012; Speagle et al. 2014; Steinhardt et al. 2014). Right: Same as the left panels but the SFR is the dust-corrected value.

the middle panel, the blue and red points represent the individual objects with the observed UV slope value of $\beta_{obs} \leq -1.7$ and $\beta_{obs} > -1.7$, respectively. In the bottom panel, the blue and red points represent the individual objects with the intrinsic UV slope value of $\beta_{int} \leq -2.5$ and $\beta_{obs} > -2.5$, respectively. All the right three panels in Figure 5.6 show the intrinsic (dust-corrected) SFR as a function of the stellar mass and the color-coding is same as the left panels for each. In both top panels, we also show the SFR − M_* relation called as "main-sequence" of star forming galaxies at similar redshift (Bouwens et al. 2012; Speagle et al. 2014; Steinhardt et al. 2014).

This figure shows that the most intense star-forming galaxies have Av ≥ 1.0, $\beta_{obs} > -1.7$, and $\beta_{int} \leq -2.5$ in our sample. According to the previous study for the star-forming galaxies

at $z \sim 2$ observed with *Spitzer*/MIPS (Reddy et al. 2010), the most actively star-forming galaxies indeed show the redder β_{obs} and larger dust attenuation. Our result are consistent with this work and it means that the most intense star-forming galaxies at $z \sim 4$ have similar property to the galaxies at $z \sim 2$.

5.3 β_{int}-$M_{\mathrm{UV},int}$ *Relation*

In our SED fitting analysis we picked up the model template which had the most small χ^2 value, and therefore the above results contain the extra degeneracy from SFH. In order to separate the SFH degeneracy, we repeat the SED fitting analysis for each fixed SFH template. The results of the β_{int}-$M_{\mathrm{UV},int}$ relation are shown in Figure 5.7 and the corresponding SFHs are labeled on the top of each panel. The first and second rows show the results of the BC03 model template and the third row shows the results of the SB99 model template. In these panels the blue, green, and red points represent the individual objects with the best-fit value of Age $\leq$ 30 Myr, 30 Myr $<$ Age $\leq$ 150 Myr, and 150 Myr $\leq$ Age. Since the SB99 model does not include the template of Age $>$ 150 Myr, there are no red points in the panels at the third row. In the most bottom right panel, we also show the β_{obs}-$M_{\mathrm{UV},obs}$ result which is the same figure in the top left panel of Figure 5.4 but the color-coding represents the best-fit age value.

We find that the global trend of the β_{int}-$M_{\mathrm{UV},int}$ relation does not significantly change among each fixed SFH and all of them are similar to the bottom right panel of Figure 5.4. It means that the β_{int}-$M_{\mathrm{UV},int}$ relation is independent of the assumed SFH and this result supports the interpretation described in Section 5.2. Summarizing the above discussion, the star-forming galaxies have the positive β_{int}-$M_{\mathrm{UV},int}$ relation and the effect of dust attenuation significantly distorts the relation. Finally the β-M_{UV} relation results in the negative β_{obs}-$M_{\mathrm{UV},obs}$ relation reported by the previous works. However, focusing only on the bright magnitude range ($-22 \lesssim M_{\mathrm{UV},obs} \lesssim -20$), the β_{obs} value looks like constant to the $M_{\mathrm{UV},obs}$ value (constant β_{obs}-$M_{\mathrm{UV},obs}$ relation) due to the existence of dusty active star-forming population.

Finally we consider whether the above β_{int}-$M_{\mathrm{UV},int}$ trend continues in the fainter magnitude range, or not. According to Bouwens et al. (2014), the β_{obs} value becomes bluer when the $M_{\mathrm{UV},obs}$ value becomes fainter, but the slope of the β_{obs}-$M_{\mathrm{UV},obs}$ relation becomes flatter in $M_{\mathrm{UV},obs} \gtrsim -19.0$. In order to establish both the observed and intrinsic β-M_{UV} relation without contradiction, it is expected that the β_{int} value becomes redder and converges to the certain β value toward the fainter magnitude range. When we extrapolate the β_{int}-$M_{\mathrm{UV},int}$ relation faintward below our sample magnitude limit, we will find the intersection point of the observed and intrinsic β-M_{UV} relation. Since the dust attenuation value becomes smaller toward the fainter magnitude range along the β_{int}-$M_{\mathrm{UV},int}$ relation (Section 5.2), the intersection point (or convergence point) will represent the position of the appearance of nearly dust-free population. Our β_{int}-$M_{\mathrm{UV},int}$ relation shows $\beta_{int} = 0.45 + 0.13 M_{UV,int}$ by only using the sample of Av < 0.5, and the β_{obs}-$M_{\mathrm{UV},obs}$ relation from Bouwens et al. (2014) shows $\beta_{obs} = -4.39 - 0.13 M_{UV,obs}$ in $M_{\mathrm{UV},obs} \leq -18.8$. As a result, both relations intersect at $M_{\mathrm{UV}} = -18.6$ and $\beta = -1.97$ and its point corresponds to the break point of β_{obs}-$M_{\mathrm{UV},obs}$

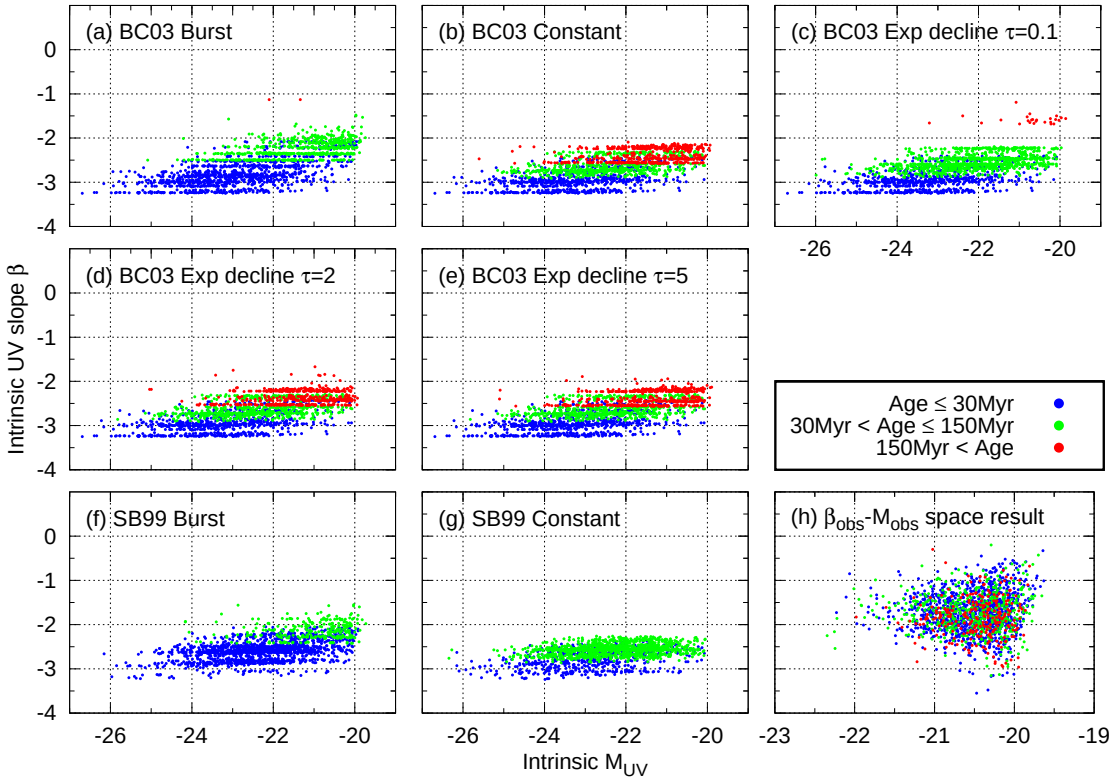

Figure 5.7: Intrinsic UV slope β distribution for each fixed SFH model. The top three panels and middle two panels show the results of the BC03 model templates and bottom left two panels show the results of the SB99 model templates. The SFHs used for the SED fitting analysis are labeled in each panel: (a) instantaneous burst, (b) continuous constant, (c) exponentially decline with $\tau = 0.1$ Gyr, (d) exponentially decline with $\tau = 2$ Gyr, (e) exponentially decline with $\tau = 5$ Gyr, (f) instantaneous burst, and (g) continuous constant from top to bottom panels. For comparison, the bottom right panel shows the observed UV slope β vs. the observed absolute magnitude at rest-frame 1500Å (same as Figure 4.1). In all of the panels, the best-fit age values for the individual objects are expressed by blue, green, and red color-coding, which indicate Age $\leq$ 30 Myr, 30 Myr $<$ Age $\leq$ 150 Myr, and 150 Myr $\leq$ Age, respectively.

relation at $M_{\rm UV} = -18.8$ and $\beta = -1.95$ reported by Bouwens et al. (2014). The above discussion is shown in Figure 5.8. Therefore the transition of the β_{obs}-$M_{{\rm UV},obs}$ relation around $M_{\rm UV} \sim -18.8$ indicates that we really see the almost dust-free population in $M_{\rm UV} < -18.8$, and the apparently bluest star-forming galaxies have $\beta \sim -2.0$.

5.4 *Color-Color Diagram*

In Sections 5.2 and 5.3, we show that the β_{int}-$M_{{\rm UV},int}$ relation does not significantly depend on the $M_{{\rm UV},obs}$ value (or photometric error) and the assumed SFHs (Figures 5.7). On

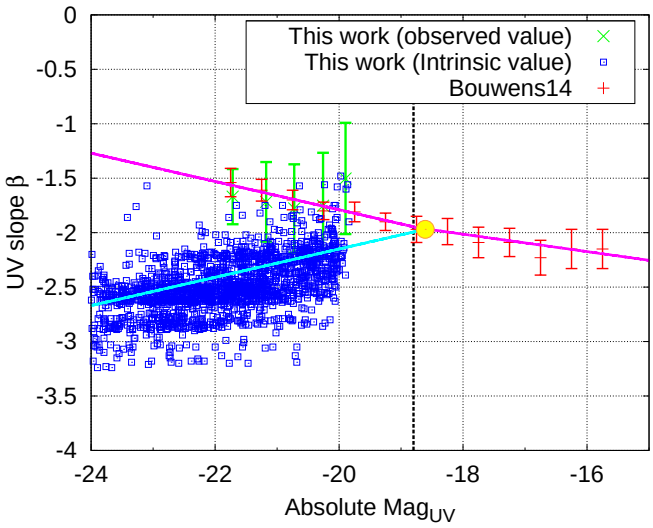

Figure 5.8: The β-$M_{\rm UV}$ relation. The blue open squares represent the individual galaxies in our sample referring to the intrinsic β and $M_{\rm UV}$ value (same as Figure 5.4 bottom right). The cyan solid line denote the best-fit linear function for our sample of Av < 0.5. For comparison, the green cross with error bars represent the mean observed β value for each observed magnitude bin described in Chapter 4. The red points with error bars and magenta solid line denote the observed β-$M_{\rm UV}$ relation from Bouwens et al. (2014). The vertical black dotted line shows the transition magnitude suggested by Bouwens et al. ($M_{{\rm UV},obs} = -18.8$). The large yellow filled circle represents the intersection point of our intrinsic β-$M_{\rm UV}$ relation and the observed β-$M_{\rm UV}$ relation of Bouwens et al..

the basis of the β_{int}-$M_{{\rm UV},int}$ relation, we also suggest that a part of star-forming galaxies at $z \sim 4$ in our sample is classified as DSFGs. This result is derived from the SED fitting analysis in which the photometric error of all the broad-band filters is simultaneously taken into consideration. However, the photometric error typically becomes larger at longer wavelength owing to the survey depth of imaging data (Table 2.1). Consequently, a weight of the photometry in the SED fitting analysis becomes smaller at longer wavelength, and it is possible that the photometry of *zJHK*-band filters does not have a considerable constraint on the best-fit SED. In particular, the wavelength range of the *zJHK*-band filters covers the Balmer Break of $z \sim 4$ galaxies, and the constraint from the *zJHK*-band photometry is critical for finding the DSFGs. In this section, we therefore focus on the photometry of *zJHK*-band filters, and discuss the existence of DSFGs by using a simple color-color technique which is a similar method with the Lyman Break technique.

For predicting the position of DSFGs at $z \sim 4$ on the color-color diagram, we calculate a color of photometries for seven model templates which are constructed by using the BC03 population synthesis model. For simplicity, we fix the dust attenuation value, age, metallicity, and SFH for each the model template, and consider the photometry of Subaru/updated-z', UKIRT/J, H, and K. The redshift ranges between 0.0 and 6.0 with an interval of $\Delta z = 0.1$. The seven model templates consist of two DSFG templates, two dust-free star-forming galaxy

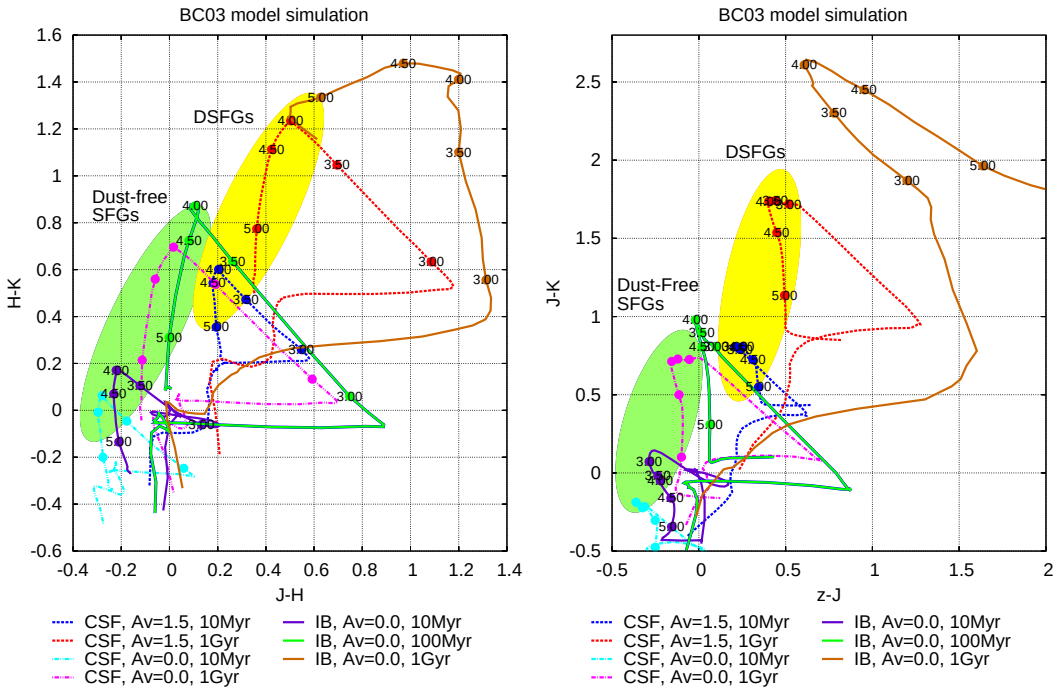

Figure 5.9: Color-Color diagram for several templates. The left panel represents $J-H$ vs. $H-K$ diagram (JHK diagram), and the right panel represents $z-J$ vs. $J-K$ diagram (zJK diagram). The seven colored lines are calculated from redshift 0.0 to 6.0 by using the BC03 model templates. The blue and red dashed lines denote the DSFG templates which are Continuous Constant SFH, Av = 1.5, $Z = 0.2Z_{\odot}$, and Age = 10Myr (blue) and Age = 1Gyr (red), respectively. The cyan and magenta dot-dashed lines denote the dust-free star-forming galaxy templates which are Continuous Constant SFH, Av = 0.0, $Z = 0.2Z_{\odot}$, and Age = 10Myr (cyan) and Age = 1Gyr (magenta), respectively. The purple, green, and orange solid lines denote the dust-free quiescent galaxy templates which are Instantaneous Burst SFH, Av = 0.0, $Z = 0.2Z_{\odot}$, and Age = 10Myr (purple), Age = 10Myr (green), and Age = 1Gyr (orange), respectively. The filled circles plotted on each the lines represent the redshift from 3.0 to 5.0 with a interval of $\Delta z = 0.5$, and further the redshift values are labeled on the circles of the DSFGs and quiescent templates.

templates, and three dust-free quiescent (non star-forming) galaxy templates. Since the Balmer Break of $z \sim 4$ galaxies is ~ 18000Å and enters the wavelength coverage of H-band, we consider two kinds of the color-color diagram: $J-H$ vs. $H-K$ diagram (JHK diagram), and $z-J$ vs. $J-K$ diagram (zJK diagram). The color combinations we adopt in both the diagram are intended to capture the hardness of light shortward of the Balmer Break and the height of the Balmer Break.

Figure 5.9 shows these model calculations; The left panel shows the result of the JHK diagram and the right panel shows the result of the zJK diagram. The blue and red dashed lines denote the DSFG templates which are Continuous Constant SFH, Av = 1.5, $Z = 0.2Z_{\odot}$, and Age = 10Myr (blue) and Age = 1Gyr (red), respectively. The cyan and magenta dot-dashed lines denote the dust-free star-forming galaxy templates which are Continuous

Constant SFH, Av = 0.0, $Z = 0.2Z_{\odot}$, and Age = 10Myr (cyan) and Age = 1Gyr (magenta), respectively. The purple, green, and orange solid lines denote the dust-free quiescent galaxy templates which are Instantaneous Burst SFH, Av = 0.0, $Z = 0.2Z_{\odot}$, and Age = 10Myr (purple), Age = 10Myr (green), and Age = 1Gyr (orange), respectively. The filled circles plotted on each the lines represent the redshift from 3.0 to 5.0 with a interval of $\Delta z = 0.5$, and further the redshift values are labeled on the circles of the DSFGs and quiescent templates.

From these figures, we find that less dusty star-forming galaxies tend to be distributed at the top left area (large green filled circle area), and more dusty star-forming galaxies tend to be distributed at relatively top right area compared with the less dusty population (large yellow filled circle area). Moreover, while in the *zJK* diagram the distribution of the DSFG population is relatively well separated from the other populations, in the *JHK* diagram the distribution of less dusty populations is close to or overlaps the distribution of more dusty populations. Thus, the *JHK* diagram is not suitable for discussing the existence of DSFGs, and then we use the *zJK* diagram bellow. We also note that the distribution of middle-age and young-age quiescent galaxies is close to or overlaps the distribution of less and/or more dusty populations although the oldest quiescent galaxies can be easily separated from the other populations. However, the young-age quiescent galaxies still have hot, massive, and short-lived OB-type stars, and they should have similar properties with on-going star-forming galaxies. Therefore, in principle, it is hard to distinguish the young-age quiescent galaxies from on-going star-forming galaxies, and at least the distribution of DSFGs is well separated from the distribution of the young-age quiescent galaxies. The middle-age quiescent galaxies will be a critical population for identifying the DSFGs because both the population occupy a similar region on the *zJK* diagram. The DSFGs tend to have a redder $z - J$ color and a bluer $J - K$ color (or a smaller height of the Balmer Break) than the middle-age quiescent galaxies. We will discuss the possibility of misidentifying the DSFGs in the following discussion.

Next, we plot our sample on the *zJK* diagram in Figure 5.10. The black dots represent the individual objects in our sample. In order to show the difference of the distribution between less and more dusty star-forming galaxies, we divide our sample into three sub-samples according to the best-fit dust attenuation value. From left to right, we show the sub-sample of (a) Av < 0.5, (b) $0.5 \leq$ Av < 1.0, and (c) Av ≥ 1.0. Moreover, we only show the reliable objects whose signal is detected at larger than 3σ level in all the *zJK*-band filters, and then the total number of the objects in this figure is ~ 1400. The yellow filled circles represent the median value for each color and sub-sample, and the orange error bars represent the average uncertainty for each color and sub-sample. The uncertainty of the color is calculated by an error propagation rule, and then the maximum uncertainty of the color in this figure is ~ 0.51[1]. The six colored dotted lines represent the model template tracks same as Figure 5.9, but we only plot the DSFG and quiescent galaxy templates and thus the color-coding is different. Moreover, we emphasize the redshift range of $3.5 < z < 4.5$ by solid lines on each the dotted lines. The cyan, light-green, and magenta lines denote the DSFG templates with Age = 10Myr, Age = 100Myr, and Age = 1Gyr, respectively. The blue, green,

[1]The signal to noise ratio (S/N) of objects we use here is larger than 3 in all the *zJK*-band filters. S/N = 3 corresponds to the magnitude error of $\Delta M = 0.36$, and hence the maximum uncertainty of a color is $\Delta\text{Color} = \sqrt{2 \times 0.36^2} = 0.51$

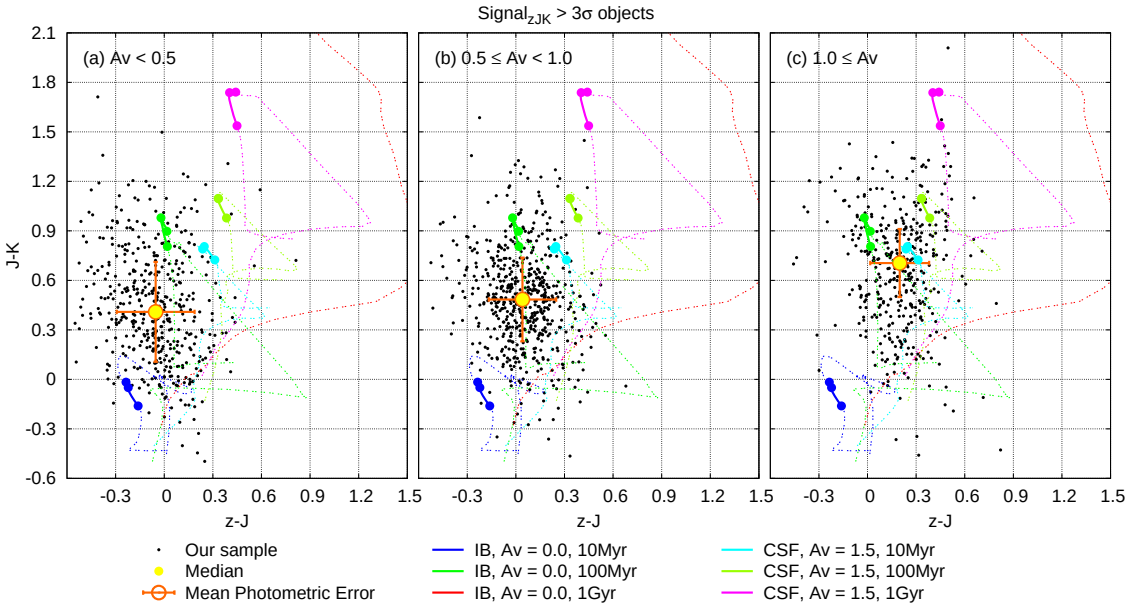

Figure 5.10: *zJK* Color-Color diagram. For each panel, the black dots represent the individual objects with (a) Av < 0.5, (b) $0.5 \leq$ Av < 1.0, and (c) Av ≥ 1.0 from left to right. The yellow filled circles with the orange error bars show the median value and the average uncertainty, respectively. The six colored dotted lines represent the model template tracks same as Figure 5.9, but we only plot the DSFG and quiescent galaxy templates. On each the dotted lines, we emphasize the redshift range of $3.5 < z < 4.5$ by solid lines. The cyan, light-green, and magenta lines denote the DSFG templates with Age = 10Myr, Age = 100Myr, and Age = 1Gyr, respectively. The blue, green, and red lines denote the quiescent galaxy templates with Age = 10Myr, Age = 100Myr, and Age = 1Gyr, respectively. The other parameters such as SFH, dust attenuation value, and metallicity are same as Figure 5.9.

and red lines denote the quiescent galaxy templates with Age = 10Myr, Age = 100Myr, and Age = 1Gyr, respectively.

Figure 5.10 indicates that the dusty objects tend to be distributed at a top right region where both $z - J$ and $J - K$ colors are redder. The median value of the dusty sub-sample indeed tends to have the redder $z-J$ and $J-K$ colors than that of the less dusty sub-sample. When taking account of the mean uncertainty of the color, the difference of the median values between the less dusty sub-samples (a) and (b) is marginal due to their large uncertainty. On the other hand, the most dusty sub-sample (c) can be separated from the other sub-samples even if we consider its uncertainty, and the most dusty objects are distributed on the DSFG area described as the green area in Figure 5.9. Furthermore, the distribution of the most dusty sub-sample can be reproduced by not the middle-age quiescent galaxies but the DSFG templates. Note that there are some outliers in all the panels, but most of them have a lower signal to noise ratio (S/N $\sim$ 3-5) in J and/or K-band compared with the other objects. Therefore, the above interpretation is not altered by these outliers. We conclude that the *zJK* color-color diagram also indicates the existence of the DSFGs and a part of star-forming

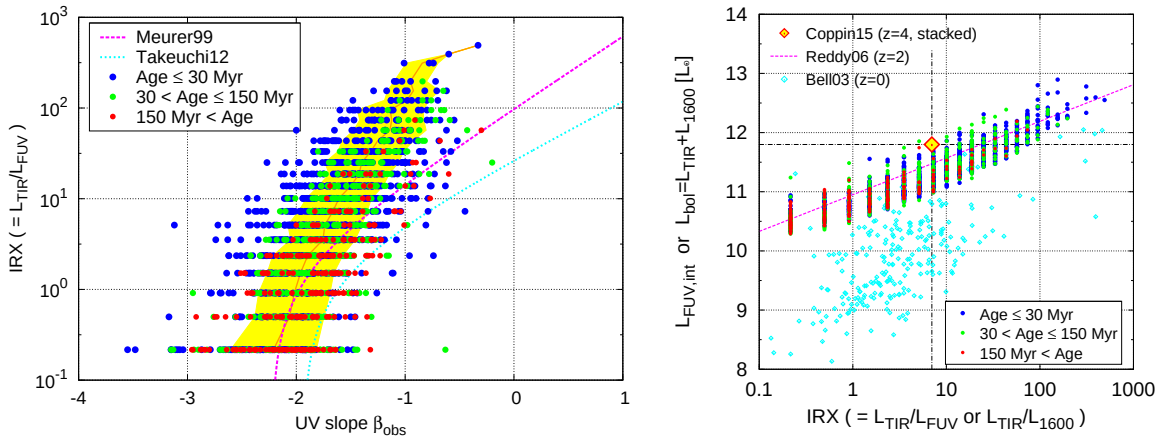

Figure 5.11: Left: IRX vs. observed UV slope. The IRX value is estimated by the empirical conversion between $\mathrm{IRX_{TIR-FUV}}$ and $\mathrm{A_{FUV}}$ reported by Burgarella et al. (2005b). The blue, green, and red points represent the best-fit age value of Age $\leq$ 30 Myr, 30 Myr $<$ Age $\leq$ 150 Myr, and 150 Myr $\leq$ Age, respectively. The orange line with the yellow filled region represents the average and standard deviation for each bin. The magenta and cyan dashed lines show the relation for the local starburst galaxies (Meurer et al. 1999; Takeuchi et al. 2012, respectively). Right: Bolometric luminosity vs. IRX. For simplicity, we use the intrinsic (dust-corrected) UV luminosity at the FUV filter as a bolometric luminosity for our sample. The blue, green, and red points represent the best-fit age value same as the left panel. The magenta dashed line represents the relation for $z \sim 2$ star-forming galaxies reported by Reddy et al. (2006) and the cyan diamonds represent the distribution of $z \sim 0$ galaxies reported by Bell (2003). The yellow diamond with the black dot-dashed lines represents the result for $z \sim 4$ galaxies from Coppin et al. (2015) in which the authors use the stacked 24-850 μm fluxes for estimating the IR luminosity.

galaxies at $z \sim 4$ in our sample is definitely classified as DSFGs.

5.5 *Implication for Most Active SFGs at* $z \sim 4$

We find that the intrinsically intense star-forming galaxies which have the blue β_{int} and bright $M_{\mathrm{UV},int}$ value, and these galaxies show the similar property of the most active star-forming galaxies at $z \sim 2$. In this section, we more directly compare the physical properties of $z \sim 4$ galaxies with those of $z \sim 2$ and 0 galaxies by estimating three physical quantities in somewhat independent ways.

Figure 5.11 shows the comparison of the UV slope, luminosity ratio of IR to UV (so called IRX), and bolometric (total) luminosity for the star-forming galaxies at $z \sim 4$, $z \sim 2$, and $z \sim 0$. All of the previous works use the sample observed with the rest-frame IR wavelength and estimate the total IR luminosity from the data. Our sample, however, does not have the rest-frame IR information for the individual objects and therefore we use the approximate conversion. For estimating the IRX value, we apply the empirical conversion between $\mathrm{IRX_{TIR-FUV}}$ and $\mathrm{A_{FUV}}$ reported by Burgarella et al. (2005b): $\mathrm{A_{FUV}}$ =

$-0.028[\log_{10}L_{\rm TIR}/L_{\rm FUV}]^3 + 0.392[\log_{10}L_{\rm TIR}/L_{\rm FUV}]^2 + 1.094[\log_{10}L_{\rm TIR}/L_{\rm FUV}] + 0.546$. Instead of the bolometric luminosity, for simplicity, we use the *intrinsic* FUV luminosity which is calculated by convolving the flux of the best-fit original (before reddening) template with the FUV filter. We emphasize that the cautious treatment is required for the comparison between our result and the previous results presented in this paper.

In the left panel of Figure 5.11, the IRX value is plotted as a function of the observed UV slope. The blue, green, and red points represent the best-fit value of Age $\leq$ 30 Myr, 30 Myr $<$ Age $\leq$ 150 Myr, and 150 Myr $\leq$ Age, respectively. The orange line with the yellow filled region represents the average and standard deviation for each bin. The magenta and cyan dashed lines show the relation for the local starburst galaxies (Meurer et al. 1999; Takeuchi et al. 2012, respectively). According to Reddy et al. (2006, 2010), the $z \sim 2$ star-forming galaxies with $L_{\rm TIR} < 10^{12}L_{\odot}$ are distributed along the M99 IRX-β relation, and the galaxies with $L_{\rm TIR} > 10^{12}L_{\odot}$ classified as Ultra Luminous InfraRed Galaxies (ULIRGs) are distributed above the M99 IRX-β relation. On the other hand, Takeuchi et al. (2012) shows that by measuring the IR and UV luminosity with same aperture size, the $z \sim 0$ star-forming galaxies are distributed along their relation. Compared with the two relations, our sample shows systematically bluer UV slope, and this systematic offset becomes larger at the larger IRX value. In particular, the latter trend implies the presence of ULIRG-type galaxies at $z \sim 4$. Although the systematic shift can be attributed to the overestimation of IRX which comes from the conversion from $A_{\rm FUV}$ to $IRX_{\rm TIR-FUV}$ and/or the failure of the SED fitting analysis, we consider that the possibility is low. This is because Burgarella et al. (2005b) demonstrate that the empirical conversion is applicable to the various type of local galaxies, and we check that the uncertainty of our SED fitting analysis is not large from Figures 5.1, 5.2, and 5.3(e.g., the change of the IRX value from 10^2 to 10^1 corresponds to the change of the Av value from ~ 1.6 to ~ 0.8, which is unlikely).

In the right panel of Figure 5.11, the bolometric luminosity is plotted as a function of the IRX value. The blue, green, and red points represent the best-fit age value same as the left panel. The magenta dashed line represents the relation for the $z \sim 2$ star-forming galaxies reported by Reddy et al. (2006) and the cyan diamonds represent the distribution of the $z \sim 0$ star-forming galaxies reported by Bell (2003). Both previous works do not use the UV luminosity at the FUV filter but the UV luminosity at 1600Å. This panel shows that the star-forming galaxies with the larger IRX value (= higher dust extinction) have the larger $L_{\rm bol}$ not only for $z \sim 2$ and 0 but also for $z \sim 4$. Furthermore the amplitude and slope of the relation for $z \sim 4$ are similar to the relation for $z \sim 2$.

We also refer to the recent result of sub-millimeter observation from Coppin et al. (2015) whose sample is quite similar to our sample. According to their work, the IR luminosity of the K-band detected LBG at $z \sim 4$ shows $L_{8-1000\mu{\rm m}} \approx 5.5 \times 10^{11}L_{\odot}$ which is estimated from the stacked fluxes at observed-frame 24-850 μm. This stacked SED also shows that the observed UV luminosity at 1700Å is $L_{1700} \approx 7.8 \times 10^{10}L_{\odot}$. Consequently, the typical LBG at $z \sim 4$ has IRX ≈ 7.0 and $L_{\rm bol} \approx 6.3 \times 10^{11}L_{\odot}$, which is plotted in the right panel of Figure 5.11 by the yellow diamond with the black dot-dashed lines. On the other hand, the median values of our sample are IRX $= 5.12$ and $L_{\rm bol} = 1.41 \times 10^{11}L_{\odot}$, which are smaller than the values of Coppin et al. (2015). First, this comparison indicates that the $z \sim 4$ LBGs are indeed significantly dust attenuated and there must be the IR luminous star-forming galaxies in our sample.

Second, our evaluation of the dust attenuation value for estimating the intrinsic β values is reasonable, or even somewhat underestimated. Finally, the difference between Coppin et al. (2015) results and ours can be due to the fact that the stacked point are the average weighted by luminosities while our median values are not. Future ALMA observations for individual detection will potentially solve the discrepancy.

5.6 *Dust Attenuation Law of Intrinsically Active SFGs at* $z \sim 4$

In the above discussion, we only consider the case of the Calzetti et al. (2000) attenuation law for dust extinction curve in the SED fitting analysis. However, it is clear that both intrinsic β and $M_{\rm UV}$ value strongly depend on the assumption of the dust attenuation law. In order to verify our result, we also do the same analysis assuming the SMC attenuation law from Prévot et al. (1984) and Bouchet et al. (1985) instead of the Calzetti et al. attenuation law. As a result, we obtain a hint of the dust attenuation law for high redshift star-forming galaxies. In the following of this section, we show and discuss the three results.

Figure 5.12 shows the comparison of the β_{int}-$M_{\rm UV,int}$ relation which is estimated from the Calzetti et al. attenuation law (Left) and SMC attenuation law (Right). The left panel is same as the bottom right panel of Figure 5.4. In the right panel, the color-coding is different from the left panel, and the blue, green, and red points represent the best-fit dust attenuation value of Av < 0.3, $0.3 \leq$ Av < 0.6, and $0.6 \leq$ Av, respectively. From this figure, we can again find that the intrinsic β value increases with the intrinsic $M_{\rm UV}$ value when using the SMC attenuation law. However the best-fit Av value in the case of the SMC attenuation law becomes much smaller than the case of the Calzetti et al. attenuation law. This is because the slope of the dust extinction curve of the SMC attenuation law is much steeper than that of the Calzetti et al. attenuation law. Consequently, we cannot identify the intrinsically active star-forming galaxies which show the high dust attenuation (Av > 1.5), blue β_{int} value ($\beta_{int} < -2.5$), and red β_{obs} value ($\beta_{obs} > -1.7$).

Figure 5.13 shows the results of the IRX-β relation (Left) and $L_{\rm bol}$-IRX relation (Right), which are same as Figure 5.11 but we use the SMC attenuation law. The left panel indicates that the distribution of the $z \sim 4$ galaxies is comparable to the IRX-β relation of Meurer et al. (1999) or most of the galaxies are distributed between Meurer et al. (1999) and Takeuchi et al. (2012). It means that we do not find the ULIRG-type galaxies in our sample and most of the $z \sim 4$ star-forming galaxies show the similar properties of the $z \sim 2$ and $z \sim 0$ star-forming galaxies. However, in the right panel, almost all of the galaxies are distributed in the area of $L_{\rm bol} < 10^{12} L_{\odot}$ and IRX $\lesssim 10$, and it is difficult to reproduce the stacked point from Coppin et al. (2015). Although there is still a large uncertainty in the stacked flux to be compared with our sample, it is preferable to apply the Calzetti et al. (2000) attenuation law for the intrinsically luminous LBGs at $z \sim 4$.

Finally, for more direct comparison between our results and Coppin et al. (2015), we estimate the flux density at observed-frame 850 μm, S_{850}, for individual objects in our sample. We first calculate the total (bolometric) IR luminosity by utilizing the NOT dust-corrected FUV luminosity and the IRX value as mentioned in Sections 5.2 and 5.5. If we assume

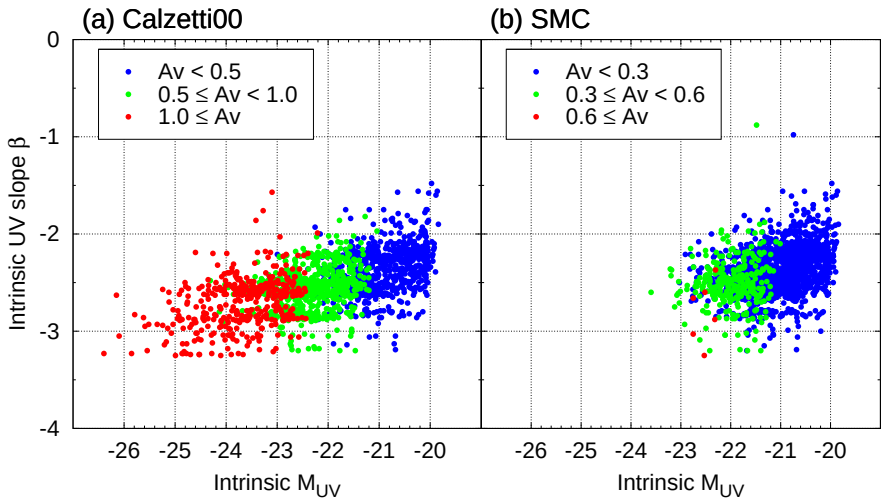

Figure 5.12: Comparison of β_{int}-$M_{\mathrm{UV},int}$ relation. The left panel is same as the bottom right panel of Figure 5.4. The right panel shows the case of the SMC attenuation law for dust extinction curve in the SED fitting analysis, and the blue, green, and red color-coding represent the objects with Av $<$ 0.3, 0.3 $\leq$ Av $<$ 0.6, and 0.6 $\leq$ Av, respectively.

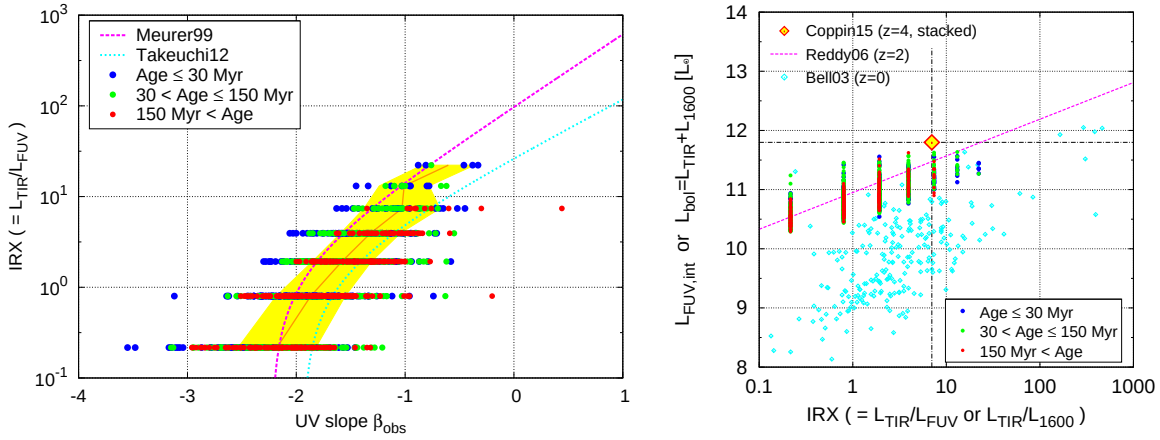

Figure 5.13: Same as Figure 5.11, but we use the SMC attenuation law for dust extinction curve instead of the Calzetti et al. (2000) attenuation law.

a spectrum of the dust thermal emission, we can predict the S_{850} value from the total IR luminosity. For modeling the dust thermal emission, we use the modified blackbody + power-law formula in which the spectrum is described as the modified blackbody assuming an optically thin case at the Rayleigh-Jeans side (smaller frequency) and as the power-law form

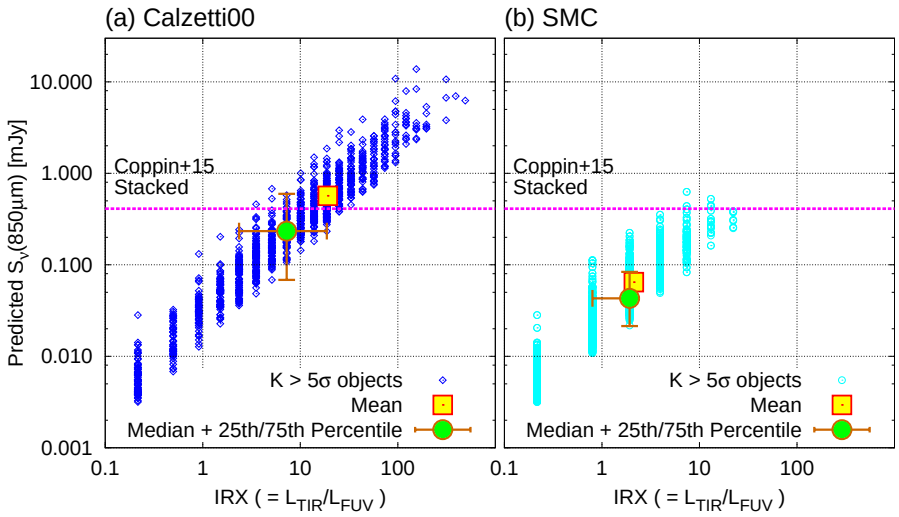

Figure 5.14: Predicted Flux density at observed-frame 850 μm for our sample. The left panel shows the case of the Calzetti et al. attenuation law, and the right panel shows the case of the SMC attenuation law in the SED fitting analysis. The vertical axis is the predicted S_{850} value and the horizontal axis is the IRX value. The blue open diamonds or cyan open circles represent the individual objects in our sample which are detected at larger than 5σ level in K-band. The yellow filled square denotes the average value, and the green filled circle with the brown error bars denote the median and 25th/75th percentile. The magenta dot line denotes the flux density measured in Coppin et al. (2015).

at the Wien side (larger frequency). This formula is,

$$S(\nu, T_d) \propto \begin{cases} \frac{\nu^\beta \nu^3}{e^{h\nu/kT_d}-1} & (\nu \leq \nu_c) \\ \nu^{-\alpha} & (\nu > \nu_c) \end{cases} \tag{5.1}$$

where $S(\nu, T_d)$ is the flux density at ν for a dust temperature T_d in the units of Jy and β is a dust emissivity index. The connecting frequency, ν_c, is calculated from,

$$\left.\frac{dS}{d\nu}\right|_{\nu=\nu_c} = -\alpha.$$

For simplicity, we fix all the above parameters and the source redshift referring to Coppin et al. (2015), that is, the dust temperature of $T_d = 38$K, the dust emissivity index of $\beta = 1.5$, the power-law index of $\alpha = 1.7$, and the source redshift of $z = 3.87$. We check the influence of the assumed source redshift on the predicted S_{850} value, and we find that the influence is marginal in the range of $z = 3.5$-4.5 because of the positive K-correction. For calculating the total IR luminosity, we integrate the modeled spectrum from 8μm to 1000μm in the rest-frame. As a result, we obtain a simple relation between the total IR luminosity and the predicted S_{850} value. We note that the main results of Coppin et al. (2015) are derived from the SED

template library constructed by Swinbank et al. (2014) and the modified blackbody + power-law formula is used just for checking the validity of the SED fitting analysis. Therefore, there appears to be a difference between the observed value from Coppin et al. (2015) and our prediction.

Figure 5.14 shows the prediction for the case of the Calzetti et al. attenuation law (Left) and the SMC attenuation law (Right). The vertical axis is the predicted S_{850} value and the horizontal axis is the IRX value. The blue open diamonds or cyan open circles represent the individual objects which are detected at larger than 5σ level in K-band in our sample. Because the sample in Coppin et al. (2015) consists of the K-band detected objects, we only use the $K > 5\sigma$ objects in this estimation. The yellow filled square denotes the average value, but the average is biased toward the larger S_{850} and IRX value since the predicted S_{850} value and the IRX value span four orders of magnitude. The green filled circle with the brown error bars denote the median and 25th/75th percentile. According to Coppin et al. (2015), the flux density measured for the stacked image is $S_{850} = 0.411 \pm 0.064$ mJy, and it is shown by the magenta dot line in both the panels. We omit the error bars of the S_{850} value of Coppin et al. (2015) from the figure because the uncertainty of the S_{850} value is quite small.

Clearly, the predicted S_{850} value is insufficient to reproduce the stacking result of Coppin et al. (2015), and hence at least the SMC attenuation law is unsuitable for high-z K-detected LBGs. On the other hand, it appears that the result from the Calzetti et al. attenuation law is consistent with the result of Coppin et al. (2015). In other words, the red color from observed-frame optical to NIR seen in a part of our sample is explained by neither the dust attenuation law with a steeper slope nor the old-age population. According to our estimation, the red color LBGs in our sample can be easily detected and measured by using the ALMA, and these galaxies can reveal not only the intrinsic properties of DSFGs but also the dust attenuation law of high-z star-forming galaxies.

Chapter 6

FUTURE PROSPECTS

In this chapter, we show two on-going studies and its future prospects; One is the study about the spatial clustering of star-forming galaxies, and the other is the study about the cosmic reionization. Regarding the spatial clustering, as mentioned in Section 1.3, we predict that the amplitude and slope of the ACF signal depend on the β value since extremely blue star-forming galaxies should be less clustered than redder star-forming galaxies. For verifying the prediction, we first investigate and consider the relation between the ACF signals and the β value for the SXDS sample. Actually, the sample size of the SXDS sample is not enough large to discuss the relation, and thus we second discuss the applicability of this study to the data set of the Subaru/HSC Strategic Survey Program (HSC-SSP). Regarding the cosmic reionization, we first introduce one unique idea proposed by Zackrisson et al. (2013) which utilizes the UV spectral slope β for estimating the escape fraction of Lyman Continuum photons. On the basis of this idea, we submitted a proposal, and then we were granted telescope time. The observation was conducted on HST 2016 August 27, and now we are in the process of the data reduction. Thus, we summarize the detail of the observation and the current status.

6.1 *Analysis of Angular Auto Correlation Function*

6.1.1 *Results from SXDS sample*

In order to reveal the dependence of ACF signals on β values, we divide the SXDS sample into two sub-samples with respect to the observed β value. One is the blue sub-sample which consists of the objects with $\beta_{obs} \leq -1.74$ and the other is the red sub-sample which consists of the objects with $\beta_{obs} > -1.74$. The criteria value of $\beta_{obs} = -1.74$ is the median value of the whole sample in the SXDS field.

The results for the whole sample, blue sub-sample, and red sub-sample are shown in Figure 6.1 by the green line with hatched region, blue points with error bars, and red points with error bars, respectively. To display the results for the blue and red sub-samples clearly, we plot the ACF signals with a small offset along the horizontal axis direction. We note that the errors of the ACF signals become quite large at $\Delta\theta \gtrsim 300''$ and therefore we basically consider the ACF signals at $\Delta\theta \lesssim 300''$. From the result for the whole sample (green), we

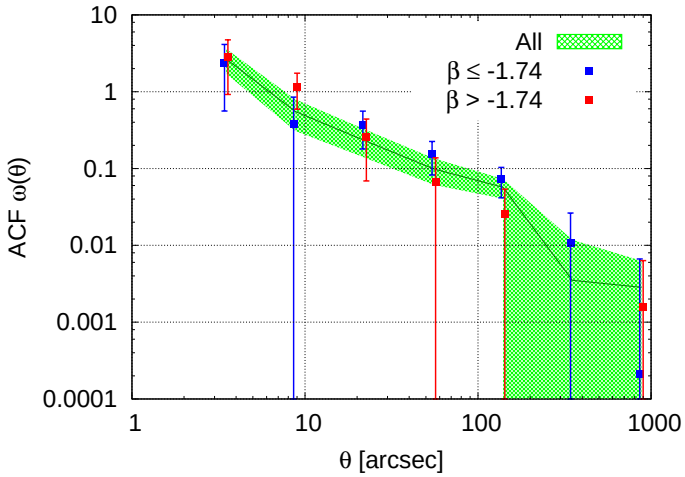

Figure 6.1: Angular auto-correlation function for whole samples, blue sub-sample ($\beta_{obs} \leq -1.74$), and red sub-sample ($\beta_{obs} > -1.74$). The green line with hatched region, blue points with error bars, and red points with error bars represent the whole sample, blue sub-sample, and red sub-sample, respectively. For emphasizing the deference of blue and red sub-sample, we draw the both plots with a small offset along the x-axis.

find that our result traces the trend of the previous studies for the $z \sim 4$ LBGs in the SXDS field (Ouchi et al. 2004, 2005). The slope of the ACF signals in $\Delta\theta \lesssim 20''$ differs from the slope in $100'' > \Delta\theta \gtrsim 20''$ even if we take account of the errors, and it can be explained by the composition of the one-halo and two-halo terms (e.g., Kravtsov et al. 2004). From the results of the blue and red sub-samples, we can see that the global trend of the ACF signals is not significantly different from the whole sample. However, due to the decrease of the sample size, the errors of them become larger than those of the whole sample. When we focus on the binned average values of the ACF signals, the blue sub-sample shows a lower signal at the small scale ($\Delta\theta \lesssim 10''$) but higher signal at the large scale ($\Delta\theta \gtrsim 10''$) than the red sub-sample.

The fitting results are tabulated in Table 6.1. From the third to fifth column, we show the fitting results by the IC corrected power-law form (Eq.3.3). From the sixth to ninth column, we also show the fitting results by the simple power-law form, $\omega(\theta) = A_\omega \theta^{1-\gamma}$, for the small scale ($\theta = 3''.5 - 22''$) and large scale ($\theta = 22'' - 139''$). All of the fitting results show that the blue sub-sample tends to have a smaller amplitude, A_ω, and shallower index, γ than the red sub-sample. As mentioned in the introduction, we expect that the objects with bluer β values would be solely distributed and the ACF signal becomes weaker than the redder one. Although the error is still large, it seems that the fitting results support this expectation. However Figure 6.1 also shows that the ACF signals of blue sub-sample become larger at $\theta \gtrsim 22''$ than the red ones since the red sub-sample shows the much steeper power-law index γ than that of the blue sub-sample (and whole sample). This is the result from the prominent one-halo term of the red sub-sample, and it may imply that the galaxies

in the red sub-sample are hosted by more massive dark matter halos than the galaxies in the blue sub-sample. According to our discussion described in Section 5.5, most of the galaxies in the red sub-sample are the intrinsically intense star-forming galaxies (or intrinsically blue β galaxies). Since SFR is proportional to stellar mass (main-sequence of star-forming galaxies described in Section 5.2), SFR is also expected to be proportional to dark matter halo mass. Indeed Bethermin et al. (2014) indicate that the clustering length slightly increases with increasing SFR. Therefore, we consider that the ACF analysis is consistent with the SED fitting analysis. Furthermore we should consider some extreme events such as gas rich merger if we explain the extreme condition of the intense star formation activity, the highly dust attenuation, and the bluest β_{int} value owing to the significant contribution from hot OB-type stars (e.g. young-age stellar population). In order to decrease the errors of the ACF signals and verify the above interpretation, we need a further investigation with a large sample and more detailed β sub-samples by utilizing the ultra-wide field survey data.

6.1.2 *Applying the Clustering Analysis to the HSC-SSP Data*

The final goal of the clustering analysis is to reveal the origin of the extremely/very blue star-forming galaxies. We can predict that the stars in the galaxies are formed from less metal-polluted HI gas, and hence the extremely/very blue star-forming galaxies should be less clustered than redder star-forming galaxies. In the previous section, we divided the SXDS sample into two sub-samples, and tried investigating the difference between the blue and red sub-samples. However, the uncertainties of the ACF signals are quite large, and it is sever to get a conclusion from the analysis. The large uncertainties are attributed to the small sample size of the SXDS sample, and we conclude that the SXDS sample is insufficient to investigate the extremely/very blue star-forming galaxies.

For the next step, we are planning to utilize the HSC-SSP data which is suitable to increase the sample size owing to the ultra-wide survey area. The HSC-SSP survey started in March 2014, and the program is on-going. The HSC-SSP is composed of three survey layers (wide, deep, and ultra deep), and all the layers are observed with Subaru/HSC *g, r, i, z*, and *y* broad-band filters. The five broad-band filters are best for investigating the $z \sim 4$ star-forming galaxies. When the survey is completed, the *deep* layer has the similar imaging depth with the SXDS data, but the much larger survey area than the SXDS data. The total area of the *deep* layer is as large as 27 deg^2 (the wide layer is 1400 deg^2 and the ultra deep layer is 3.5 deg^2), and it is $\sim$35 times larger than the SXDS data. Consequently, the HSC-SSP data set enables us to investigate the ACF of $z \sim 4$ star-forming galaxies for several β and $M_{\rm UV}$ sub-samples in detail.

In order to investigate $z \sim 4$ star-forming galaxies, we consider the best selection criteria based on the Lyman Break technique (Steidel & Hamilton 1992; Steidel et al. 1995, 1996) constructed from the filter set of Subaru/HSC by using the population synthesis model. Actually, Hildebrandt et al. (2009) investigate the color selection criteria for g-dropouts (LBGs at $z \sim 4$) constructed from the filter set of CFHT/MegaCam which has the *u, g, r, i*, and *z* broad-band filters. The response curve of the *g, r, i*, and *z*-band filters of CFHT/MegaCam is almost same as that of Subaru/HSC. Since the main selection criteria of Hildebrandt et al. (2009) requires the *g, r*, and *i*-band filters, we can simply apply the criteria to the HSC-SSP

data. However, the authors also use the u-band filter for excluding the contamination from low-z galaxies. Moreover, in the simulation of Hildebrandt et al. (2009), the authors use the population synthesis model of Bruzual & Charlot (1993) and the intergalactic medium (IGM) attenuation model of Madau (1995), which are relatively conservative. Therefore, we should consider the new color selection criteria constructed from the filter set of Subaru/HSC by using a recent population synthesis model and a recent IGM attenuation model, and it is very interesting to compare the detectability and/or the purity of the new criteria with that from Hildebrandt et al. (2009).

For making the color criteria, we use the population synthesis model of Bruzual & Charlot (2003), which is described in Section 3.2, and the IGM attenuation model of Inoue et al. (2014). The mean transmission at the Lyman series and Lyman continuum regime by Inoue et al. (2014) is higher than that by Madau (1995), and hence the Lyman Break calculated in our model is smaller than the previous work. We note that the absorption by neutral hydrogen in the IGM is stochastic, and the actual transmission can vary widely from sight-line to sight-line (Madau 1995; Inoue & Iwata 2008). For simplicity, we consider the templates constructed from two SFHs (Continuous Constant and Instantaneous Burst), two age values (10Myr and 1Gyr), one metallicity value ($Z = 0.2Z_{\odot}$), and two dust attenuation value (Av = 0.0 and 1.5). We assume the Calzetti et al. (2000) dust attenuation law, and at the wavelength shorter than Lyα ($\lambda \leq 1200$Å) we calculate the extinction curve assuming a linear function by extrapolating the Calzetti et al. extinction curve at $\lambda = 1200$ and 1300Å. For the filter response curve, we use the data obtained from the Subaru/HSC instrument Web Site[1] after multiplying the Quantum efficiency of FDCCD, the Transmittance of the dewar window, the Transmittance of the Primary Focus Unit of the HSC, and the Reflectivity of the Primary Mirror.

We propose the color-color diagram of $g-r$ vs. $i-z$ (*griz*-diagram) for selecting $z \sim 4$ LBGs, and it is shown in Figure 6.2. For comparison, we also show the color-color diagram of $g-r$ vs. $r-i$ (*gri*-diagram), which is adopted in Hildebrandt et al. (2009), in Figure 6.3. In both the figures, the left two panels show the model tracks calculated from the template of the Continuous Constant SFH, and the right two panels show the model tracks calculated from the template of the Instantaneous Burst SFH. The blue and cyan lines represent the model templates with Age = 10Myr and 1Gyr, respectively, but both the models have Av = 0.0. The red and magenta lines represent the model templates with Age = 10Myr and 1Gyr, respectively, but both the models have Av = 1.5. The small dots on each line denote the redshift intervals with $\Delta z = 0.1$, and the large three diamonds show the redshift of $z = 3.5$, 4.0, and 4.5 from small $g-r$ color to large $g-r$ color. The green cross marks denote the colors for various types of stars calculated from Pickles (1998) stellar spectral flux library. The black solid line is the color selection criteria we propose here (Figures 6.2) and the criteria of Hildebrandt et al. (2009, Figures 6.3).

According to our model calculation, it is difficult to pick up $z \sim 4$ LBGs by using the *gri*-diagram (Figure 6.3) because of the small $g-r$ color (or small Lyman Break). The small $g-r$ color is mainly attributed to the assumed IGM attenuation model in our calculation. In fact, we check that the $g-r$ color becomes larger and the color criteria of Hildebrandt

[1] `http://www.naoj.org/Observing/Instruments/HSC/sensitivity.html`

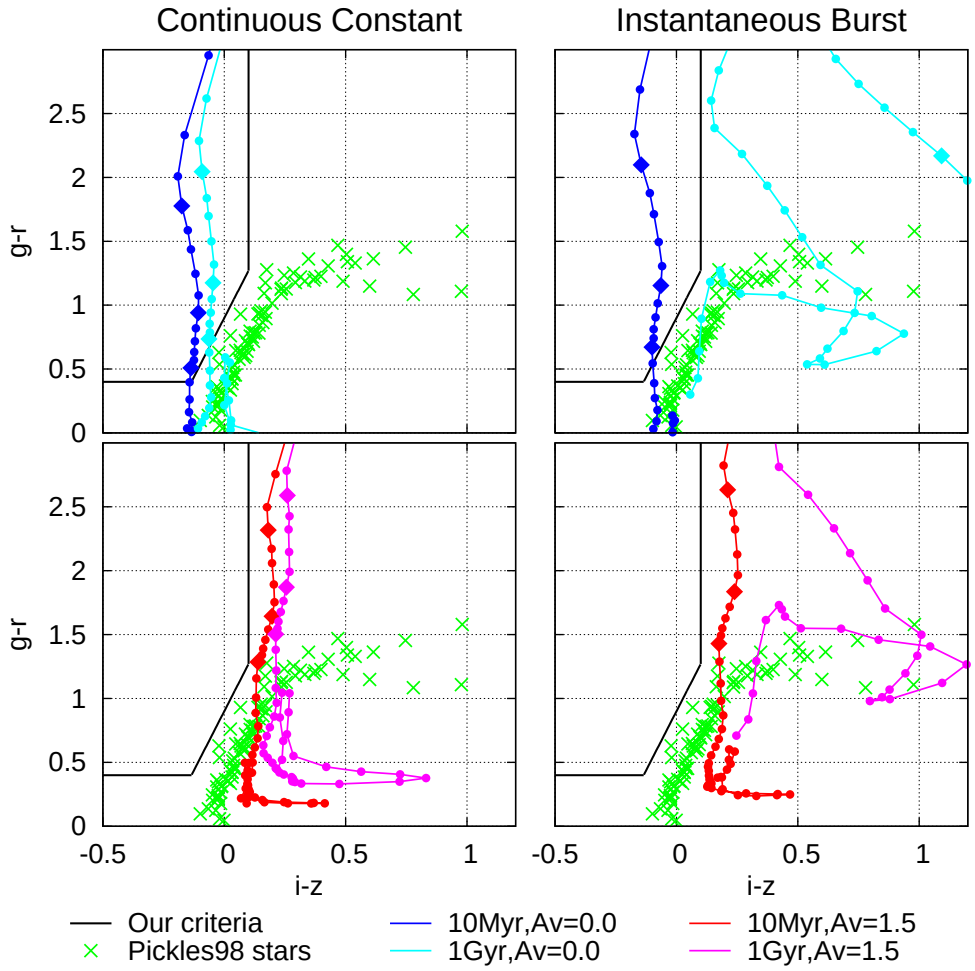

Figure 6.2: *griz* Color-Color diagram. The left two panels show the model tracks calculated from the template of the Continuous Constant SFH, and the right two panels show the model tracks calculated from the template of the Instantaneous Burst SFH. Both the blue and cyan lines represent the model templates with Av = 0.0, but the age value is Age = 10Myr (blue) and 1Gyr (cyan), respectively. Both the red and magenta lines represent the model templates with Av = 1.5, but the age value is Age = 10Myr (red) and 1Gyr (magenta), respectively. The small dots on each line denote the redshift intervals with $\Delta z = 0.1$, and the large three diamonds show the redshift of $z = 3.5$, 4.0, and 4.5 from bottom to top. The green cross marks denote the colors for various types of stars calculated from Pickles (1998) stellar spectral flux library. The black solid line is the color selection criteria we propose here.

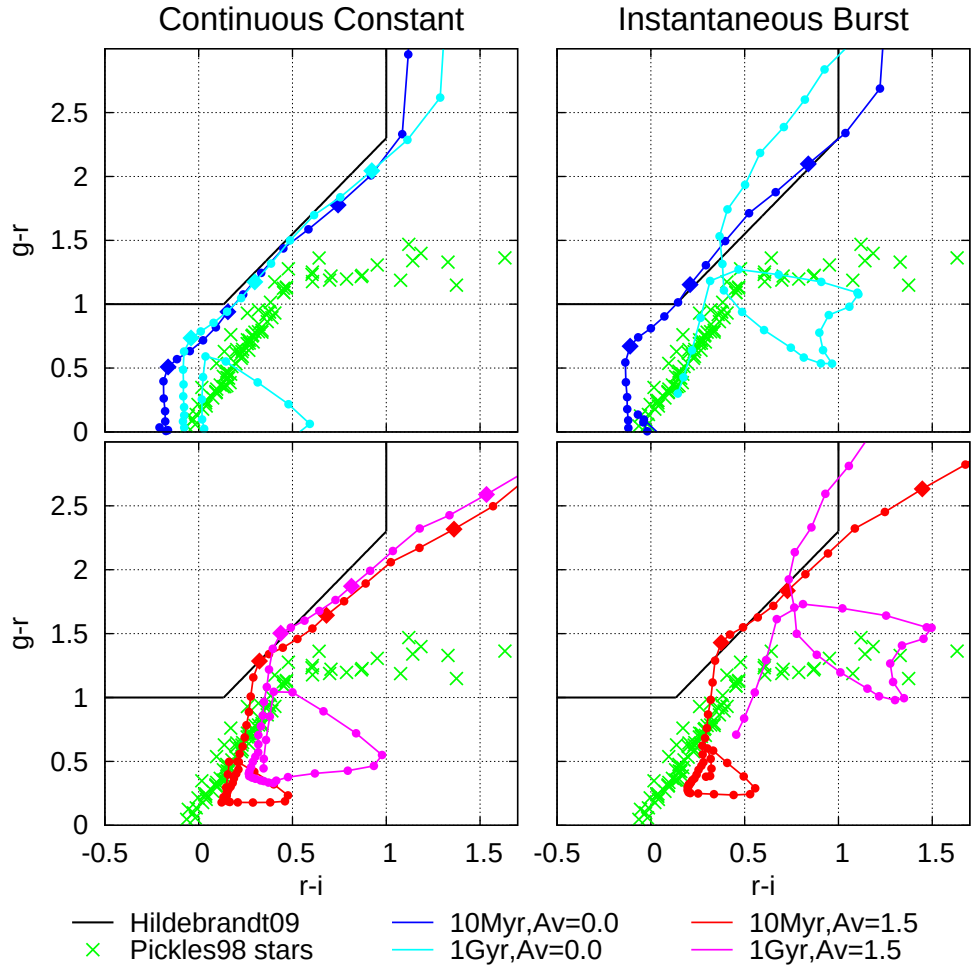

Figure 6.3: *gri* Color-Color diagram. Same as Figures 6.1, but the horizontal axis is the color of $r-i$. In this figure, the black solid line denotes the color selection criteria of Hildebrandt et al. (2009).

et al. (2009) can select $z \sim 4$ LBGs when assuming the IGM attenuation model of Madau (1995). Therefore, as mentioned above, we should use another color selection criteria for selecting $z \sim 4$ LBGs when assuming the recent IGM model. We investigate several color combinations, and then we propose the *griz*-diagram (Figure 6.2). In the figure, we also draw a line as the candidate of the color criteria. This criteria is intended to select the young and less dusty LBGs because our purpose is to investigate the extremely/very blue star-forming galaxies. This criteria indeed can separate the target galaxies from both DSFGs (red line in the left bottom panel) and old passive galaxies (cyan or magenta lines in the right two panels). However, if we compare the blue galaxies with the redder star-forming galaxies, we should change the $i-z$ color criteria. Since there seems to be the contamination from the low-z passive galaxies, we need to calibrate our color selection criteria by using spectroscopic

samples, and the investigation is on-going. We will quantify the contamination rate from the low-z galaxies and the detectability of $z \sim 4$ LBGs, and then we will do the clustering analysis.

Table 6.1: Summary of Fitting Results to ACF.

		IC corrected[a]			small scale[b]		large scale[b]	
Sample	N_{obj}	A_ω	$\gamma - 1$	IC/A$_\omega \times 10^3$	A_ω	$\gamma - 1$	A_ω	$\gamma - 1$
SXDS−All	1824	5.8 ± 1.3	0.98 ± 0.04	1.1	$13.1^{+12.0}_{-6.3}$	1.34 ± 0.29	$2.2^{+4.6}_{-1.5}$	0.75 ± 0.26
SXDS−Blue[c]	918	4.9 ± 1.4	0.87 ± 0.13	2.2	$6.7^{+17.6}_{-4.9}$	0.96 ± 0.49	$5.5^{+19.4}_{-4.3}$	0.88 ± 0.36
SXDS−Red[c]	906	16.6 ± 8.9	1.33 ± 0.17	0.12	$16.6^{+38.7}_{-11.6}$	1.29 ± 0.54	$12.4^{+165}_{-11.5}$	1.26 ± 0.70

[a] Calculated by the integral constant corrected formula, $\omega(\theta) = A_\omega(\theta^{1-\gamma} - \mathrm{IC}/A_\omega)$, over 3″.5-2210″

[b] Calculated by the simple power law formula, $\omega(\theta) = A_\omega\theta^{1-\gamma}$, over 3″.5-22″ (small scale) and 22″-139″ (large scale)

[c] The SXDS−Blue and Red sample is the sub-sample with $\beta_{obs} \leq -1.74$ and $\beta_{obs} > -1.74$, respectively

6.2 *EW(Hβ)-β Method*

6.2.1 *Background*

The reionization of neutral hydrogen in intergalactic medium (IGM) is one of the major event in the cosmic history. From the studies of the Lyα forest, the fraction of Lyα emitting galaxies, and the patchy kinetic Sunyaev-Zeldovich effect, it is considered that the transition from neutral phase to ionized phase completed at $z \gtrsim 6$ (e.g., Fan et al. 2002, 2006; Ono et al. 2012; Schenker et al. 2012; Zahn et al. 2012). The information of UV spectral slope β is also utilized for constraining the reionization (Duncan et al. 2015) because the β value can be a indicator of the production rate of hydrogen ionizing photons. However, the sources of the reionization is still unknown because of the uncertainty of the number density of faint star-forming galaxies and/or the fraction of hydrogen ionizing photons which escape from galaxies into the surrounding IGM, f_{esc}, at $z > 6$ (e.g., Madau et al. 1999; Finkelstein et al. 2012b, 2015).

The escape fraction can be measured as the ratio of observed to intrinsic number of ionizing photons (Lyman continuum, hereafter LyC, at $\lambda < 912$ Å) although there are some difficulties in estimating both of the observed and intrinsic number of LyC. The intrinsic number of LyC photons is derived from a model fit to the non-ionizing UV part of the spectrum ($\lambda \sim 1500$ Å), and thus it depends on the adopted galaxy SED model in which the dust attenuation, age, SFH, metallicity, and Initial Mass Function (IMF) is assumed. The direct observation for the escaped LyC photons from galaxies also has some uncertainties since the foreground IGM absorption by Lyα clouds or the foreground contamination from low-z galaxies becomes more severe for higher redshift galaxies (e.g., Inoue & Iwata 2008; Vanzella et al. 2010). Nevertheless f_{esc} values have been measured for galaxies at up to $z \sim$ 3-4 and there seems to be a trend that f_{esc} value increases with redshift from a few % ($z \sim$ 0-1) to 5-40% ($z \sim 3$) (e.g., Inoue et al. 2006; Bergvall et al. 2013) by using spectroscopic data, multi-band imaging data, and the high resolution imaging data observed with *Hubble Space Telescope (HST)*.

Since the foreground IGM absorption is stochastic, it may be possible to directly measure the f_{esc} values for galaxies at $z > 6$ if there is a clear sightline. However, the possibility is low even if the target galaxies are at $z \sim$ 3-4. Therefore, the *indirect* method for the measurement of the f_{esc} value, which is not affected by foreground IGM absorption, is required and has been suggested for the last several years (Zackrisson et al. 2013, 2016; Jones et al. 2013). Zackrisson et al. proposed a new idea to indirectly measure the f_{esc} value by using the Hβ line equivalent width (EW) and the rest-frame *intrinsic* UV spectral slope β (hereafter EW(Hβ)-β method). The method is based on a simple idea; A lower escape fraction of LyC photons absorbed in the HII regions of galaxies results in stronger nebular emission and a larger EW(Hβ). Consequently, a low f_{esc} corresponds to a high EW(Hβ), whereas a high f_{esc} corresponds to a low EW(Hβ). The intrinsic UV spectral slope β is a tracer of the production rate of LyC photons, and hence the EW(Hβ)-β diagram can be a useful tool for the measurement of the f_{esc} values.

Figure 6.4 shows the predictions from simple toy models (Left; Zackrisson et al. 2013) and SPH simulations (Right; Zackrisson et al. 2016). While the EW(Hβ)-β relation also depends on the age of star formation and/or metallicity, the four colored lines (Left) or dots (Right)

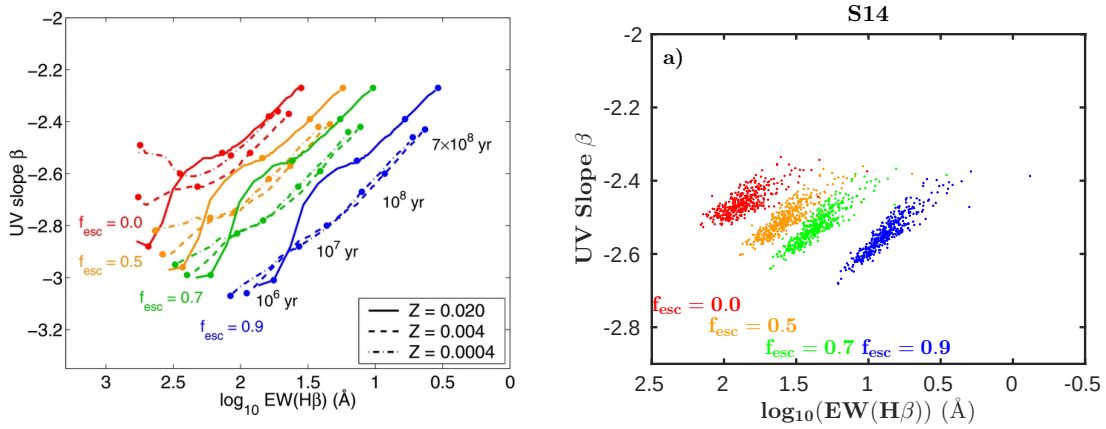

Figure 6.4: EW(Hβ)-β diagram predicted from the simple toy model (Left) and the SPH simulations (Right) in the case of dust-free. The four colored lines or dots represent different f_{esc} values described in the figure. In the left figure, the solid, dashed, and dot-dashed lines indicate the metallicity of $Z = Z_{\odot}$, $0.2Z_{\odot}$, and $0.02Z_{\odot}$, respectively. In the right figure, the dots represent individual galaxies at $z = 7$ from Simizu et al. (2014). *The figures are taken from Zackrisson et al. (2013, 2016).*

which represent the galaxies with $f_{esc} = 0.0$ (red), 0.5 (yellow), 0.7 (green), and 0.9 (blue) are well separated, respectively. It means that if we can measure the intrinsic (i.e., dust-free) β value as well as EW(Hβ), the f_{esc} value can be inferred. For example, if a galaxy has $\beta = -2.7$ and rest-frame EW(Hβ) of ~ 10 Å, $f_{esc} \sim 0.9$ is expected. With this method, f_{esc} values can be observationally obtained even for galaxies at $z > 6$ by using future instruments such as *JWST*.

Before applying this new interesting idea to galaxies at $z > 6$, the method needs to be verified for galaxies for which f_{esc} values have already been obtained through more direct method. For this purpose, we submitted a proposal in which we target two LyC galaxies at $z_{spec} = 3.2$ and a dozen of galaxies at $z_{phot} \sim 3.2$ whose LyC was measured with NB359 narrow-band filter. The proposal was accepted in Subaru Proposal S16B semester (Proposal ID:S16B-012, PI:Yamanaka), and the observation was conducted on 2016 August 27. Therefore, we now get a opportunity to check this method.

6.2.2 *Spectroscopic Observation and Current Status*

We conducted NIR multi-object spectroscopy with the Multi-Object Spectrometer For Infra-Red Exploration (MOSFIRE; McLean et al. 2010, 2012) on the Keck-I 10m telescope. The data was obtained on HST 2016 August 27, and the night was photometric with seeing $0''.4-0''.6$. A total of four masks was observed using the ABA′B′ dithering pattern with the nod amplitude of $3''.0$ (A-B) and $2''.4$ (A′-B′). Except for one object in the SSA22 field mask, we used slit widths of $0''.7$ which corresponds to the spectral resolution $R = 3610$ in the K-band and $R = 3388$ in the Y-band.

Two of the four masks are our main masks for the candidates of $z_{spec} = 3.2$ LyC galaxies in the SSA22 field which is selected from Iwata et al. (2009) and Micheva et al. (2016). In each mask, we assigned one slit on one LyC galaxy (hereafter we call the objects as LCG1

Table 6.2: Summary of Spectroscopic Data

Mask No.	Field	Filter	Target Objects	Target features	Exp. Time
1	SSA22	K	LCG1, LBGs, LAEs	[OIII]λ5007, Hβ	8820s[a]
2	SSA22	K	LCG2, LBGs, LAEs	[OIII]λ5007, Hβ	1800s
3	SXDS	K	Dusty LBGs	Hβ	3420s
4	ELAIS-N1	Y	Proto-Cluster Candidate	Balmer Break	2160s

[a] In our observation, almost the first half night was lost due to the telescope trouble. This value is the sum of the *safe* science frame observed in the first and second half night. If we only use the science frame in the second half night, the exposure time is 7920s. However, if we include the suspicious science frame in the first night, the exposure time becomes 9540s.

and LCG2). In addition to the LCG1 and LCG2, we also assigned slits on the LBGs and LAEs with photometric redshift $z_{phot} \sim 3.2$. The purpose of the observation is to determine the spectroscopic redshift by strong emission lines such as [OIII] λ5007, and to measure the Hβ emission line flux. For this purpose, these two masks were observed in K-band filter. Net exposure times are 8820s and 1800s, respectively, although we lost the almost first half-night because of telescope trouble. The other two of four masks are prepared for effectively utilizing the telescope time before and after the main observation. One mask is for the $z \sim 4$ LBGs with red β value in the SXDS field. This mask was observed in K-band filters. The other mask is for the candidates of $z \sim 2$ proto-cluster member in the ELAIS-N1 field (T. Yamada, private communication). This mask was observed in Y-band filters. Net exposure times are 3420s and 2160s, respectively. The mask information is summarized in Table 6.2.

The data reduction was performed by using the MOSFIRE data reduction pipeline (DRP)[2] which was developed by the MOSFIRE instrument team. As a result, we obtained the 2-D stacked spectra which were flat-fielded, wavelength calibrated, rectified, and sky subtracted. In the wavelength calibration procedure for K-band, we found the best solution for each slit from a combination of OH night sky lines and arc lines of a Neon lamp. By default, an Argon arc lamp is also prepared, and indeed we obtained the data of the Argon arc lines in the afternoon calibration. However, the combination of OH night sky lines, arc lines of the Neon, and Argon lamps did not work well, and the wavelength solution was not found. Therefore, we used the combination of OH night sky lines and arc lines of the Neon lamp for the K-band wavelength calibration. The one-dimensional (1-D) spectra with their 1σ error were extracted from the final 2-D spectra by using the BMEP[3] software which was developed by the MOSFIRE Deep Evolution Field (MOSDEF) team. This software is useful to detect and identify the faint emission lines and continuum, and the extraction is conducted with a boxcar aperture. The extracted spectrum of bright objects were compared with the spectrum extracted by the IRAF apall task, and we confirmed that both the spectra were consistent.

[2] `https://keck-datareductionpipelines.github.io/MosfireDRP/`
[3] `https://github.com/billfreeman44/bmep`

As for flux calibration, we observed a telluric standard A0V star, HIP 80974, when the star was at similar airmass with the science frames. Since the observed wavelength range depends on the position in the mask, the standard longslit observation cannot always cover the entire wavelength range if a science target is at the edges of the mask. In order to acquire the standard spectrum which covers the accessible wavelength range at K-band, we adopted the 'long2pos_specphot' procedure. This procedure has been developed by the instrument team, and a custom mask in which there are two slits to sample both of the longer and shorter wavelength range is prepared. In this procedure, we can also calibrate slit-losses assuming both the target objects and standard star are spatially-unresolved point sources.

Now, we are working on the flux calibration. Owing to the telescope trouble, there is a difficulty in the process of the flux calibration. We will try some methods which enable us to complete the calibration, and then we will measure the flux of the Hβ emission line and estimate the EW(Hβ) by utilizing the imaging data.

Chapter 7

SUMMARY

In this work, we investigate the UV slope β, stellar population, and spatial distribution of bright star-forming galaxies at $z \sim 4$ in the SXDS field which is the wide-area and deep survey field. We use the imaging data of SXDS/$BVRi'z'$, Subaru/updated-z', UDS/JHK, *HST*/F125WF160W, and *Spitzer*/3.6μm 4.5μm, and we construct the sample of star-forming galaxies at $z \sim 4$ by both Lyman Break technique and photometric redshift selection. The UV slope β is calculated by the simple power-law fit. Our main results are described below.

- We find that there is little dependence of the observed UV slope β on the absolute UV magnitude M_{UV} in the range of $-22.0 \lesssim M_{UV} \lesssim -20.0$. The slope of the β-M_{UV} relation is -0.04 ± 0.02, and it is more shallower than the previous studies for similar redshift (e.g., -0.13 ± 0.02 from Bouwens et al. 2014 and -0.10 ± 0.03 from Kurczynski et al. 2014).

- In order to illustrate the effect of the incompleteness to the observed β-M_{UV} distribution, we estimate the recovery fraction which is the ratio of re-collected objects to input objects. Our simulation indicates that the observed global trend of β-M_{UV} relation is mainly formed by some physical reasons, not our sample selection.

- For considering the dependence of the UV slope on the dust attenuation, age, metallicity, and SFH, we introduce and investigate the *intrinsic* (dust-corrected) UV slope, β_{int}, and *intrinsic* absolute UV magnitude, $M_{UV,int}$, by using the results of the SED fitting analysis. Interestingly, the intrinsic UV slope increases with the intrinsic absolute UV magnitude, and the star-forming galaxies with the bluest β_{int} and brightest $M_{UV,int}$ value are the dusty population, and then resulting the red β_{obs} value. Due to such population, we see the flat β_{obs}-$M_{UV,obs}$ distribution.

- We find that the β_{int}-$M_{UV,int}$ relation does not depend on the assumption of the SFH. Although there is a degeneracy between the dust attenuation and age, it is not critical for the β_{int}-$M_{UV,int}$ relation. These results support the above interpretation.

- The intersection point of the β_{int}-$M_{UV,int}$ relation and β_{obs}-$M_{UV,obs}$ relation would represent the position of the appearance of nearly dust-free population. We calculate this intersection point and it is at $\beta = -1.97$ and $M_{UV} = -18.6$ which is close to the break point of β_{obs}-$M_{UV,obs}$ relation reported by Bouwens et al. (2014). Therefore in order to find the extremely metal-poor or metal-free galaxies, it is efficient to search extremely blue β galaxies with $M_{UV,obs} \gtrsim -19.0$.

- Since the photometric uncertainty of optical broad-band filters is typically smaller than that of NIR broad-band filters, the SED fitting analysis tends to select best-fit SEDs which well reproduce the photometries of optical broad-band filters. Therefore, it is useful to directly compare the observed color of the zJK-band filters with the expected color of DSFGs, dust-free SFGs, and quiescent galaxies. We find that the observed color of the most dusty sub-sample (Av $\geq$ 1.0) is well reproduced by the color of DSFGs. When taking account of the mean photometric error, the distribution of the most dusty sub-sample can be separated from the expected color of dust-free SFGs and quiescent galaxies. Thus, a part of star-forming galaxies at $z \sim 4$ in our sample is definitely classified as DSFGs.

- We estimate the IRX (= L_{TIR}/L_{FUV}) value and bolometric (total) luminosity. We compare the distribution of IRX-β_{obs} and L_{bol}-IRX for $z \sim 4$ with those of $z \sim 2$ and 0 and find that the IRX-β_{obs} relation of $z \sim 4$ is similar to that of $z \sim 2$ at the smaller IRX range (IRX $\sim$ 1) while the relation of $z \sim 4$ departs from that of $z \sim 2$ toward the bluer β value at the larger IRX range (IRX $\gtrsim$ 10). We also find that the L_{bol}-IRX relation of $z \sim 4$ is similar to that of $z \sim 2$ rather than $z \sim 0$ over the sampled IRX range. Both results indicate that a significant fraction of $z \sim 4$ LBGs are the highly dust attenuated population and there must be the IR luminous star-forming galaxies such as ULIRGs in our sample.

- We also conduct the SED fitting analysis assuming the SMC attenuation law for dust extinction curve instead of the Calzetti et al. (2000) attenuation law. In this case, while the trend of the β_{int}-$M_{UV,int}$ relation does not change, we cannot identify the dusty active star-forming population and most of the galaxies are distributed between the relation of Meurer et al. (1999) and Takeuchi et al. (2012) on the IRX-β space. However the result of the L_{bol}-IRX relation does not appear to be consistent with the stacked result from Coppin et al. (2015). For more direct comparison, we estimate the flux density at observed-frame 850μm (S_{850}) for our sample, and the predicted S_{850} value from the SMC attenuation law is indeed insufficient to reproduce the result from Coppin et al. (2015). Thus, the Calzetti et al. attenuation law is preferable to the SMC attenuation law for the $z \sim 4$ intrinsically luminous LBGs.

- As first future prospect, we investigate and discuss the relation between ACF signals and β values for the SXDS sample, and then we consider the potential of the HSC-SSP data. We calculate the ACF for the whole sample, $\beta_{obs} \leq -1.74$ (blue) sub-sample, and $\beta_{obs} > -1.74$ (red) sub-sample. Our analysis shows the sign of the ACF signal excess for the red sub-sample at the small scale ($\theta \lesssim 22''$) due to the large amplitude and much steeper power-law index of the ACF signals. It probably means that the intrinsically intense star-forming galaxies are hosted by more massive dark matter halos since most of the galaxies in the red sub-sample are the intrinsically intense star-forming galaxies. However the errors of the ACF analysis is still large, and we need a further investigation. By using the HSC-SSP data, we can easily increase the sample size owing to the extremely wide survey area. We have already made the color selection criteria for $z \sim 4$ LBGs, and we will calibrate it from the spectroscopic samples.

- As second future prospect, we introduce one interesting idea proposed by Zackrisson et al. (2013). The idea utilizes the UV spectral slope β for estimating the escape fraction of Lyman Continuum photons which is important quantity for revealing the source of cosmic reionization. In order to verify the new idea, we conducted NIR multi-object spectroscopy on HST 2016 August 27. We summarize the detail of the spectroscopic observation and the method of the data reduction. Now, we are working on the flux calibration.

Acknowledgement

At the outset, I would like to express the deepest appreciation to my supervisor, Professor Toru Yamada, for his guidance and support. From the time I entered the master course of the Tohoku University Astronomical Institute, he has taught me fundamentals of observational astronomy and high redshift galaxies. After I went to the doctor course, he has provided me the continuous guidance although he has been busy. In particular, when I had prepared to submit an academic paper and proposals, he had thoroughly discussed the contents with me without warring about time. His advice has precisely made me realize the weakness in my discussion and come up with new ideas. I will never forget what I learn for last five years.

I would like to offer my thanks to the three referees of my thesis, Professor Masashi Chiba, Associate Professor Masayuki Akiyama, and Associate Professor Takashi Murayama. Many important comments from them improve this thesis.

I am deeply indebted to all the members of the Astronomical Institute. My colleagues, Daisuke Toyouchi, Masayo Morioka, Takahiro Morishita, Takuya Otsuka, and Toshiyuki Mizuki, have provided me a lot of advice and have stimulated me. My research life has been very exciting thanks to them. Yamada group members, Mariko Kubo, Ken Mawatari, Yuki Kimura, Stevanus K. Nugroho, and Kohei Shinoka, have given me a great deal of advice on the data reduction, and have discussed my research with me. In addition, in the weekly meeting, Prof. Yamada and they have introduced newest academic papers which have been always interesting me.

I would like to thank Akio Inoue, Erik Zackrisson, Ikuru Iwata, and Genoveva Micheva for helpful comments for our proposal. We had submitted and revised our proposal many times, and finally we were granted telescope time of Keck/MOSFIRE. We did not get the telescope time without their great supports. I appreciate the authors and the editor-in-chief of ApJ and A&A for the permission to use their figures in this thesis. This work was supported by JSPS KAKENHI Grant Number JP26400217.

Last of all, I am deeply grateful to my parents, brother, and grandparents for their continuous supports.

Bibliography

Ashby, M. L. N., Willner, S. P., Fazio, G. G., et al. 2013, ApJ, 769, 80

Álvarez-Márquez, J., Burgarella, D., Heinis, S., et al. 2016, A&A, 587, A122

Banerji, M., Chapman, S. C., Smail, I., et al. 2011, MNRAS, 418, 1071

Baugh, C. M., Lacey, C. G., Frenk, C. S., et al. 2005, MNRAS, 356, 1191

Bastian, N., Covey, K. R., Meyer, M. R., 2010, ARA&A, 48, 339

Bell, E. F., 2003, ApJ, 586, 794

Bergvall, N., Leitet, E., Zackrisson, E., & Marquart, T. 2013, A&A, 554, A38

Bertin, E. & Arnouts, S., 1996, A&AS, 117, 393

Bethermin, M., Kilbinger, M., Daddi, E., et al. 2014, A&A, 567, 103

Berlind, A. A., & Weinberg, D. H., 2002, ApJ, 575, 587

Bielby, R. M., Shanks, T., Weilbacher, P. M., et al. 2011, MNRAS, 414, 2

Bielby, R., Hill, M. D., Shanks, T., et al. 2013, MNRAS, 430, 425

Bielby, R. M., Tummuangpak, P., Shanks, T., et al. 2016, MNRAS, 456, 4061

Bolzonella, M., Miralles, J.-M., Pello, R., et al. 2000, A&A, 363, 476

Bouchet, P., Lequeux, J., Maurice, E., Prévot, L., & Prévot-Burnichon, M. L. 1985, A&A, 149, 330

Bouwens, R. J., Illingworth, G. D., Franx, M., et al. 2009, ApJ, 705, 936

Bouwens, R. J., Illingworth, G. D., Oesch, P. A., et al. 2010, ApJL, 708, L69

Bouwens, R. J., Illingworth, G. D., Oesch, P. A., et al. 2012, ApJ, 754, 83

Bouwens, R. J., Illingworth, G. D., Oesch, P. A., et al. 2014, ApJ, 793, 115

Bouwens, R. J., Illingworth, G. D., Oesch, P. A., et al. 2015, ApJ, 811, 140

Bouwens, R. J., Smit, R., Labbé, I., et al. 2016a, ApJ, 831, 176

Bouwens, R. J., Aravena, M., Decarli, R., et al. 2016b, ApJ, 833, 72

Bruzual A., G., & Charlot, S. 1993, ApJ, 405, 538

Bruzual, G. & Charlot, S., 2003, MNRAS, 344, 1000

Burgarella, D., Buat, V., Small, T., et al. 2005a, ApJL, 619, L63

Burgarella, D., Buat, V. & Iglesias-Páramo, J., 2005b, MNRAS, 360, 1413

Burgarella, D., Buat, V., Gruppioni, C., et al. 2013, A&A, 554, A70

Calzetti, D., Kinney, A. L., Storch-Bergmann, T., 1994, ApJ, 429, 582

Calzetti, D., Armus, L., Bohlin, R. C., et al. 2000, ApJ, 533, 682

Capak, P. L., Carilli, C., Jones, G., et al. 2015, Nature, 522, 455

Casali, M., Adamson, A., Alves de Oliveira, C., et al. 2007, A&A, 467, 777

Casey, C. M., Scoville, N. Z., Sanders, D. B., et al. 2014, ApJ, 796, 95

Chapman, S. C., Blain, A. W., Smail, I., & Ivison, R. J. 2005, ApJ, 622, 772

Chapin, E. L., Pope, A., Scott, D., et al. 2009, MNRAS, 398, 1793

Coppin, K. E. K., Geach, J. E., Almaini, O., et al. 2015, MNRAS, 446, 1293

de Barros, S., Vanzella, E., Amorín, R., et al. 2016, A&A, 585, A51

Dessauges-Zavadsky, M., D'Odorico, S., Schaerer, D., et al. 2010, A&A, 510, A26

Duncan, K., Conselice, C. J., Mortlock, A., et al. 2014, MNRAS, 444, 2960

Duncan, K. & Conselice, C. J., 2015, MNRAS, 451, 2030

Dunlop, J. S., McLure, R. J., Robertson, B. E., et al. 2012, MNRAS, 420, 901

Dunlop, J. S., Rogers, A. B., McLure, R. J., et al. 2013, MNRAS, 432, 3520

Erb, D. K., Shapley, A. E., Pettini, M., et al. 2006, ApJ, 644, 813

Erb, D. K., Pettini, M., Shapley, A. E., et al. 2010, ApJ, 719, 1168

Fan, X., Narayanan, V. K., Strauss, M. A., et al. 2002, AJ, 123, 1247

Fan, X., Strauss, M. A., Becker, R. H., et al. 2006, AJ, 132, 117

Finkelstein, S. L., Papovich, C., Rudnick, G., et al. 2009, ApJ, 700, 376

Finkelstein, S. L., Papovich, C., Salmon, B., et al. 2012a, ApJ, 756, 164

Finkelstein, S. L., Papovich, C., Ryan, R. E., et al. 2012b, ApJ, 758, 93

Finkelstein, S. L., Ryan, R. E., Jr., Papovich, C., et al. 2015, ApJ, 810, 71

Fukugita, M., Ichikawa, T., Gunn, J. E., et al. 1996, ApJ, 111, 1748

Furusawa, H., Kosugi, G. & Akiyama, M., et al. 2008, ApJS, 176, 1

Furusawa, H, Kashikawa, N, Kobayashi, M. A. R., et al. 2016, ApJ, 822, 46

Grogin, N. A., Kocevski, D. D., Faber, S. M., et al. 2011, ApJS, 197, 35

Groth, E. J. & Peebles, P. J. E. 1977, ApJ, 217, 385

Gruppioni, C., Pozzi, F., Rodighiero, G., et al. 2013, MNRAS, 432, 23

Griffin, M. J., Abergel, A., Abreu, A., et al. 2010, A&A, 518, L3

Hambly, N. C., Collins, R. S., Cross, N. J. G., et al. 2008, MNRAS, 384, 637

Hao, Cai-Na, Kennicutt, R. C., Johnson, B. D., et al. 2011, ApJ, 741, 124

Hathi, N. P., Le Fèvre, O., Ilbert, O., et al. 2016, A&A, 588, A26

Hayashino, T., Matsuda, Y., Tamura, H., et al. 2004, AJ, 128, 2073

Heckman, T. M., Robert, C., Leitherer, C., Garnett, D. R., & van der Rydt, F. 1998, ApJ, 503, 646

Heinis, S., Buat, V., Béthermin, M., et al. 2013, MNRAS, 429, 1113

Hewett, P. C., Warren, S. J., Leggett, S. K., & Hodgkin, S. T., 2006, MNRAS, 367, 454

Hickox, R. C., Wardlow, J. L., Smail, I., et al. 2012, MNRAS, 421, 282

Hildebrandt, H., Pielorz, J., Erben, T., et al. 2009, A&A, 498, 725

Hodgkin, S. T., Irwin, M. J., Hewett, P. C., & Warren, S. J., 2009, MNRAS, 394, 675

Holland, W. S., Robson, E. I., Gear, W. K., et al. 1999, MNRAS, 303, 659

Hopkins, P. F., Hernquist, L., Cox, T. J., & Kereš, D. 2008, ApJS, 175, 356-389

Inoue, A. K., Iwata, I., & Deharveng, J.-M. 2006, MNRAS, 371, L1

Inoue, A. K., & Iwata, I. 2008, MNRAS, 387, 1681

Inoue, A. K., Shimizu, I., Iwata, I., & Tanaka, M. 2014, MNRAS, 442, 1805

Iwata, I., Inoue, A. K., Matsuda, Y., et al. 2009, ApJ, 692, 1287

Jones, T. A., Ellis, R. S., Schenker, M. A., & Stark, D. P. 2013, ApJ, 779, 52

Kashikawa, N., Yoshida, M., Shimasaku, K., et al. 2005, ApJ, 637, 631

Kennicutt, R. C., Jr. 1998, ARA&A, 36, 189

Kennicutt, Jr, R. C., & Evans, II, N. J., 2012, ARA&A, 50, 531

Koekemoer, A. M., Faber, S. M., Ferguson, H. C., et al. 2011, ApJS, 197, 36

Koornneef, J., & Code, A. D. 1981, ApJ, 247, 860

Kong, X., Charlot, S., Brinchmann, J., & Fall, S. M. 2004, MNRAS, 349, 769

Kurczynski, P., Gawiser, E., Rafelski, M., et al. 2014, ApJL, 793, L5

Kravtsov, A. V., Berlind, A. A., Wechsler, R. H., et al. 2004, ApJ, 609, 35

Landy, S. D. & Szalay, A. S., 1993, ApJ, 412, 64

Larson, K. L., Sanders, D. B., Barnes, J. E., et al. 2016, ApJ, 825, 128

Lawrence, A., Warren, S. J., Almaini, O., et al. 2007, MNRAS, 379, 1599

Lee, K.-S., Dey, A., Reddy, N., et al. 2011, ApJ, 733, 99

Le Floc'h, E., Papovich, C., Dole, H., et al. 2005, ApJ, 632, 169

Leitherer, C., Schaerer, D., Goldader, J. D., et al. 1999, ApJS, 123, 3

Lemke, D., Klaas, U., Abolins, J., et al. 1996, A&A, 315, L64

Ling, E. N., Frenk, C. S. & Barrow, J. D., 1986, MNRAS, 223, 21

Madau, P. 1995, ApJ, 441, 18

Madau, P., Pozzetti, L., & Dickinson, M. 1998, ApJ, 498, 106

Madau, P., Haardt, F., & Rees, M. J. 1999, ApJ, 514, 648

Madau, P., & Dickinson, M. 2014, ARA&A, 52, 415

Magnelli, B., Elbaz, D., Chary, R. R., et al. 2011, A&A, 528, A35

Magnelli, B., Popesso, P., Berta, S., et al. 2013, A&A, 553, A132

Maiolino, R., Nagao, T., Grazian, A., et al. 2008, A&A, 488, 463

McLean, I. S., Steidel, C. C., Epps, H., et al. 2010, Proc. SPIE, 7735, 77351E-77351E-12

McLean, I. S., Steidel, C. C., Epps, H. W., et al. 2012, Proc. SPIE, 8446, 84460J

Muerer, G. R., Heckman, T. M. & Calzetti, D., 1999, ApJ, 521, 64

Micheva, G., Iwata, I., Inoue, A. K., et al. 2017, MNRAS, 465, 316

Naidu, R. P., Oesch, P. A., Reddy, N., et al. 2016, arXiv:1611.07038

Nakamura, E., Inoue, A. K., Hayashino, T., et al. 2011, MNRAS, 412, 2579

Neugebauer, G., Habing, H. J., van Duinen, R., et al. 1984, ApJL, 278, L1

Oke, J. B., & Gunn, J. E., 1983, ApJ, 266, 713

Ono, Y., Ouchi, M., Mobasher, B., et al. 2012, ApJ, 744, 83

Oteo, I., Cepa, J., Bongiovanni, Á., et al. 2013, A&A, 554, L3

Ouchi, M., Shimasaku, K., Okamura, S., et al. 2004, ApJ, 611, 685

Ouchi, M., Hamana, T., Shimasaku, K., et al. 2005, ApJ, 635, 117

Overzier, R. A., Heckman, T. M., Wang, J., et al. 2011, ApJL, 726, L7

Peacock, J. A., & Smith, R. E., 2000, MNRAS, 318, 1144

Pettini, M., Kellogg, M., Steidel, C. C., et al. 1998, ApJ, 508, 539

Pettini, M., Steidel, C. C., Adelberger, K. L., Dickinson, M., & Giavalisco, M. 2000, ApJ, 528, 96

Pettini, M., Rix, S. A., Steidel, C. C., et al. 2002, ApJ, 569, 742

Pickles, A. J. 1998, PASP, 110, 863

Poglitsch, A., Waelkens, C., Geis, N., et al. 2010, A&A, 518, L2

Prévot, M. L., Lequeux, J., Maurice, E., Prévot, L. and Rocca-Volmerange, B., 1984, A&A, 132, 389

Reddy, N. A., Steidel, C. C., Fadda, D., et al. 2006, ApJ, 644, 792

Reddy, N. A., Erb, D. K., Pettini, M, Steidel, C. C., Shapley, A. E., 2010, ApJ, 712, 1070

Rieke, G. H., Young, E. T., Engelbracht, C. W., et al. 2004, ApJS, 154, 25

Roche, N., Eales, S. A., Hippelein, H., & Willott, C. J. 1999, MNRAS, 306, 538

Rogers, A, B., McLure, R. J., Dunlop, J. S., 2013, MNRAS, 429, 2456

Rogers, A. B., McLure, R. J., Dunlop, J. S., et al. 2014, MNRAS, 440, 3714

Sanders, D. B., Soifer, B. T., Elias, J. H., Neugebauer, G., & Matthews, K. 1988, ApJL, 328, L35

Schenker, M. A., Stark, D. P., Ellis, R. S., et al. 2012, ApJ, 744, 179

Seaton, M. J. 1979, MNRAS, 187, 73P

Siana, B., Smail, I., Swinbank, A. M., et al. 2009, ApJ, 698, 1273

Shimizu, I., Inoue, A. K., Okamoto, T., Yoshida, N. 2014, MNRAS, 440, 731

Simpson, J. M., Swinbank, A. M., Smail, I., et al. 2014, ApJ, 788, 125

Speagle, J. S., Steinhardt, C. L., Capak, P. L., Silverman, J. D., 2014, ApJ, 214, 15

Steidel, C. C., & Hamilton, D. 1992, AJ, 104, 941

Steidel, C. C., Pettini, M., & Hamilton, D. 1995, AJ, 110, 2519

Steidel, C. C., Giavalisco, M., Dickinson, M., & Adelberger, K. L. 1996, AJ, 112, 352

Steidel, C. C., Adelberger, K. L., Dickinson, M., et al. 1998, ApJ, 492, 428

Steidel, C. C., Adelberger, K. L., Shapley, A. E., et al. 2000, ApJ, 532, 170

Steinhardt, C. L.,Speagle, J. S., Capak, P. L., Silverman, J. D., 2014, ApJ, 791, 25

Swinbank, A. M., Simpson, J. M., Smail, I., et al. 2014, MNRAS, 438, 1267

Takeuchi, T. T., Yuan, F.-T., Ikeyama, A., Murata, K. L., & Inoue, A. K. 2012, ApJ, 755, 144

Tremonti, C. A., Heckman, T. M., Kauffmann, G., et al. 2004, ApJ, 613, 898

Tacconi, L. J., Genzel, R., Smail, I., et al. 2008, ApJ, 680, 246

Uchimoto, Y. K., Yamada, T., Kajisawa, M., et al. 2012, ApJ, 750, 116

Vanzella, E., Siana, B., Cristiani, S., & Nonino, M. 2010, MNRAS, 404, 1672

Veilleux, S., Kim, D.-C., Sanders, D. B., Mazzarella, J. M., & Soifer, B. T. 1995, ApJS, 98, 171

Veilleux, S., Kim, D.-C., & Sanders, D. B. 1999, ApJ, 522, 113

Yamada, T., Nakamura, Y., Matsuda, Y., et al. 2012a, AJ, 143, 79

Yamada, T., Matsuda, Y., Kousai, K., et al. 2012b, ApJ, 751, 29

Yoshida, M., Shimasaku, K., Kashikawa, N., et al. 2006, ApJ, 653, 988

Yuan, T.-T., Kewley, L. J., & Sanders, D. B. 2010, ApJ, 709, 884

Yun, M. S., Scott, K. S., Guo, Y., et al. 2012, MNRAS, 420, 957

Wardlow, J. L., Smail, I., Coppin, K. E. K., et al. 2011, MNRAS, 415, 1479

Webb, T. M. A., Yamada, T., Huang, J.-S., et al. 2009, ApJ, 692, 1561

Wilkins, S. M., Bunker, A. J., Stanway, E., Lorenzoni, S. & Caruana, J., 2011, MNRAS, 417, 717

Zackrisson, E., Inoue, A. K., & Jensen, H. 2013, ApJ, 777, 39

Zackrisson, E., Binggeli, C., Finlator, K., et al. 2016, arXiv:1608.08217

Zahn, O., Reichardt, C. L., Shaw, L., et al. 2012, ApJ, 756, 65

Zehavi, I., Weinberg, D. H., Zheng, Z., et al. 2004, ApJ, 608, 16

Zehavi, I., Zheng, Z., Weinberg, D. H., et al. 2011, ApJ, 736, 59